Realistic calculations for correlated materials

Von der Fakultät für Mathematik und Physik der Universität Stuttgart zur Erlangung der Würde eines Doktors der Naturwissenschaften (Dr. rer. nat.) genehmigte Abhandlung

Vorgelegt von

Daniil Toloui-Mantadakis

aus Athen, Griechenland

Hauptberichter:	Dr. Philipp Hansmann
Mitberichter:	Prof. Dr. Maria Daghofer
Prüfungsvorsitzender:	Prof. Dr. Hidenori Takagi
Tag der mündlichen Prüfung:	05. Februar 2020

Max-Planck-Institut für Festkörperforschung

Universität Stuttgart

2019

Contents

Preface **v**

Abstract **vii**

Zusammenfassung **ix**

Introduction **1**

1 General Background **5**

1.1 State of the problem: The Schrödinger equation 5

1.2 Density Functional Theory: an ab initio description 7

1.3 Low energy effective Hamiltonians 8

1.3.1 The Hubbard Model: a simple yet challenging prototype 9

1.3.2 Periodic Anderson Model 11

1.3.3 Multiorbital generalizations: A survival kit 11

1.4 Dynamical Mean-Field Theory 16

1.4.1 Key concepts and formulation 16

1.4.2 Limitations and extensions 21

1.5 Bringing two worlds together: The merger of DFT and DMFT 24

1.5.1 Constructing the *ab initio* Hamiltonian 24

1.5.2 Double counting and self-consistent cycle 26

1.6 Observables and connection to experiments 28
1.6.1 The problem of analytical continuation 28

2 Perturbative approaches around reference points **31**
2.1 The multi-orbital Random Phase Approximation 31
2.1.1 Linear response theory 32
2.1.2 Mathematical formulation 34
2.2 Strong coupling approximation impurity solver 41
2.2.1 Mathematical formulation 41
2.2.2 Implementation details 44
2.2.3 Benchmarks: The single-band Hubbard model 46
2.2.4 Final remarks 49

3 Investigation of the $LaNiO_2/LaGaO_3$ heterostructure **51**
3.1 Model and methodology 52
3.2 Results: Aggregated local spectral functions 54
3.3 Results: Layer and orbital resolved spectra 56
3.4 Summary 59

4 Interplay of CF and SOC **65**
4.1 Current driven insulator-to-metal transition 66
4.1.1 Models and technical details 68
4.1.2 Results and discussion 70
4.1.3 Conclusions 73
4.2 Generic study of t_{2g} system 75
4.2.1 Models and methods 76
4.2.2 Results: Comparison in the one-particle level 82
4.2.3 Results: Uniform and static response functions 83

4.2.4 Summary and conclusions 86

5 Dynamics of the PAM's magnetic response **89**

5.1 Models and methodology 90

5.2 Results: Single particle spectral functions 91

5.3 Results: Magnetic response functions 93

5.3.1 Static magnetic response 93

5.3.2 Dynamic magnetic response: Frequency- and time-domain 95

6 Summary **99**

Bibliography **101**

List of Figures **117**

List of Tables **125**

Acknowledgments **127**

Preface

This dissertation contains the results of my research carried out at the Max Planck Institute for Solid State Research between June 2015 and December 2019 in the group of and under supervision of Dr. Philipp Hansmann.

This dissertation is a result of my own work and includes nothing which is the outcome of work done in collaboration except where specifically indicated in the text. This dissertation has not been submitted in whole or in part for any other degree or diploma at this or any other university.

Stuttgart, _____ _____

Date Daniil Toloui-Mantadakis

Abstract

Strongly correlated fermionic systems nowadays stand in the forefront of condensed matter physics. A plethora of phenomena, ranging from unconventional superconductivity, gigantic and colossal magneto-resistance and metal-to-insulator transitions, are attributed to the effects of electron correlation. Given the spectacular progress on the experimental side, today – more than ever – the understanding of the underlying microscopic mechanisms, and the explanation or even prediction of experimental observations becomes a necessity. The advancements of theoretical and computational methodologies together with a concurrent increase of computational power, allows for both the *ab initio* study of realistic materials and the investigation of low-energy effective Hamiltonians inspired and designed to resemble whole classes of compounds.

This work is conceptually divided into two major parts. In Chapter 3 and Chapter 4, we present our results, obtained by the state-of-the-art merger of density functional and dynamical mean-field theory, for two realistic systems: the layered $LaNiO_2/LaGaO_3$ superstructure, where we focus on the orbital resolved single-particle spectral functions and study the effect of electron and hole doping; and the ruthenate system Ca_2RuO_4, for which we provide a clear understanding and theoretical support of the experimentally observed semi-metallic state under the application of DC current. The second conceptual part of this work deals with the study of low-energy effective Hamiltonians. In Chapter 4, we investigate a generic t_{2g} model Hamiltonian in the presence of non-spherical crystal-field potentials and/or spin-orbit coupling in order to shed more light on the distinct features that arise on the single-particle level and, most importantly, on the two-particle observables, such as the uniform and static magnetic susceptibilities. In Chapter 5, we investigate the multi-

orbital extension of the periodic Anderson model, as inspired by the family of cerium-based heavy-fermion compounds, with a clear focus on the evolution of the dynamic behavior of the systems' moments.

Zusammenfassung

Stark korrelierte fermionische Systeme stehen heutzutage an der Spitze der Physik der kondensierten Materie. Ein Überfluss von Phänomenen, die von unkonventioneller Supraleitung über gigantischen und kolossalen Magnetowiderstand bis hin zu Metall-Isolator Übergängen reichen, werden auf die Auswirkungen der Elektronenkorrelation zurückgeführt. Angesichts der spektakulären Fortschritte auf der experimentellen Seite, werden heute - mehr denn je - das Verständnis der zugrunde liegenden mikroskopischen Mechanismen und die Erklärung oder sogar Vorhersage experimenteller Beobachtungen zu einer Notwendigkeit. Die Weiterentwicklung theoretischer und computer-basierter Methoden mit gleichzeitiger Steigerung der rechnerischen Leistung ermöglicht sowohl die *ab initio* Untersuchung realistischer Materialien als auch die Untersuchung von niederenergetischen effektiven Hamiltonians, die inspiriert und so entworfen wurden, dass sie ganzen Verbindungsklassen ähneln.

Diese Arbeit ist konzeptionell in zwei Hauptteile gegliedert. In den Kapiteln 3 und 4 stellen wir unsere Ergebnisse vor, die durch die State of the Art Zusammenführung von Dichtefunktional- und dynamischer Mittelfeldtheorie für zwei realistische Systeme erhalten wurden: die geschichtete $LaNiO_2/LaGaO_3$ - Überstruktur, bei der wir uns auf die orbital aufgelösten Einteilchen-Spektralfunktionen konzentrieren und den Effekt von Elektronen- und Lochdotierung untersuchen; und das Ruthenatsystem Ca_2RuO_4, für das wir ein klares Verständnis und eine theoretische Unterstützung des experimentell beobachteten halbmetallischen Zustands unter der Anwendung von Gleichstrom liefern. Der zweite konzeptionelle Teil dieser Arbeit befasst sich mit der Untersuchung von niederenergetischen effektiven Hamilton-Operatoren. In Kapitel 4 untersuchen wir einen generischen t_{2g} Modell-Hamiltonian in Gegenwart von nicht-sphärischen Kristallfeldpotentialen und/oder Spin-

Orbit-Kopplung, um ein klareres Verständnis der Besonderheiten, die auf der Einteilchen Ebene enstehen, aber vor allem auf Zweiteilchen-Observablen, wie die gleichmäßigen und statischen magnetischen Suszeptibilitäten. In Kapitel 5 untersuchen wir die Multi-Orbital-Erweiterung des periodischen Anderson-Modells, inspiriert von der Familie der Schwerfermionverbindungen auf Cerium-Basis, mit einem klarem Fokus auf die Evolution des dynamisches Verhaltens der System-Momente. In Kapitel 6 fassen wir die wichtigsten Punkte dieser Arbeit zusammen.

Introduction

The Stone Age, the Copper Age, the Iron Age... Materials have always been so important that eras of human history – characterized usually by abrupt socio-economical global change– have been named based on the very ability of controlling and, more crucially, exploiting their properties. However, this day and age – the Silicon or Information Age – is unique in a special regard: the technological and scientific progress – especially since the advent of quantum mechanics – enables us now to understand, predict and even manipulate matter on the microscopic level. This has led to rapid and fascinating advancements – unimaginable decades ago – that allow to design functional materials tailored for specific purposes, that are progressively manifested in every aspect of modern technology and contemporary life.

Quantum mechanics played a pivotal role in this "revolution", providing the "equation of everything"[1], the Schrödinger equation. However, although is in our hands for almost a century now, its direct solution is a futile task, due to the immense amount of degrees of freedom. This has been already foreseen and quoted in the early days of quantum mechanics by Paul Dirac:

> [...] The underlying physical laws necessary for the mathematical theory of a large part of physics and the whole of chemistry are thus completely known, and the difficulty is only that the exact application of these laws leads to equations much too complicated to be soluble. It therefore becomes desirable that

[1] Regarding the nucleous and electrons.

> approximate practical methods of applying quantum mechanics should be developed. [...]

This summarizes the scope of a large branch of condensed matter physics, which focuses on the development and application of approximation schemes to draw insights on the properties of matter. In this regard, the classification of systems with respect to the strength of correlations has been of paramount importance. In weakly correlated systems, an effective single-particle description – as provided by e.g. density functional theory – holds, and the one many-body problem reduces to the solution of many tractable one-body problems. In the second category, such an effective description breaks down as correlation effects grow stronger, and many-body approaches have to be considered at least in a subset of the present degrees of freedom. To reduce the intractable number of degrees of freedom, while still capturing the most relevant energy-scales and mechanisms of a system, effective low energy Hamiltonians have been proposed. Additionally, a plethora of many-body approaches have been devised or tailored in order to provide approximate solutions for them. [2].

Dynamical mean-field theory is one of the most successful non-perturbative approaches to capture and account for correlation effects, by mapping the original effective lattice model onto an effective impurity problem self-consistently. Furthermore, algorithmic advances nowadays allow for the study of even extended (multi-orbital) systems manageable numerical cost. And its recent merger with density functional theory is considered to be the state-of-the-art framework for *ab initio* electronic structure calculations, where effective Hamiltonians encoding material features (explicitly) and correlation effects (approximately) are considered all together.

[2] It is important to note that even the simplest effective model, the Hubbard model, cannot be solved exactly except for special cases.

Overview and Scope of the Thesis

In this thesis we perform both material specific ab initio calculations within the framework of (DFT+)DMFT and study models that stand as adequate representatives for whole classes of materials. In the former case, we particularly focus on the study of single particle observables, such as single-particle spectral functions, aiming to support, explain and predict experimental studies. In the latter case, motivated by transition metal systems that belong either to the early 3d, 4d and 5d series and rare earth, heavy-fermion, compounds, we construct and study effective multi-orbital Hamiltonians, considering the most relevant energy scales and their interplay, to shed more light, on both the static and dynamic two-particle response.

The main structure of the thesis is organized as follows:

- Chapter 1 is devoted to a short presentation of the most important theoretical parts that are necessary to follow the subsequent sections of the work. Starting from the effective Hamiltonians that have been employed throughout the thesis, we focus on their multi-orbital extensions that are the basis to describe real systems. Dynamical mean-field theory and its merger with density functional theory are presented in detail, together with comments on the actual objectives and limitations of the methods.

- In Chapter 2, perturbative approaches around the exactly solvable reference points – the non-interacting and the atomic-limit – are discussed. In the first part I present the multi-orbital extension of the Random Phase Approximation, which offers an efficient way to extract information on the two-particle level, while targeting the response functions (dynamic and static) of the system. In the second part I discuss the mathematical and most importantly the computational realisation of the strong coupling approximation impurity solver. It belongs to a wide family of so-called semi-analytical solvers and can be efficiently employed within the DMFT framework.

- In Chapter 3 we present our *ab initio* DFT+DMFT results on the $LaNiO_2/LaGaO_3$ superstructure in detail. Here we focus on the layer and orbital resolved single-particle spectral functions of the system and study the effect of electron and hole

doping on the overall orbital distribution.

- Chapter 4 consists of two parts. First, we present our realistic calculations for the Ca_2RuO_4 compound that provide a clear theoretical understanding and support to the experimentally observed semi-metallic state under the application of DC current. The second part is devoted to pure model calculations, where we focus on the distinct effects induced by (tetragonal) crystal field potentials and/or spin orbit coupling splittings. In particular we investigate both the single particle local spectral functions, but most importantly the uniform and static magnetic susceptibilities. Although the latter is more challenging to obtain, it is more sensitive to distinguish the conserved quantities of the employed models.

- In Chapter 5 we study a multi-orbital extension of the periodic Anderson model, resembling heavy-fermion systems, and focus primarily on the dynamics of the localized moments immersed in the fermionic conduction sea. In fact we show that the hybridization between the localized states and the conduction bands define the time-scale decay of fluctuations and thus restrict the applicability of purely local models.

- In Chapter 6 we provide a short summary of the key points of this work.

Chapter 1

General Background

In this chapter, I will discuss the general concepts that my thesis is based on. Whenever possible, I provide intuitive pictures instead of formal derivations that can be found in a plethora of well-known textbooks. The aim is to present the basic notions, approximations and methodologies that form the field of realistic calculations for correlated materials in such a way that the rest chapters can be followed consistently.

1.1 State of the problem: The Schrödinger equation

The electronic properties of a time-independent condensed matter system are governed by the Schrödinger equation, $\hat{H}\psi = E\psi$, where ψ is the many-body (electron) wavefunction, E is the energy of the system and $\hat{H}$ is its Hamiltonian. In the non-relativistic limit, the latter reads:

$$\hat{H} = \hat{H}^{(e)}_{\text{kin}} + \hat{H}^{(n)}_{\text{kin}} + \hat{H}^{(e-n)}_{\text{int}} + \hat{H}^{(n-n)}_{\text{int}} + \hat{H}^{(e-e)}_{\text{int}}, \tag{1.1}$$

where the superscript e (n) refers to the electron (nuclei). Albeit complete, Eq. (1.1) is usually simplified by employing the so-called Born-Oppenheimer approximation [24], within which the electrons' and nuclei' degrees of freedom decouple. The nuclei are orders of magnitude more massive than electrons, therefor they can be considered as (purely) sta-

tionary for all (relevant) timescales of the latter. Hence, the second and fourth term in Eq. (1.1) can be neglected [1], and the electronic many-body Hamiltonian reads as,

$$\hat{H} = -\frac{\hbar^2}{2m}\sum_{i=0}^{i=N}\nabla_i^2 - \sum_{i,I}\frac{Z_I e^2}{|\boldsymbol{r}_i - \boldsymbol{R}_I|} + \frac{1}{2}\sum_{i\neq i'}\frac{e^2}{|\boldsymbol{r}_i - \boldsymbol{r}_{i'}|}, \tag{1.2}$$

where $\boldsymbol{r}_i$ ($\boldsymbol{R}_I$) is the position of the i-th electron (I-th) nucleus) of the system, m is the electron-mass and Z_I is the atomic-number. The first term accounts for the kinetic energy of the electrons while the second – given that the set of nuclei positions forms a rigid crystal-structure – corresponds to a single-particle potential. It is the last term, the Coulomb repulsion between electrons, that aggravates the complexity of the problem, since it couples all remaining degrees of freedom and as a consequence all electrons become correlated.

An immediate consequence is that the solution of the corresponding eigenvalue equation is out-of-reach already when few particle are involved, a fact that has been already foreseen in the early days of quantum mechanics. Still, approximations and effective theories emerged, which filled the gap between theory and realization leading to a deep understanding of the underlying physics of matter. For example, band theory and, soon after, the celebrated Landau Fermi liquid theory [79] revealed that for a wide range of materials, the original interacting and correlated problem is adiabatically connected to a system of non-interacting *quasiparticles* with effective or renormalized parameters, which can be solved with rather minimal efford. Such systems are typically labeled as weakly correlated and correspond to compounds with typically wide valence bands.

On the other hand, in compounds with narrow bands, that typically originate from open d or f valence shells, such one-particle description breaks-down. A prototypical example of such systems, labeled as strongly correlated, is the transition metal oxide NiO: band theory predicts it to be a metal, while in reality it is an insulator. The seeds to the explanation of such a remarkable failure were placed by Mott, who pointed out the electronic interactions to be the reasoning.

Further discoveries of other strongly correlated materials together with the realization of their extreme sensitivity upon adjustable external parameters and the diversity of phases

[1] More precisely, the nucleus-nucleus interaction energy adds a constant shift in the total-energy.

that can be triggered, eventually branched the community of condensed matter into two main categories with respect to the characterization of electronic correlations, typically with different questions to answer and methodological tools to employ and develop: in the first case effective one-particle approximations to solve the original many-body problem are employed, while, in the second, many-body approaches and effective low-energy Hamiltonians are used to reduced the complexity and seek insights.

1.2 Density Functional Theory: an ab initio description

The evolution of density functional theory, in its modern form, has been marked by two major steps [69][62]. First, it was Hohenberg and Kohn that rigorously proved that the particle-density uniquely determines the Hamiltonian, and thus the total energy, of a given system [59]; this would later remain in history as the HK theorem. Build on top, the second step, was given by Kohn and Sham who provided the corresponding practical scheme [70]: a mapping of the original interacting system onto an auxiliary non-interacting one, under the condition that both systems have the same ground-state density, transforms the one many-body problem into many one-body problems. The resulting exact equations are known as the Kohn-Sham equations [2] and read as,

$$\left(\frac{\hbar^2}{2m}\nabla_i^2 + V_{\text{ion}}(\boldsymbol{r}) + \int d^3\boldsymbol{r}' V_{ee}(\boldsymbol{r}-\boldsymbol{r}')n(\boldsymbol{r}') + \frac{\delta E_{xc}[n]}{\delta n(\boldsymbol{r})}\right)y_i(\boldsymbol{r}) = \epsilon_i y_i(\boldsymbol{r}), \tag{1.3}$$

where $n(\boldsymbol{r})$ is the particle-density and $V_{\text{ion}}(\boldsymbol{r})$ is the ionic potential; the first term is the kinetic energy while the third term is the Hartree term; y_i and ϵ_i are formally Lagrange multipliers introduced for the mapping [3]. Their solution can be achieved by self-consistent schemes, given the form of the – generally unknown – exchange-correlation functional $E_{xc}[n]$. The later is practically the *only* approximation that needs to be employed before utilizing the self-consistent cycle for a target particle-density. (sketch)

[2] For a derivation of the Kohn-Sham equations we refer to AppendixXXX.

[3] Note however, that due to the surprising good estimates when those Lagrange multipliers are interpreted as *real* wavefunctions and excitation energies, the objectives of DFT go nowadays beyond the calculation of the ground state energy and density, e.g. calculation of density of states, bandstructures, responses, e.t.c.

The construction, development and extension of such exchange-correlation functionals ,to take into account a larger portion of the electronic correlations, is still an active field of research [134]. Among the most famous approximations for the exchange-correlation potential, widely used in the solid-state community, one finds the (spin-resolved) local density approximation, (s)LDA, and it's gradient extension (s)GGA [15].

Being computationally inexpensive and versatile, DFT has gained extreme popularity that exceeds the boundaries of solid-state physics, and one finds applications in as diverse fields as astrophysics [7] and drug design [58]. In the fields of material science and chemistry, it has been the standard tool to explore material trends, while nowadays large (commercial or open-source) code bases allow access to a plethora of interesting properties. Gradually, DFT became the synonym of first-principles or ab initio method.

Nevertheless, and despite the advancements, DFT still remains practically a one-particle theory that treats the complicated correlations in a static mean-field manner. Thus, it is confined to give acceptable results for only the weakly correlated class of compounds, or at most to mimic the effects of strong-correlations through the ad-hoc inclusion of effective energy splittings [9][85]. For a proper treatment of strong-correlations one needs to reside to many-body approaches, which is the subject of the next sections.

1.3 Low energy effective Hamiltonians

The second branch of the community – the many-body one – aims to attack Eq. (1.2) from another perspective. Instead of seeking approximate single-particle solutions of the original problem, it tries to construct reduced – in terms of degrees of freedom – effective model Hamiltonians and deal with their full complexity. Here, *reduced* shall be understood as *minimal*, in terms of answering the question "Which degrees of freedom cannot be neglected?". At the same time, *effective* has the meaning of *renormalized*: truncation of the phase-space of the problem in a controlled procedure, corresponds to a redefinition of the constitutional parameters that act on the selected target energy window.

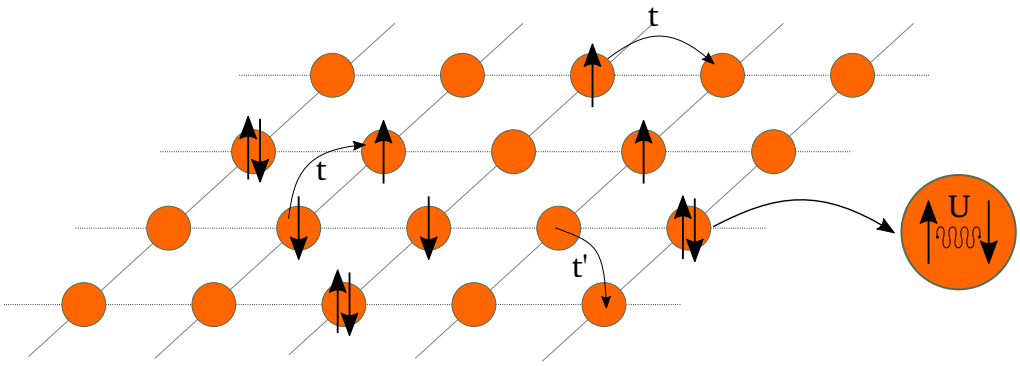

Fig. 1.1: The Hubbard model of a two-dimensional square lattice with first and second nearest neighbors hopping, t and t', and a local Coulomb interaction, U.

That said, it is advisable to change the notation of Eq. (1.2) into second quantization form. In a localized Wannier basis [139][95], Eq. (1.2) is written as,

$$\hat{H} = \sum_{ij}\sum_{\alpha\beta} t_{ij}^{\alpha\beta}\hat{c}_{i\alpha}^{\dagger}\hat{c}_{j\beta} + \frac{1}{2}\sum_{ii'jj'}\sum_{\alpha\alpha'\beta\beta'} U_{ii'jj'}^{\alpha\alpha'\beta\beta'}\hat{c}_{i\alpha}^{\dagger}\hat{c}_{i'\alpha'}^{\dagger}\hat{c}_{j'b'}\hat{c}_{jb}, \tag{1.4}$$

where $\hat{c}_{i\alpha}^{\dagger}$ ($\hat{c}_{i\alpha}$) are the usual fermionic creation (annihilation) operators that create (destroy) a particle on a Wannier orbital centered at site i with orbital and spin quantum numbers $\alpha = \{\tau_a, \sigma\}$. Note that until this point, no approximation on the electronic Hamiltonian has been employed: Eq. (1.4) is nothing but the so-called tight-binding representation of Eq. (1.2).

In the following sections, I will discuss the simplifications, approximations and rationale behind two derived models that are considered in this work.

1.3.1 The Hubbard Model: a simple yet challenging prototype

For a time-spread of more than 50 years, the (fermionic) Hubbard model has been the subject of extensive studies both numerical and analytical. Nowadays, it serves as the prototypical Hamiltonian for the description of correlated fermionic systems, and it is conjectured to describe the physics high-temperature superconductivity [142, 6].

The model was introduced – at the same year but independently – by J. Hubbard [60], J.

Kanamori [65] and M.C. Gutzwiller [49], for the description of transition metals, itinerant magnetism and the metal-to-insulator transition, respectively [4]. For a given lattice $\mathscr{L}$, the Hamiltonian formally reads:

$$\hat{H} = \hat{H}_{\text{kin}} + \hat{H}_{\text{int}} = \sum_{i,j\in\mathscr{L}} \sum_{\sigma} t_{ij}^{\sigma} \hat{c}_{i\sigma}^{\dagger} \hat{c}_{j\sigma} + \sum_{i\in\mathscr{L}} U_i \hat{n}_{i\uparrow} \hat{n}_{i\downarrow}. \tag{1.5}$$

The first term, stands for the hopping processes – via tunneling effect – of electrons from site i to site j, and describes their itinerant character. The second term, in contrast, favors localization by penalizing any potential double-occupancy on any site. And it is the interplay of those energy scales, together with the particle-density and the lattice structure that determine the ground-state properties and excitation spectrum of the system. In the non-interacting, $U = 0$, and in the atomic, $t = 0$, limit, Eq. (1.5) can be readily diagonalized in momentum or real space, respectively. Analytic solutions are only known for one dimension via the Bethe Ansatz [92][20] and in the limit of infinite dimensions through dynamical mean-field theory.

The apparent simplicity of the Hubbard model is only deceptive in case of other dimensions, except the two mentioned extremes. As four possible states, namely $|0\rangle, |\uparrow\rangle, |\downarrow\rangle, |\uparrow\downarrow\rangle$, can be realized on each lattice site, the configuration space of the whole system grows as 4^N, where N is the number of lattice sites. Thus, exact diagonalization of the Hamiltonian – with or without employing symmetries – is only possible for limited number of sites, and finite-size effects prohibit a controlled extrapolation to the thermodynamic limit.

An accurate numerical treatment, able to handle the exponential growth of the configuration space – for a general parametrization of the model – remains an open and challenging research topic. Lattice Quantum Monte Carlo variants[36] suffer from the so-called fermionic sign-problem [135] which becomes severe away from half-filling and for intermediate-to-strong coupling strength; density matrix-renormalization group (DMRG) approaches [126, 115], while essentially exact in 1D, face extreme difficulties in two-dimensions and above, since the bond dimension increases exponentially with the width of the quasi-1-dimensional stripe.

[4] In chemistry, it is known as the Pariser-Parr-Pople model, introduced already ten years prior.

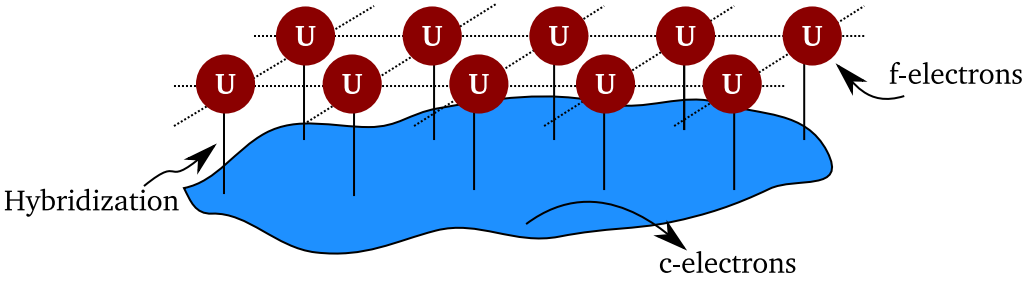

Fig. 1.2: A picturial view of the periodic Anderson model (PAM).

1.3.2 Periodic Anderson Model

The description of partially filled f-electron systems – rare earth lanthanides and actinides – is typically sought for by another low-energy effective Hamiltonian: the periodic Anderson Model (PAM) [104]. The PAM Hamiltonian, describes periodically aligned f-shells embedded in a metallic (itinerant) host, and reads:

$$\hat{H}_{\text{PAM}} = \sum_{\boldsymbol{k},\sigma} \varepsilon_{\boldsymbol{k}} \hat{c}^{\dagger}_{\boldsymbol{k}\sigma} \hat{c}_{\boldsymbol{k}\sigma} + \varepsilon_f \sum_{i\sigma} f^{\dagger}_{i\sigma} f_{i\sigma} + U \sum_{i} n_{fi\uparrow} n_{fi\downarrow} \sum_{i,\boldsymbol{k},\sigma} (V_{i\boldsymbol{k}}\, f^{\dagger}_{i\sigma} \hat{c}_{\boldsymbol{k}\sigma} + h.c). \tag{1.6}$$

Here, $f^{\dagger}_{\sigma}, f_{\sigma}$ are creation and annihilation operators of f-electrons with spin σ, while $c^{\dagger}_{\boldsymbol{k}\sigma}, c_{\boldsymbol{k}\sigma}$ are creation and annihilation operators of conduction electrons with dispersion relation $\varepsilon_{\boldsymbol{k}}$. The last term describes the hybridization between localized f-states, subject to the interaction U, and the fermionic conduction sea.

Note that no direct hopping between f-electrons exists: f electrons can acquire kinetic energy only via their hybridization with the conduction electrons in case that charge fluctuations – controlled by the strength of the on-site repulsion – are energetically favorable. For various extensions as well as (semi-)analytical and numerical treatments of the PAM, we refer the interested reader to Ref. [57].

1.3.3 Multiorbital generalizations: A survival kit

Our first assumption when describing the Hubbard model was that the underlying low-energy physics can be described by a single-band placed around the Fermi energy. How-

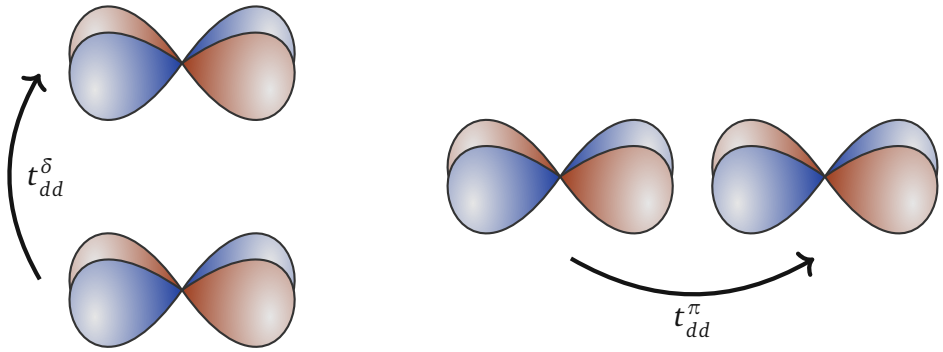

Fig. 1.3: Examples of parametrization of the hopping between d-orbitals. The π (σ) bond corresponds to the case where the density distribution lobes point towards (parallel to) each other.

ever, in most *realistic* cases such a *downfolding* is not possible. Multiple bands lie on or in the proximity of the Fermi energy while they might hybridize strongly with other itinerant valence states. The aim of this section is to describe the main components and additional terms that typically arise and provide the key ideas of predicting the behavior of such systems, which we formally express through the multi-orbital generalization of the Hubbard Hamiltonian:

$$\hat{H} = \sum_{i\neq j}\sum_{\alpha\beta\sigma} t_{ij}^{\alpha\beta\sigma}\hat{c}^{\dagger}_{i\alpha\sigma}\hat{c}_{j\beta\sigma} + \sum_{i}\sum_{\alpha\beta}\sum_{\sigma\sigma'} h_{\alpha\beta}^{\sigma\sigma'}\hat{c}^{\dagger}_{i\alpha\sigma}\hat{c}_{i\beta\sigma'} + \sum_{i}\sum_{\alpha\beta\gamma\delta}\sum_{\sigma\sigma'} U_{\alpha\beta\gamma\delta}^{\sigma\sigma'}\hat{c}^{\dagger}_{i\alpha\sigma}\hat{c}^{\dagger}_{i\beta\sigma'}\hat{c}_{i\gamma\sigma'}\hat{c}_{i\delta\sigma}, \tag{1.7}$$

where we have chosen to split the quadratic part into a local, $h_{\alpha\beta}^{\sigma\sigma'}$, and non-local part, $t_{\alpha\beta}^{\sigma\sigma'}$, while once again we consider only local interactions[5]. For the following, we further assume a system, where a d-shell atom resides on each lattice site, as is the case for transition metals of the $3d$, $4d$ and $5d$ series of the periodic table, although the same argumentation follows naturally for any shell type, i.e f-shells of the lanthanides series. The hopping integrals, e.g. shown Fig. 1.3, $t_{ij}^{\alpha\beta\sigma}$ can be obtained by considering the interatomic Slater-Koster

[5]Extending the model to include non-local interactions is straightforward, but will not be considered in any part of this work.

two-center integrals [53, 131], and they will not be discussed further.

The isolated atom: Let us start by considering only the presence of the last term of Eq. (1.7), namely an isolated d-shell. For $N \geq 2$ full diagonalization of the rotationally invariant $SO(3)$ interaction operator – parametrized in our case with 3 independent coefficients – written in the d^N Hilbert space, yields the so-called multiplet structure of the atom [127]. Its ground state, $|GS\rangle$, is determined by the infamous Hund's rules: **(i)** the $|GS\rangle$ has the maximum possible total-spin $\boldsymbol{S}$, **(ii)** the $|GS\rangle$ has the maximum possible total orbital angular-momentum $\boldsymbol{L}$ and **(iii)** for more (less) than half-filled shell the $|GS\rangle$ has the maximum (minimum) total angular momentum, $\boldsymbol{J}$, possible [6].

Atomic-shells embedded into a lattice: We now turn our focus to the energy scales that emerge or are typically introduced, when considering a periodic lattice. When an atom is embedded in a solid, its original $SO(3)$ symmetry reduces to the symmetry group of the corresponding lattice. More specifically, as shown in Fig 1.4, let us assume the very common in transition-metal oxides perovskite structure: here the d-shell is placed in the center of a perfect octahedron with oxygens (ligands) at its corners. This symmetry corresponds to the O_h point group.

In first approximation, we can assume the oxygens as being point charges (no orbital structure). The symmetry operations, that leave the Hamiltonian invariant, determine the form of the single-particle states. The original (atomic) 5-fold degeneracy is lifted and two degenerate subspace arise: a 3-fold and a 2-fold irreducible representation, labeled as t_{2g} and e_g respectively, with an energy difference denoted as Δ_{CF}. To get an intuitive picture of the crystal field effects, we will use another notation for our five single-particle wavefunctions – the tesseral harmonics T_l^m–, constructed as linear combinations of the complex-valued spherical harmonics: $d_{xy}, d_{yz}, d_{zx}, d_{x^2-y^2}, d_{z^2}$. The tesseral harmonics are real-valued functions and their electron distribution is shown in Fig. 1.4.

Given the octahedral point-charge structure around the d-shell, we can readily see that the

[6] The last rule applies when considering spin-orbit coupling interaction.

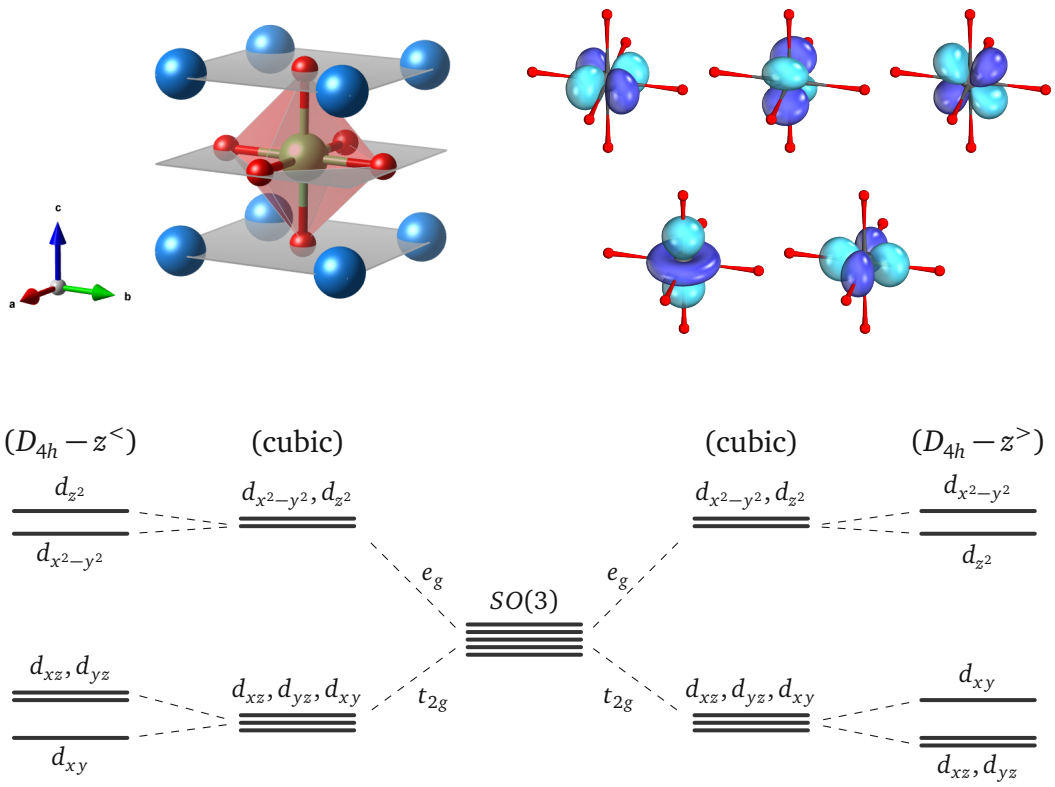

Fig. 1.4: (top-left) The unit cell of a cubic perovskite ABO_3. (top-right) The d orbitals in the basis of tesseral harmonics. (bottom) Energy level splittings of the d-shell due to the experience of an (I) octahedral, O_h, and (II) tetragonal , D_{4h}, crystal-field generated from the surrounding ligands. The far-left case corresponds to a compression of the z-axis while the far-right case corresponds to an elongation of the z-axis.

lobes of the electron distribution for $d_{x^2-y^2}$ and d_{z^2} (the e_g subsapce) point directly towards the corners of the octahedron. Thus, they will experience stronger Coulomb repulsion and will be shifted upwards in energy with respect to the d_{xy}, d_{yz} and d_{zx} orbitals (the t_{2g} subspace) which point in between the surrounding ligands. The same argumentation follows also for the splittings – and the orbital characters – resulting from a compression or an elongation along the c-axis of the octahedron: a tetragonal crystal-field described by the D_{4h} point-group symmetry.

It should be noted once again that the above ionic view, the crystal-field theory, is an approximation, since it principally neglects the effect of covalency: equivalently this means

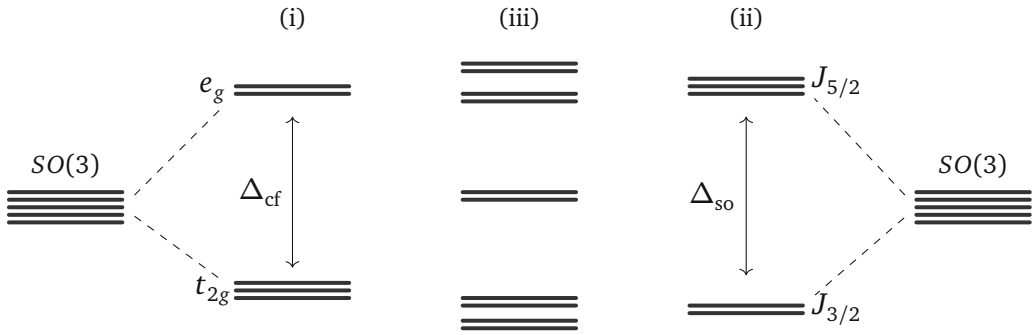

Fig. 1.5: Energy splittings of the d-shell. **(i)** Splittings based on a cubic crystal-field, which is diagonal in basis of the tesseral harmonics, T_l^m. **(ii)** Splittings generated from the spin-orbit coupling, which is diagonal in the basis of total-angular momentum, $|J;J_z\rangle$. **(iii)** Splittings generated when both cubic crystal-field and spin-orbit coupling operator act on the d-state manifold. Note that no good single particle basis exists [123].

that the oxygen states lie far below our low energy window so that they do not hybridize with the d-shell. When the latter assumption does not hold, a more comprehensive treatment must be considered, known as *ligand-field theory*, where both the electrostatic and the covalent bonding (hybridization) between ligands and the transition metal are explicitly taken into account [7].

Another quadratic term, that is considered in this work, is the relativistic spin-orbit coupling operator, whose action results in splittings of the multiplets with total angular momentum **J**. Expressed in the basis of spherical harmonics, $|l,m,\sigma\rangle$, it is given by,

$$\hat{H}_{\mathrm{so}} = \lambda\Bigg(\sum_{m=-l}^{m=+l}\sum_{\sigma} m\sigma\hat{c}^{\dagger}_{m\sigma}\hat{c}_{m\sigma} + \sum_{m=-l}^{m=l-1} p_l^m(\hat{c}^{\dagger}_{m+1\downarrow}\hat{c}_{m\uparrow} + \hat{c}^{\dagger}_{m\uparrow}\hat{c}_{m+1\downarrow})\Bigg), \tag{1.8}$$

where $p_l^m = \frac{1}{2}\sqrt{l+m+1}\sqrt{l-m}$ and λ is the spin-orbit coupling strength. For transition metals that belong to the $3d$-series, the spin-orbit coupling is rather small – of the order of meV – when compared with the crystal-field splitting between the t_{2g} and e_g subspace – of the order of eV – and often is neglected. This is not the case for $4d$ and especially $5d$ series compounds, where the situation might even be the opposite, or in cases that the crystal-field symmetry is further reduced, e.g. by tetragonal distortions. There, one

[7] A systematic study of group, crystal and ligand field theory is far beyond the scope of this section. The interested reader is pointed the excellent monograph [14].

actually needs to compare the energy scales of *all* crystal-field splittings to decide if the spin-orbit coupling can be safely neglected.

A schematic view of the d-shell including both single-particle operators is shown in Fig. 1.5.

1.4 Dynamical Mean-Field Theory

In absence of exact analytical or numerical treatment of (even) the single-band Hubbard model, it has been a necessity to seek for another route towards the exploration of its phase diagram. Many-body approaches based on expansions around small parameters – when existing – proved to be extremely useful: the physical properties of the system can be accessed through one- or two-particle Green's functions which not only can be computed in a controlled manner but are also cheaper to store memory-wise and easier to analyze than the *bulky* many-body wavefunction.

Nevertheless, while one can envisage a perturbative expansion around the extreme coupling limits, no obvious small parameter for the intermediate regime seemed to exist. It has been the seminal work of W. Metzner and D Vollhardt, that revealed the existence of another limit: the infinite dimensions or infinite coordination number [97]. In this limit a non-perturbative expansion with respect to the coupling strength is possible and sets the foundation of the so-called dynamical mean-field theory [42, 55, 73, 37].

1.4.1 Key concepts and formulation

Following the ideas of Ref. [97], consider the single-band Hubbard model for the case of a d-dimensional hypercubic lattice and assume only nearest-neighbor hopping with strength t. In such case, the kinetic part of Eq. 1.5 can be readily diagonalized and the corresponding eigenvalues are,

$$\epsilon(\boldsymbol{k}) = -2t \sum_{a=1}^{d} \cos(k_a), \tag{1.9}$$

where k_a is the projection of the $\boldsymbol{k}$ vector on the a axis. Given the eigenvalues, one can evaluate the corresponding density of states (DOS), as:

$$D(\omega) = \Big(\frac{1}{2\pi}\Big)^{d/2} \sum_{\boldsymbol{k}} \delta(\omega - \epsilon(\boldsymbol{k})) \overset{d\to\infty}{=} \frac{1}{2t(\pi d)^{1/2}} e^{-\left(\frac{\omega}{2t\sqrt{d}}\right)^2}, \tag{1.10}$$

where for the last equality we used the central limit theory. The kinetic energy scales as the variance (the second moment) of the above distribution, and thus diverges in the limit $d \to \infty$, given a constant hopping amplitude, t. In contrast, the potential energy per lattice site of the system does not scale with the number of dimensions. Consequently, in this limit the model would lead to a trivial situation: the competition between kinetic and potential energy would not be captured. To capture the competition between the two relevant scales in this limit, we need to introduce a scaling factor. This is equivalent to *force* the above variance to be finite and can be achieved by a renormalization $t \approx t^*/\sqrt{2d}$. The scaling derived above for the specific assumptions can be generalized for a system with long range hopping elements by introducing the quantity $\mathscr{Z}_{||i-j||}$. The latter counts the number of equivalent sites at distance $||i-j||$ from site i. The scaling, then, reads as

$$t_{ij} \propto \frac{t^*_{ij}}{\mathscr{Z}_{||i-j||}}. \tag{1.11}$$

Diagrammatics in the limit of infinite dimensions: We proceed by asking "How does the single-particle propagator of the system behave in the limit $d \to \infty$, given the scaling of the hopping amplitudes as in Eq.(1.11)? ". For the non-interacting single-particle propagator, $G^0_{ij}(i\omega_n)$, written on the Matsubara axis, we can show – by expansion – that it scales exactly as the hopping amplitudes, namely:

$$G^0_{ij}(i\omega_n) = \Big[(i\omega_n + \mu)\mathbb{1} - \tilde{t}\Big]^{-1}\Big|_{ij} \propto \frac{1}{\mathscr{Z}_{||i-j||}}, \tag{1.12}$$

where μ is the chemical potential of the system that fixes the particle-density. The interacting Green's function, $G_{ij}(i\omega_n)$ is connected with the non-interacting one and the self-energy, $\Sigma_{ij}(i\omega_n)$, via the Dyson equation:

$$G_{ij}(i\omega_n) = \Big(\big[G^0_{ij}(i\omega_n)\big]^{-1} - \Sigma_{ij}(i\omega_n)\Big)^{-1}. \tag{1.13}$$

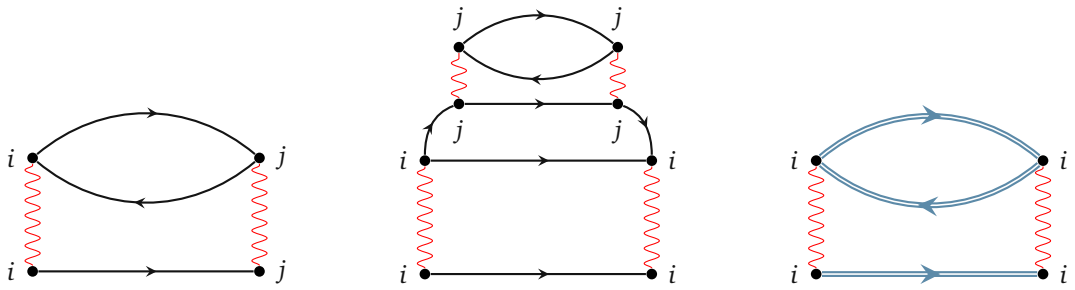

Fig. 1.6: Examples of Feynman diagrams for the self-energy. **(a)** second-order diagram of the self-energy, **(b)** non-skeleton self-energy diagram, **(c)** Second-order diagram of the self-energy expressed in terms of the interacting (dressed) single-particle propagator.

Thus, assuming that the self-energy tends to zero faster than the hopping amplitudes when $\mathscr{Z}_{||i-j||} \to \infty$ – a condition that we will verify shortly – the interacting Green's function has the same scaling as the non-interacting one.

In Fig. (1.6a), we show a second-order Feynman diagram that contributes to the self-energy of our system, Σ_{ij}. Given that our interaction is considered to be local and thus it connects a site i with itself, we can distinguish between two cases:

- Non-local contributions, namely when $i \neq j$: Since we have three non-local propagators involved, all these diagrams scale as $\mathscr{Z}_{||i-j||}^{-3/2}$ and thus vanish in the limit of $\mathscr{Z}_{||i-j||} \to \infty$.
- Local contribution, namely when $i = j$: In this case the diagram remains finite even in the limit of infinite coordination number.

The same argument holds for all non-local contributions to the self-energy, as long as two different sites are connected by at least three lines (propagators). In Fig. (1.6b), we show another diagrammatic possibility for the self-energy, where now two different lattice sites are connected by only two lines (propagators). In that case, the two propagators provide a factor of $\mathscr{Z}_{||i-j||}^{-1}$ which cancels exactly with the prefactor of the implied internal summation (over j). However, the figure is already included when we consider *local* interacting

propagators (blue lines) to build-up our diagrammatics, as shown in Fig. (1.6c).

Thus, we can conclude that in the limit of infinite dimensions only the local diagrams contribute to the self-energy: the non-local ones are irrelevant since they scale at least as $\mathscr{Z}^{-3/2}_{||i-j||}$. Transforming the notation from the real to the reciprocal space, this corresponds to:

$$\Sigma_{ij}(z) = \delta_{ij}\,\Sigma(\omega) \quad \rightarrow \quad \Sigma(z,\boldsymbol{k}) = \Sigma(\omega). \tag{1.14}$$

So far, we have shown that, in limit of infinite dimensions, the correlations encoded in the self-energy, collapse onto the local ones only. That is, for the interacting lattice Green's function of the Hubbard model:

$$G(\boldsymbol{k}, i\omega_n) = \Big(i\omega_n + \mu - \epsilon(\boldsymbol{k}) - \Sigma(\boldsymbol{k}, i\omega_n)\Big)^{-1} = \Big(i\omega_n + \mu - \epsilon(\boldsymbol{k}) - \Sigma(i\omega_n)\Big)^{-1}. \tag{1.15}$$

However, we still miss a scheme within which we are actually able to compute this local self-energy. Devising such a scheme implies two ingredients [41]:

- A solvable effective model, whose self-energy is *a priori* purely local.
- A *self-consistent mapping* of the original lattice model onto the above effective one.

Connection with the Anderson Impurity Model: The model Hamiltonian describing an impurity embedded in a bath of non-interacting electrons, can be written in the form of the Anderson impurity model (AIM) [5], which reads as:

$$\hat{H}_{\text{AIM}} = \sum_{n\sigma} \epsilon_n \hat{c}^{\dagger}_{n\sigma}\hat{c}_{n\sigma} + \sum_{n\sigma} V_n(\hat{c}^{\dagger}_{n\sigma} f_{\sigma} + f^{\dagger}_{\sigma}\hat{c}_{n\sigma}) + U f^{\dagger}_{\uparrow} f_{\uparrow} f^{\dagger}_{\downarrow} f_{\downarrow}, \tag{1.16}$$

where $c^{\dagger}$ (c) and $f^{\dagger}$ (f) create (destroy) an electron on a conduction site and the impurity site, respectively; ϵ_n are the on-site energies of the non-interacting sites and V_n denotes the hybridization of the n-th site with the impurity. These two parameters – called *Anderson parameters* – together with the onsite interaction strength, U, completely define the AIM. Integrating out the trivial non-interacting part, the action of the AIM reads as [2]:

$$S_{AIM} = -\frac{1}{\beta}\int_0^{\beta} d\tau \int_0^{\beta} d\tau' \sum_{\sigma} \bar{\eta}_{\sigma}(\tau)\mathscr{G}_0^{-1}(\tau-\tau')\eta_{\sigma}(\tau') + U\int_0^{\beta} \bar{\eta}_{\uparrow}(\tau)\eta_{\uparrow}(\tau)\bar{\eta}_{\downarrow}(\tau)\eta_{\downarrow}(\tau)d\tau. \tag{1.17}$$

Here $\bar{\eta}_\sigma$ (η_σ) are the Grassman variables associated with the creation (annihilation) operators of the impurity; β is the inverse temperature. The non-interacting Green's function, $\mathscr{G}^0$, of the AIM – entering in the quadratic part of the action – is conventionally called the Weiss-field and is expressed in terms of the *Anderson parameters* of the fermionic bath as:

$$\mathscr{G}^0(\mathrm{i}\omega_n) = \mathrm{i}\omega_n + \mu - \sum_m \frac{\mid V_m \mid^2}{\mathrm{i}\omega_n - \epsilon_m} = \mathrm{i}\omega_n + \mu - \Delta(\mathrm{i}\omega_n), \tag{1.18}$$

where in the last equality he have defined the so-called *hybridization function*, $\Delta(\mathrm{i}\omega_n)$. Inspection of the action, Eq. (1.16), reveals an intuitive picture: the quadratic part describe the process in which an electron leaves the impurity at time τ', propagates freely in the fermionic bath for $\tau - \tau'$, and returns at the origin at time τ; the quartic part describes the instantaneous Coulomb interaction when the impurity is doubly-occupied. The relation between the impurity site and the non-interacting bath, is encoded in $\mathscr{G}^0$, which is nothing but the quantum counterpart of the Weiss-field of classical mean-field theory. The interacting single-particle Green's function, $G^\sigma_{\mathrm{AIM}}(i\omega_n)$ – given the AIM – action is obtained as:

$$G^\sigma_{\mathrm{AIM}}(\mathrm{i}\omega_n) = -\frac{\int \mathscr{D}[\bar{\eta}]\mathscr{D}[\eta]\bar{\eta}_\sigma\eta_\sigma e^{-S}}{\int \mathscr{D}[\bar{\eta}]\mathscr{D}[\eta]e^{-S}}, \tag{1.19}$$

and the impurity self-energy, is evaluated via the corresponding Dyson equation,

$$\Sigma_{\mathrm{AIM}}(\mathrm{i}\omega_n) = [\mathscr{G}^0(\mathrm{i}\omega_n)]^{-1} - [G_{\mathrm{AIM}}(\mathrm{i}\omega_n)]^{-1}. \tag{1.20}$$

DMFT self-consistency scheme: We can now describe the self-consistent DMFT scheme to map the original lattice model into an effective impurity problem. Since in the limit of infinite dimensions the diagrams that contribute to the self-energy are the local skeleton ones, and since by definition the diagrams that contribute to the self-energy of an AIM are also local – with local Green's functions – we can conclude that both systems are described by the same diagrammatics. Thus, assuming that the on-site Coulomb interaction of the impurity system is the same also for all sites of the lattice system, and in the case that both interacting Green's functions, G_{loc} and G_{AIM}, are the same, the corresponding self-energies evaluate the same. With these considerations we obtain,

$$G_{\mathrm{loc}}(i\omega_n) = G_{\mathrm{AIM}}(i\omega_n) \Rightarrow \sum_{\boldsymbol{k}} \Big(i\omega_n + \mu - \epsilon(\boldsymbol{k}) - \Sigma(i\omega_n) \Big)^{-1} = \Big(\mathscr{G}_0^{-1} - \Sigma_{\mathrm{AIM}}(i\omega_n) \Big)^{-1}, \tag{1.21}$$

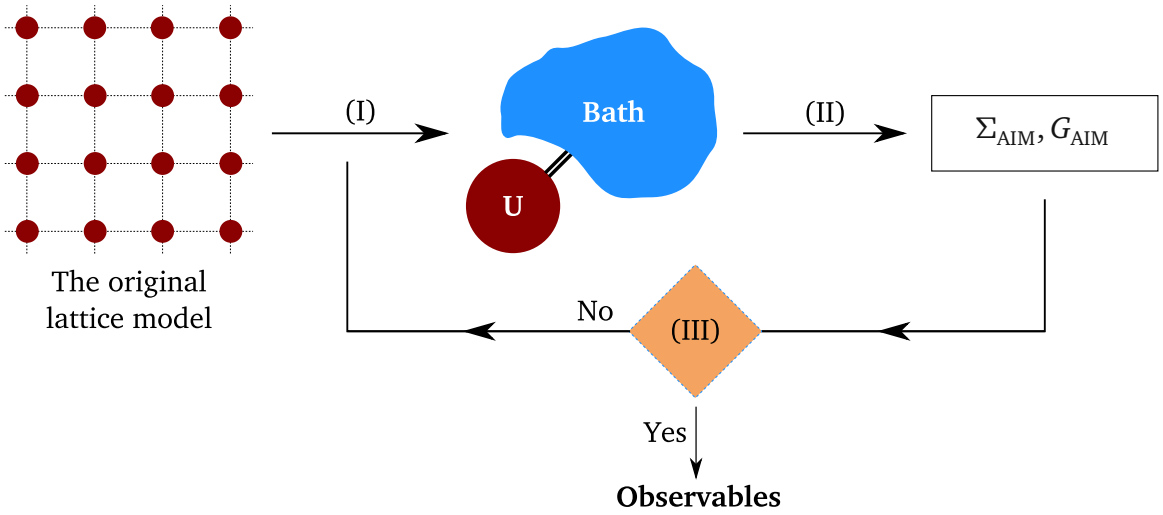

Fig. 1.7: The DMFT self-consistent scheme. Given the original lattice model we **(I)** fix the particle density – calculating the chemical potential μ – and we obtain the local Green's function of the system. Provided the interacting part of the Hamiltonian, we define and **(II)** solve the AIM. At stage **(III)** we check if the convergence criteria are met and return to stage **(I)** or exit the self-consistent loop, respectively.

which can be regarded as the **DMFT self-consistency equation**. If we are able to find the AIM whose Weiss-field and self-energy fulfill Eq. (1.21), then we will know exactly the local interacting Green's function and self-energy of the lattice system, in the limit of infinite dimensions.

In turn, to specify the self-energy, one needs to solve the impurity many-body problem, a task for which various methods have been devised – even 20 years before DMFT was formulated – and are still actively developed. A summary of the self-consistency scheme of DMFT is shown in Fig. 1.7.

1.4.2 Limitations and extensions

The limitations of dynamical mean-field theory originate both from numerical and theoretical reasons. From the numerical point of view, despite the enormous simplification of the lattice model in infinite dimensions, one is still left to deal with and overcome the full

complexity of the resulting quantum impurity model, which lies at the core of the self-consistent DMFT framework. This task is the subject of the so-called *quantum impurity solvers*, which can be classified into two main categories: analytical (AIS) and numerical (NIS) solvers. AIS are typically employed to provide approximative yet computationally inexpensive solutions involving (controlled) diagrammatic truncation schemes as in iterative perturbation theory and strong-coupling expansion, or non-crossing and slave-boson mean-field approximation, to name a few. NIS, based on e.g. different flavors of continuous-time quantum Monte Carlo (CTQMC), exact diagonalization or density-matrix renormalization group (DMRG), represent the opposite "limit": they are computationally (very) expensive but can be considered as exact. Each class comes with its own benefits and challenges hence their usage depends on the context.

For instance, the qualitative exploration of phase-diagrams over a large set of tunable parameters is often a perfect case for an AIS [32, 80]. In contrast, quantitative – or many times even qualitative [8] – studies necessitate the use of expensive NIS calculations. CT-QMC solvers [45, 46] are currently considered to be the state-of-the-art method for finite temperature simulations of multi-orbital systems with complex hybridization functions. Their computational cost scales cubicly with the number of orbitals and temperature. However, as in their lattice counterpart, they are often hampered by the fermionic sign-problem, which causes an exponential scaling in computational time for any desired accuracy. Furthermore, the measurements of the Green's functions and self-energies are obtained on the Matsubara axis, which necessitates the ill-conditioned analytic continuation to obtain results on the real axis. This systematic problem is avoided when using ED solvers [87], which operate directly on the real-frequency axis. They are, however, severely limited regarding the number of orbitals they can handle. New DMRG algorithms [16], exploiting efficient representations of the wavefunction, such as matrix-product states (MPS), seem to (partially) circumvent the exponential growth of the Hilbert space and offer a very interesting alternative for the solution of generic impurity problems.

Regarding theoretical considerations, the main limitation of DMFT is very easy to be under-

[8] Perturbative solvers cannot be expected to perform well away from the parameter space in which they are defined.

stood: only in the limit of infinite dimensions the self-energy loses it's spatial dependence and becomes local. In finite systems, however, the self-energy has also non-local part, meaning that non-local correlation effects – and thus non-local fluctuations, e.g. charge and spin fluctuations – are completely missed by DMFT. The various methods, devised during the last decades to include some portion of those missing contributions, fall into two general categories: cluster extensions [44, 91] and diagrammatics extensions [112].

- In cluster extensions, formulated either in the reciprocal space (DCA) [56, 122, 84] or in real space (cellular-DMFT)[72], the idea is to extend the single-site impurity model to a cluster of impurities embedded into the dynamical mean field bath. As DMFT accounts exactly for all local correlations on the impurity, cluster DMFT extensions will account for all local correlations within the cluster: short-range correlations will be included. Additionally, they provide a systematic way to approach the thermodynamic limit by increasing the cluster size.

- In diagrammatic extensions, non-local correlations are taken into account via inclusion of (non-local) Feynman diagrams that are not considered in DMFT. Early approaches in this context, supplemented the purely local DMFT self-energy with non-local contributions of other diagrammatic methods, i.e GW+(E)DMFT [128, 12]. Other recently developed approaches, point towards a different way to introduce non-local correlation effects. For instance, $D\Gamma A$ is formulated around the locality of the two-particle irreducible vertex $\mathbf{\Gamma}$ [133], while $TRILEX$ [13] is based on the locality of the three point 2-fermion-1-boson vertex, $\mathbf{\Lambda}$. In the same category, diagrammatic mergers like DMF^2RG can be considered too [132].

Extensions of DMFT are a current subject of active research. However, a word of caution: the extensions of DMFT typically imply a huge increase in computational cost. Cluster extensions, for instance, are rather limited by the cluster size, while diagrammatic extensions apart from being computationally expensive are also memory bound, since they deal with higher-order Green's functions. Thus, especially the treatment of multiorbital systems within these extensions is in its early stage.

1.5 Bringing two worlds together: The merger of DFT and DMFT

In the previous sections, we discussed the methodologies commonly employed either for *ab initio* calculations (DFT) or for model hamiltonians (DMFT), and we addressed their merits and limitations. Hence, it should be already evident that a realistic description of strongly-correlated materials, directly points to a combination of such concepts. Among the so-called DFT++ methods [83], the merger DFT and DMFT is currently the state-of-the-art framework [105]. It allows the inclusion of many-body effects into one or more correlated subspaces, within a material-dependent parametrization of the Hamiltonian of the system. In the following, we will describe the rationale behind this merger, alongside with its algorithmic realization and pitfalls that are usually encountered.

1.5.1 Constructing the *ab initio* Hamiltonian

In contrast with a pure model Hamiltonian study, where one usually deals with a relatively small number of orbitals and can, therefor, explicitly choose and write down the single-particle hopping integrals, $t_{ij}^{\alpha\beta}$, the description of a periodic real system (compound) is far more complicated: it typically consist of dozens of orbitals in the unit-cell, whose local structure must be properly obtained, while thousands of hopping amplitudes must be determined. On top, we know that neither all states shall be considered as relevant nor all remaining states shall be treated as correlated and *altered* by the inclusion of many-body correlation effects.

Construction of the quadratic Hamiltonian: The initial local structure and hopping integrals, $T_{ij}^{\alpha\beta}$, are obtained solely within the context of DFT, and it is assumed that they form the *non-interacting* Hamiltonian, $H^0(\boldsymbol{k}) = H^{\mathrm{DFT}}(\boldsymbol{k})$. It should not be forgotten though, that this last step is an approximation since DFT is already taking into account part of correlation effects through the exchange-correlation functional; indeed this is the source

of the so-called double-counting problem which we will discuss in Section 1.5.2.

Given the converged set of single-particle wavefunctions and eigen-energies, the next step is to construct atomic-like orbitals for the relevant energy window, $\mathscr{W}$, for which the low energy Hamiltonian will be defined. Common choices of such atomic-like localized basis, $\Psi_{i\alpha}(\mathbf{r})$ are (localized) projections [124] and linear or N-th order muffin-tin orbitals [4], while their quality is typically validated by the convergence upon the original DFT band-structure. This allows us to obtain a tight-binding representation of our system, namely the quadratic part of Eq. (1.4), as,

$$\hat{H}^0 = \sum_{ij}\sum_{\alpha\beta} T_{ij}^{\alpha\beta}\hat{c}_{i\alpha}^{\dagger}\hat{c}_{j\beta}, \tag{1.22}$$

where the hopping integrals $T_{ij}^{\alpha\beta}$ are given as,

$$T_{ij}^{\alpha\beta} = \langle \Psi_{i\alpha}(\mathbf{r})|\hat{H}_{\mathrm{DFT}}|\Psi_{j\beta}(\mathbf{r}')\rangle \tag{1.23}$$

Construction of the quartic Hamiltonian: In the DFT+DMFT framework correlation effects are generated by the interaction terms in the selected subspaces. Without loss of generality, let $\mathscr{M}$ be the set of all states in the low energy-window, namely the correlated, $\mathscr{C}$, and the uncorrelated, $\mathscr{U}$. In the same manner as in Eq. (1.4), we can define the interacting (quartic) term of the Hamiltonian, which is parametrized by the U-matrix, $U_{\alpha\beta\gamma\delta}$ with $\alpha\beta\gamma\delta \in \mathscr{C}$.

However, because of the rearrangement of all surrounding electrons upon the presence of an electron due to the Coulomb repulsion, the interaction interaction to be constructed must consider the effect of screening. The derivation of such a U-matrix, is the subject of constrained approaches, like the constrained local density approximation [48] or constrained random-phase approximation [11]. The latter, is based on the resummation of ring-diagrams to build the polarization tensor, excluding the processes within the correlated subspace $\mathscr{C}$ and generates a frequency dependent interaction $U_{\alpha\beta\gamma\delta}(i\nu_n)$. Oftentimes, the static limit – or close to the static limit – value of the interaction kernel is taken to construct the interacting Hamiltonian of the low-energy model [136], albeit this approxima-

tion neglects processes, such as plasmons, that might crucially affect the excitation spectra, as shown in references [27].

1.5.2 Double counting and self-consistent cycle

Based on the previous considerations, the Hamiltonian of the system in the energy window $\mathscr{W}$, reads:

$$\hat{H} = \sum_{ij} \sum_{\alpha\beta \in \mathscr{M}} T_{ij}^{\alpha\beta} \hat{c}_{i\alpha}^{\dagger} \hat{c}_{j\beta} + \sum_{i} \sum_{\alpha\beta\gamma\delta \in \mathscr{C}} U_{\alpha\beta\gamma\delta}^{(i)} \hat{c}_{i\alpha}^{\dagger} \hat{c}_{i\beta}^{\dagger} \hat{c}_{i\gamma} \hat{c}_{i\delta}. \tag{1.24}$$

At this point, two cases can be realized: **(i)** All states in $\mathscr{M}$ are correlated, that is $\mathscr{M} = \mathscr{C}$ and $\mathscr{U} = \emptyset$, **(ii)** uncorrelated states exists in the low energy window, $\mathscr{U} \neq \emptyset$. In the first scenario, the resulting form of the Hamiltonian is nothing but the multi-orbital generalization of the Hubbard model and DMFT can be employed directly to converge the interacting local Green's function and local self-energy of the system.

In the second case, though, additional steps must be included. As mentioned earlier, part of the correlation effects – local and non-local – are already taken into account during the DFT step. At the same time, within DMFT we are assured that we account for all local correlation effects explicitly; this would effectively lead to a double counting of some terms. Thus some form of double counting correction has to be introduced. However, the commonly used exchange-correlation functionals are non-linear and cannot be explicitly expressed in terms of Feynman diagrams – there is no *common language* between DFT and DMFT. Thus, there is no definite solution to the double-counting problem, and one typically *assumes* its form inspired by limiting cases.

The most common schemes, labeled as "around mean-field" (AMF) [10] and "fully-localized limit" (FLL) [29] correction, are constructed directly from the non-interacting (DFT) occupation numbers. Restrictions for the high-frequency asymptotic behavior of the impurity's self-energy have been also employed in the study of insulating systems, while oftentimes the double-counting term is treated as an adjustable parameter, optimized *a posteriori* upon the proximity of the converged solution to experimental results. Independently of the selected form, the double-counting correction essentially assumes a quadratic operator to be

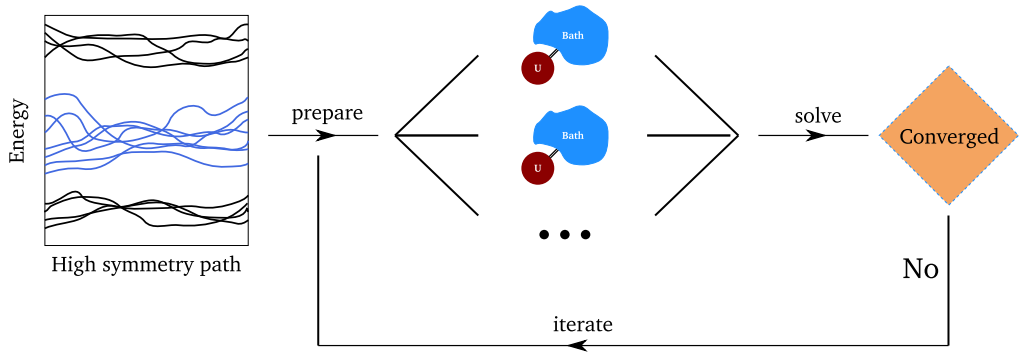

Fig. 1.8: A schematic view of the DFT+DMFT self-consistent scheme in its *one-shot* variant.

included in the Hamiltonian, as:

$$H_S \rightarrow H_S + \sum_i \sum_{\alpha\beta \in \mathscr{C}} \mu_{\mathrm{DC}} \hat{c}^\dagger_{i\alpha} \hat{c}_{i\beta}. \tag{1.25}$$

Having discussed all the preliminaries, as sketched in Fig. 1.8, the steps and decisions to be made in order to perform a self-consistent DFT+DMFT calculation – in the so-called *one-shot* variant, can be summarized as follows:

1. Perform a DFT calculations and identify the low energy-window, $\mathscr{W}$ in which the Hamiltonian will be constructed. Obtain a tight-binding representation of the Hamiltonian, $H_0(\mathbf{k})$ (Wannierization).
2. Label the subspaces, c_i, of the Hamiltonian to be treated as correlated. Parametrize the interaction kernel and assume a form of the double-counting correction for each correlated subspace.
3. Obtain the local lattice Green's function – in the first cycle the all self-energies can be set equal to the corresponding double-counting correction – as,

$$G^{\mathscr{W}}_{\mathrm{loc}} = \frac{1}{N_k} \sum_k \frac{1}{i\omega_n + \mu - H_0(\mathbf{k}) - \Sigma^{\mathscr{W}}(i\omega_n)}, \tag{1.26}$$

where the self-energy in the full space is constructed as,

$$\Sigma^{\mathscr{W}}(i\omega_n) = \begin{pmatrix} \Sigma^{(1)} & 0 & 0 & 0 \\ 0 & \Sigma^{(2)} & 0 & 0 \\ 0 & 0 & \dots & 0 \\ 0 & 0 & 0 & 0 \end{pmatrix} - \begin{pmatrix} \Sigma^{(1)}_{\mathrm{DC}} & 0 & 0 & 0 \\ 0 & \Sigma^{(2)}_{\mathrm{DC}} & 0 & 0 \\ 0 & 0 & \dots & 0 \\ 0 & 0 & 0 & 0 \end{pmatrix} \tag{1.27}$$

with $\Sigma^{(i)}$ and $\Sigma^{(i)}_{\mathrm{DC}}$ being the self-energy and double-counting correction of the correlated subspace i.

4. Solve independently the AIMs defined the Weiss-field,

$$\mathscr{G}_0^{(i)} = \left[\Sigma^{(i)} + [G^{(i)}_{\mathrm{loc}}]^{-1}\right]^{-1}, \tag{1.28}$$

and the interaction $\hat{H}^{(i)}_{\mathrm{int}}$, where the local Green's function of the i-th subspace is obtained by the projection operator P_i as $G^{(i)}_{\mathrm{loc}} = P_i G^{\mathscr{W}}_{\mathrm{loc}} P_i^{\dagger}$.

5. Iterate over steps 3 and 4 until the convergence criteria are met.

1.6 Observables and connection to experiments

This section is devoted to the physical observables that one is able to obtain upon solving a corresponding model Hamiltonian, always in the context of DMFT (or DFT+DMFT). That is, we ask which physical information can be extracted given the non-interacting Hamiltonian together with the converged local Green's function and self-energy. Furthermore, we assume that the solution of the impurity problem is obtained on the imaginary (Matsubara) axis as is the case for most impurity solvers, based on Quantum Monte Carlo (QMC) implementations.

1.6.1 The problem of analytical continuation

Most experiments probe dynamical quantities directly on the real-frequency axis, e.g single-particle spectral functions. In turn, the (local) spectral-function, $A(\omega)$ and the retarded

single-particle Green's function, $G^R_{\rm loc}(\omega)$ are connected as

$$A(\omega) = \frac{1}{\pi}\mathrm{Im}G^R_{\rm loc}(\omega). \tag{1.29}$$

The connection between $A(\omega)$ (target-quantity) and the imaginary-time single-particle Green's function $G(\tau)$ (obtained during simulation) is given – in the continuum – by,

$$G_{\rm loc}(\tau) = \int d\omega \mathscr{K}(\tau,\omega)A(\omega) \rightarrow G_\tau = \mathscr{K}_{\tau\omega}A_\omega, \tag{1.30}$$

where, for the right-hand side, we have assumed a discrete time and frequency mesh; this is the case for all numerical simulations. $\mathscr{K}(\tau,\omega)$ is the kernel of the transformation which in the fermionic case reads,

$$\mathscr{K}(\tau,\omega) = \frac{e^{-\tau\omega}}{1+e^{-\beta\omega}}, \tag{1.31}$$

with $\beta = \frac{1}{\kappa_B T}$ being the inverse temperature. A direct inversion of the matrix equation to retrieve the spectral function, $A = \mathscr{K}^{-1}G$ is futile. The exponential decay of the kernel transformation corresponds to a very large *condition number* of the above procedure [23], meaning that even small variations of the input vector (G) significantly change the resulting output vector (A): the analytical continuation is an ill-conditioned problem. The advancements and/or the development of algorithms and methods to deal with it is an active field of research. Among other methods [47, 76], the Maximum Entropy Method (MEM) [119, 47, 120], which is based on the Bayes theorem, has been proven to be the most successful. Here we will recapitulate only the basic idea of the MEM, while for the interested reader we refer to [61]. The basic idea of MEM, in order to circumvent the ill-conditioned relation Eq. (1.30), is to construct, instead, the (statistically) *best* spectral function $A(\omega)$ that gives the correct $G(\tau)$, in terms of analytic properties.

The arguments are based on the Bayes theorem stating that the joint probability of two stochastic samples X and Y, $P[X,Y]$, is given as:

$$P[X,Y] = P[X|Y]P[Y] = P[Y|X]P[X], \tag{1.32}$$

where $P[X|Y]$ is the conditional probability of having X given Y. The purpose of the MEM algorithm is to exactly maximize the *posterior* functional $P[A(\omega)|G(\tau)]$, which is calculated as:

$$P[A(\omega)|G(\tau)] = P[G(\tau)|A(\omega)]\frac{P[A(\omega)]}{P[G(\tau)]} \tag{1.33}$$

where $P[G(\tau)|A(\omega)]$ is called the *likelihood* function. It estimates the probability of finding the actual $G(\tau)$ given the spectral function $A(\tau)$, and typically is calculated as:

$$P[G(\tau)|A(\omega)] \propto \exp\left[a \int d\omega \left(A(\omega) - D(\omega) - A(\omega) \ln \frac{A(\omega)}{D(\omega)}\right)\right] = \exp[aS] \qquad (1.34)$$

where S is called information entropy, a is an adjustable hyper-parameter and $D(\omega)$ is the so-called default model: it is used as the initial point for the spectral function and to enforce its analytic properties, e.g. normalization. Note, however, that the default model should not impact the resulting $A(\omega)$, given that the stochastically generated $G(\tau)$ data have relatively small noise.

Complementary, obtaining the self-energy in real frequencies allows us to retrieve various properties of the system which can are of experimental interest, including for instance Fermi-surfaces, k-resolved or local spectral functions, renormalization factors e.t.c.. However, the AC procedure of the $\Sigma(\omega)$ is a more subtle issue, since a corresponding spectral representation does not exist, and various methodologies have been employed. For example, one could analytically continue both the local non-interacting and the local interacting Green's functions and use the Dyson equation to obtain the $\Sigma(\omega)$. However, such a procedure tends to give unsatisfactory results as there are two independent analytical continuations involved, leading to strong oscillations of the results. Another approach, considered to be more stable, is to exploit the AC of an auxiliary (mock) Green's function – which fulfills all necessary analytic properties – and reconstruct the objective $\Sigma(\omega)$ from $G_{\text{aux}}(\omega)$.

Chapter 2

Perturbative approaches around reference points

The scope of this chapter is to discuss two different methodologies that can be employed when a clear separation of the primary energy scales, namely the itinerant and interacting, exists. In such systems, which lie in the proximity of the exactly solvable reference points – the non-interacting and the atomic-limit one –, diagrammatic expansions with respect to the *remaining* inferior energy scale formally hold and offer an alternative approach to access physical observables both at the one- and two-particle level, albeit the limits of their applicability are often debatable.

2.1 The multi-orbital Random Phase Approximation

There are three interconnected parts involved for a theoretical description of a (realistic) system: **(i)** the construction of a microscopic model, preferably as minimal as possible, which we hypothesize to capture the essential physical mechanisms that are present, **(ii)** the *solution* of the corresponding model to access its physical properties and **(iii)** the cross-validation of points **(i)**, **(ii)** against the *actual* experimentally obtained observables of the

corresponding system. In turn, experimental setups are designed under the principle of probing the response of a given system upon (usually weak) external perturbations and indirectly extracting its so-called susceptibility, which as the name suggests describes how susceptible is the system upon such a perturbation.

Although the comparison of a microscopic theory with the experiment commence (usually) from one-particle quantities – for instance single-particle spectral functions compared with ARPES [31] experimental data –, most experiments, such as Raman spectroscopy or inelastic neutron scattering [28], require access to high-in-order correlators from the theoretical side, in particular two-particle Green's functions.

Devising methodologies and approximations to obtain the latter is currently an active field of research. Here, we will discuss the matrix formalism of the random-phase approximation that allows the study of multi-orbital model Hamiltonians regarding their response functions and has been employed for the study of a generic t_{2g}-model presented in Chapter 4.

2.1.1 Linear response theory

Let us assume that the system in thermodynamic equilibrium is described by the (time-independent) Hamiltonian $\hat{H} - \mu\hat{N}$. Furthermore, we consider an external field, $F_m(t)$, with $F_m(t = -\infty) = 0$, that acts on our system and couples to the m-th component of an operator $\hat{B}$, so that it reads:

$$\hat{H}_1(t) = \sum_m B_m F_m(t) \quad \text{with} \quad [\hat{H}_1(t), \hat{N}] = 0. \tag{2.1}$$

From statistical mechanics, we know that the expectation value $\langle\, \hat{A}(t)\, \rangle$ of any operator $\hat{A}$ at time t will be given by

$$\langle\, \hat{A}(t)\, \rangle \equiv \langle \hat{A} \rangle_t = \mathrm{Tr}[\rho(t) A] = \mathrm{Tr}[\rho_0\, A] + \mathrm{Tr}[\rho_1(t)\, A]. \tag{2.2}$$

The last equality in Eq. (2.2) is obtained by defining the density-matrix of the system at time t, $\rho(t)$, as

$$\rho(t) = \rho + \rho_1(t) \quad \text{with} \quad \rho_1(t=-\infty) = \rho = \frac{e^{-\beta(\hat{H}-\mu\hat{N})}}{\mathrm{Tr}[e^{-\beta(\hat{H}-\mu\hat{N})}]}. \tag{2.3}$$

The last equation states that at $t = -\infty$ the system is at equilibrium with no perturbation applied. In turn, the density-matrix satisfies the *Liouville-von Neumann* equation of motion [25]:

$$i\,\frac{d\rho(t)}{dt} = [H, \rho_1(t)] + [H_1(t), \rho] + [H_1(t), \rho_1(t)]. \tag{2.4}$$

The last term of Eq. (2.4) is at least of second order in terms of the applied field and we can restrict ourselves to include only terms up to first order. Thus, we are left only with the *linear* terms, namely,

$$i\,\frac{d\rho_1(t)}{dt} = [H, \rho_1(t)] + [H_1(t), \rho], \tag{2.5}$$

The above differential equation which can be easily solved and yields:

$$\rho_1(t) = -i \int_{-\infty}^{t} dt'\; e^{i(\hat{H}-\mu\hat{N})(t'-t)}\,[H_1(t'), \rho]\, e^{-i(\hat{H}-\mu\hat{N})(t'-t)}. \tag{2.6}$$

By substituting Eq. (2.6) and Eq. (2.1) into Eq. (2.2), we obtain,

$$\langle \hat{A} \rangle_t = \langle \hat{A} \rangle_0 - i \sum_m \int_{-\infty}^{t} dt'\; \mathrm{Tr}\Big[e^{i(H-\mu N)(t'-t)}\,[\hat{B}_m, \rho]\, e^{-i(H-\mu N)(t'-t)}\,\hat{A}\Big] F_m(t'), \tag{2.7}$$

where $\langle \ldots \rangle_0$ denotes the expectation value calculated on the unperturbed system. Introducing the Heisenberg picture for the operators $\hat{A}, \hat{B}_m$, Eq. (2.7) can be rewritten into:

$$\langle\, \hat{A}\, \rangle_t - \langle\, \hat{A}\, \rangle_0 = -i \sum_m \int_{-\infty}^{t} dt' \langle\, [\hat{A}(t), \hat{B}_m(t')]\, \rangle\, F_m(t'). \tag{2.8}$$

Introducing the definition of the retarded (bosonic) Green's function,

$$\chi^{r}_{AB_m}(t, t') = -i\Theta(t-t') \langle\, [\hat{A}(t), \hat{B}_m(t)]\, \rangle_0, \tag{2.9}$$

we end up to the so-called *Kubo formula* [78],

$$\langle \hat{A} \rangle_t - \langle \hat{A} \rangle_0 = \sum_m \int_{-\infty}^{+\infty} dt' \chi^r_{AB_m}(t,t') F_m(t'), \tag{2.10}$$

or, equivalently, written in the frequency domain,

$$\langle \delta\hat{A}_\omega \rangle = \sum_m \chi_{AB_m}(\omega) F_m(\omega), \tag{2.11}$$

where $\langle \delta\hat{A} \rangle$ is the response of the system due to the effect of the perturbation. From a phenomenological point of view, the coefficients χ_{AB_m} connect the experimentally accessible response of the system with the corresponding applied field and are conventionally called *susceptibilities*. They fulfill all properties of bosonic Green's functions, e.g. sum rules and Kramers-Kronig relations, while they directly encode the causality principle [43].

2.1.2 Mathematical formulation

In the previous section, we derived a fundamental expression to connect the action of a field on our system with its response and found that the intrinsic properties that govern this connection are encoded in the so-called susceptibility of the system. The methodology to evaluate the corresponding susceptibility for a given model is the subject of this part.

More specifically, we will assume that the unperturbed system is characterized by translational symmetry and is time-independent, thus the susceptibility depends solely on spatial and time differences, namely:

$$\chi_{AB}(\boldsymbol{r}-\boldsymbol{r'}, \tau-\tau') = \langle \hat{\mathcal{T}} \{ \hat{A}(\boldsymbol{r},\tau)\, \hat{B}(\boldsymbol{r'},\tau') \} \rangle. \tag{2.12}$$

Note, that here we have transformed the notation onto the imaginary axis, due to the analytical properties that Green's functions, in general, fulfill. The expectation value $\langle \ldots \rangle$ is assumed with respect to the full (interacting) Hamiltonian of the system. The operator $\hat{\mathcal{T}}$ is the time-ordering operator whose action (for the bosonic case) is defined as:

$$\hat{\mathcal{T}} \{ \hat{M}(\tau)\, \hat{P}(\tau') \} = \Theta(\tau-\tau') \hat{M}(\tau) \hat{P}(\tau') + \Theta(\tau'-\tau) \hat{P}(\tau') \hat{M}(\tau). \tag{2.13}$$

The single particle operators $\hat{A}, \hat{B}$ can be expressed in terms of fermionic creation and annihilation operators and thus Eq. (2.12) can be rewritten as:

$$\begin{aligned}\chi_{AB}(\boldsymbol{r}-\boldsymbol{r'},\tau-\tau') &= \sum_{ijkl} A_{ij}B_{kl}\langle\, \hat{\mathscr{T}}\left\{\hat{c}_i^\dagger(\boldsymbol{r},\tau)\hat{c}_j(\boldsymbol{r},\tau)\hat{c}_k^\dagger(\boldsymbol{r'},\tau')\hat{c}_l(\boldsymbol{r'},\tau')\right\}\,\rangle \\ &= \sum_{ijkl} A_{ij}B_{kl}\ \chi^{\text{gen}}_{ijkl}(\boldsymbol{r}-\boldsymbol{r}',\tau-\tau'). \end{aligned} \tag{2.14}$$

Here, the Latin letters i, j, k, l stand for composite spin-orbital indices that label the chosen single-particle basis in which the matrix representation of the operators is obtained; χ^{gen}_{ijkl} is the generalized susceptibility of the system. Note that Eq. (2.14), suggests that the knowledge of the generalized susceptibility allows us to evaluate any physical susceptibility generated from the set of operators $\{\hat{A}, \hat{B}\}$ and that χ_{AB} is nothing but a *tensor contraction* of the χ^{gen}_{ijkl}.

Non-interacting limit

We will start from the non-interacting limit in which a specific element of the generalized susceptibility reads,

$$\chi^{\text{gen}}_{ijkl}(\boldsymbol{q},\tau-\tau') = \sum_{\boldsymbol{k},\boldsymbol{k'}}\langle\, \hat{\mathscr{T}}\left\{\hat{c}_i^\dagger(\boldsymbol{k}+\boldsymbol{q},\tau)\hat{c}_j(\boldsymbol{k},\tau)\hat{c}_k^\dagger(\boldsymbol{k}-\boldsymbol{q},\tau')\hat{c}_l(\boldsymbol{k'},\tau')\right\}\,\rangle_0 \tag{2.15}$$

where we have performed a Fourier transformation to the reciprocal space (since our Hamiltonian has translational symmetry). Making use of the Wick's theorem [35] – which applies since the expectation value is taken with respect to the non-interacting system – and recalling the definition of the non-interacting single-particle Green's function,

$$G^0_{\alpha\beta}(\boldsymbol{k},\tau-\tau') = -\langle\, \hat{\mathscr{T}}\{\hat{c}_\beta(\boldsymbol{k},\tau)\hat{c}_\alpha^\dagger(\boldsymbol{k},\tau')\}\,\rangle_0, \tag{2.16}$$

we can rewrite Eq. (2.15) as,

$$\chi^{0,\text{gen}}_{ijkl}(\boldsymbol{q},\tau) = \sum_{\boldsymbol{k},\boldsymbol{k'}} G^0_{ji}(\boldsymbol{k},0)G^0_{lk}(\boldsymbol{k'},0)\delta_{\boldsymbol{q},0} - \sum_{\boldsymbol{k}} G^0_{li}(\boldsymbol{k}+\boldsymbol{q},-\tau)G^0_{jk}(\boldsymbol{k},\tau). \tag{2.17}$$

In terms of Feynman diagrams, the first contribution on the right-hand side of Eq. (2.1.2) is represented by a disconnected diagram and can be conveniently neglected in all orders

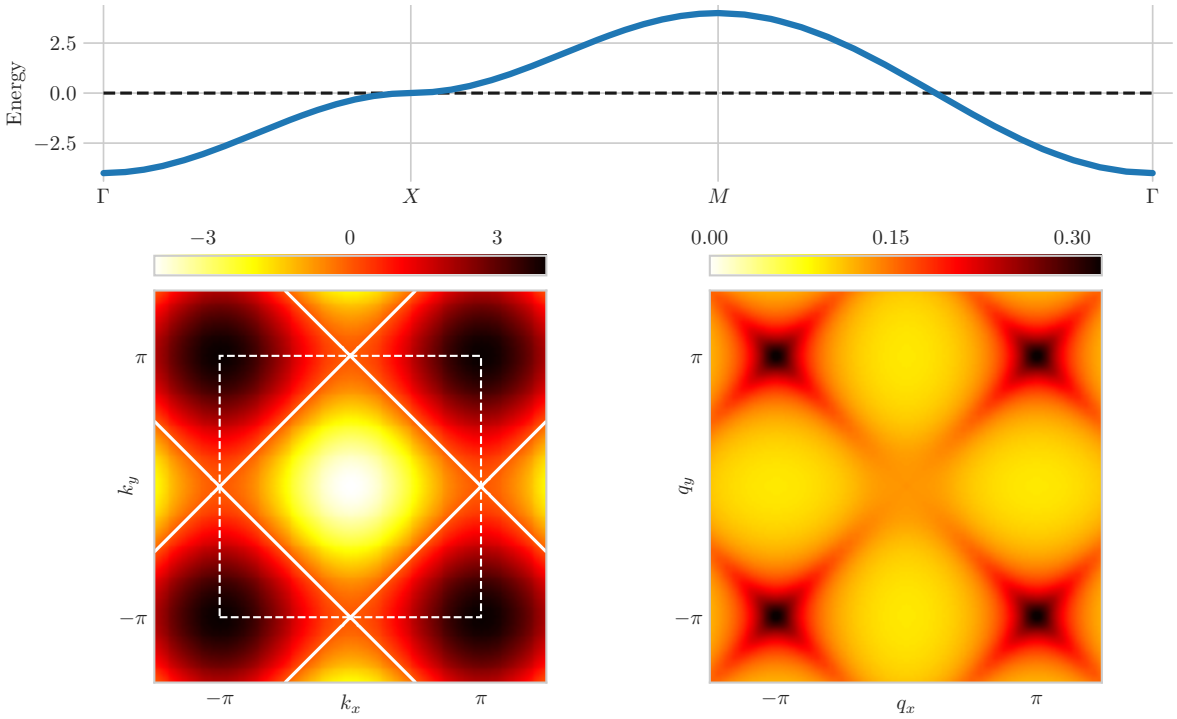

Fig. 2.1: Example case: the two-dimensional single band Hubbard model described by the dispersion relation $\varepsilon_{\mathbf{k}} = -2t\ (\cos k_x + \cos k_y)$, with $t = 1$ setting the energy units. (upper panel) Band-structure along the high-symmetry points of the Brillouin-zone. Dashed line corresponds to the assumed chemical potential. (lower left) The Fermi surface of the above model. Full lines correspond to the perfect nesting condition. Dashed lines denote the boundaries of the Brillouin zone. (lower right) The static non-interacting generalized susceptibility as obtained by a direct evaluation of the Lindhard formula. Due to $SU(2)$ symmetry all non-zero elements of the tensor are equal.

of the perturbation expansion due to the linked cluster theorem [68]. The remaining term describes the propagation of a particle-hole pair in the non-interacting system and is conventionally named *ring* or *bubble* diagram, due to its diagrammatic representation. To this end, and by Fourier transforming from the imaginary time domain into the Matsubara frequency one, the non-interacting generalized susceptibility reads:

$$FT[\chi^{0,\mathrm{gen}}_{ijkl}(\boldsymbol{q},\tau)] \rightarrow \chi^{0,\mathrm{gen}}_{ijkl}(\boldsymbol{q},i\nu_n) = -\frac{1}{\beta}\sum_{\boldsymbol{k}}\sum_{\omega_n} G^0_{li}(\boldsymbol{k}+\boldsymbol{q},i\omega_n+i\nu_n)G^0_{jk}(\boldsymbol{k},i\omega_n), \quad (2.18)$$

where $\omega_n = \frac{(2n+1)\pi}{\beta}$ and $\nu_n = \frac{2n\pi}{\beta}$ are the fermionic and the bosonic Matsubara frequencies, respectively. As an example, in Fig. 2.1, we show the bare (non-interacting) susceptibility, $\chi^{0,\mathrm{gen}}_{ijkl}$, for a single-band Hubbard model defined through the dispersion relation $\varepsilon_{\boldsymbol{k}}$, as obtained analytically using the *Lindhard formula* [98]:

$$\chi^{0,\mathrm{gen}}(\boldsymbol{q}, i\nu_n) = \frac{1}{N_k}\sum_{\boldsymbol{k}} \frac{f(\varepsilon_{\boldsymbol{k}}) - f(\varepsilon_{\boldsymbol{k}+\boldsymbol{q}})}{i\nu_n + \varepsilon_{\boldsymbol{k}+\boldsymbol{q}} - \varepsilon_{\boldsymbol{k}}}. \tag{2.19}$$

Note that due to the $SU(2)$ symmetry of the model, only four components of the non-interacting generalized susceptibility are non-zero (and actually equal), namely: $\chi^{0,\mathrm{gen}}_{\sigma\sigma\sigma\sigma}$ and $\chi^{0,\mathrm{gen}}_{\sigma\sigma'\sigma'\sigma}$ for $\sigma \in [\uparrow, \downarrow]$.

Introducing interactions

To consider the effect of the interactions on the generalized susceptibility we can follow the conventional many-body perturbation methodology in order to generate all possible higher-in-order diagrams using again the Wick's theorem. A controlled approximation to evaluate such a series of infinite diagrams assumes a resummation of a subset of diagrams whose expansion series does not diverge.

Such an approximation is the random phase approximation (RPA) [22] which is built upon the idea that only the terms involving particle-hole susceptibilities for a given wavevector $\boldsymbol{q}$ and frequency ν_n add up coherently, while the contribution of all other diagrams is suppressed due to their random phase [3]. The calculation of the generalized susceptibility within RPA results in a summation of diagrams with bubble and ladder topology up to infinite order and diagrammatically reads:

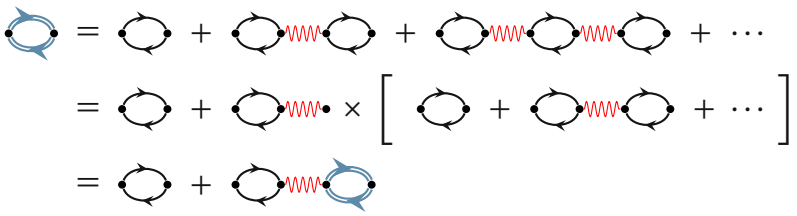

which translates into an algebraic form as,

$$\boldsymbol{\chi}^{\mathrm{gen}}(\boldsymbol{q}, i\nu_\nu) = \frac{\boldsymbol{\chi}^{0,\mathrm{gen}}(\boldsymbol{q}, i\nu_\nu)}{1 - \boldsymbol{\chi}^{0,\mathrm{gen}}(\boldsymbol{q}, i\nu_\nu)\, \boldsymbol{U}}, \tag{2.20}$$

where we explicitly use bold-face letters to denote the matrix character of the building blocks $\boldsymbol{\chi}^{\mathrm{gen}}, \boldsymbol{\chi}^{0,\mathrm{gen}}$ and the corresponding $\boldsymbol{U}$ interaction. Note that the denominator of Eq. (2.20) shall be understood as a matrix inversion operation. As such, the very ability to invert the denominator – non-trivial determinant – sets the *hard* limit of the applicability of the RPA: for fixed $\boldsymbol{\chi}^{0,\mathrm{gen}}$ and for a critical U_c the denominator is not invertible, thus signalizing the breakdown of the assumed diagrammatic resummation.

The main benefit of the matrix generalization of RPA is its efficiency; the computational cost is generated solely from (multiple) matrix operations and has a rather small memory-footprint, since the mathematical objects involved scale as $N_s^4 \times N_{\mathbf{q}} \times N_{\nu_n}$, where N_s is the number of single-particle states, $N_{\mathbf{q}}$ is the number of $\boldsymbol{q}$-points and N_{ν_n} is the number of bosonic Matsubara frequencies.[1] For general realistic multiorbital systems, where the Fermi surface typically consist of several Fermi sheets, oftentimes the RPA is the only methodology to obtain lattice generalized response functions, although its validity is still debatable even in the weak coupling regime.

Physical susceptibilities

The solution of Eq. (2.20) results in the determination of the $\chi^{\mathrm{gen}}_{ijkl}$ tensor which, in turn, allows us to access any physical susceptibility by simply applying Eq. (2.14). In continuation of our previous example, in Fig. 2.2, we visualize the static spin and charge susceptibilities along the high symmetry path on the Brillouin zone. For fixed temperature and increasing onsite interaction strength, the spin susceptibility dominates and finally diverges at a critical value of $U_c = 1.47$, signalizing a phase transition from the normal state (NS) onto the (checkerboard) antiferromagnetic (AF) one. This phase transition is driven by the perfect

[1] Note that this is the upper limit of the memory scaling. In practice, various symmetries can be exploited and lead to significant reduction of computational cost.

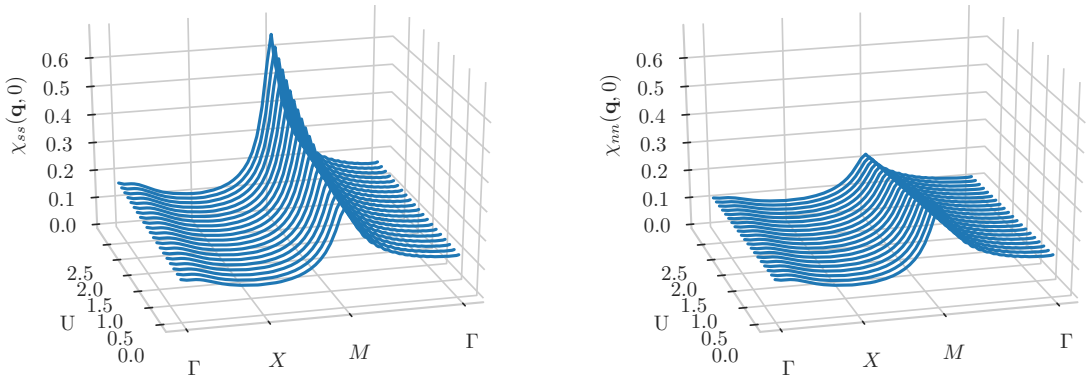

Fig. 2.2: Interacting physical susceptibilities obtained with the RPA for the model defined in Fig. 2.1. (left) The static spin-spin response function, $\chi_{ss}(\boldsymbol{q},0)$, along the high symmetry points of the Brillouin zone. (right) The static density-density response function, $\chi_{nn}(\boldsymbol{q},0)$, along the high symmetry points of the Brillouin zone.

nesting of the assumed Fermi surface and could be foreseen already from the pole structure of the non-interacting generalized response.

At this point, it is important to note that although the RPA is known to be overtaken by the structure of the Fermi surface, for multiorbital systems attributing or rationalizing divergences based solely on nesting conditions can lead to wrong estimates due to the matrix form of the interaction kernel.

An alternative view of RPA: The Bethe-Salpeter equation

Previously we derived a closed form for the generalized susceptibility in the context of (matrix) RPA based on a mere diagrammatic expansion and summation of diagrams of a particular topology. Another approach to conceptualize RPA is to view it in the context of the *Bethe-Salpeter equations* (BSEs) [94]. The BSEs are the two-particle equivalent of the one-particle Dyson equation and formally read,

$$\chi^{\text{gen}} = \chi^{0,\text{gen}} + \chi^{0,\text{gen}} \boldsymbol{F}_{ch} \chi^{0,\text{gen}}, \tag{2.21a}$$

$$\boldsymbol{F}_{ch} = \boldsymbol{\Gamma}_{ch} + \boldsymbol{\Gamma}_{ch} \chi^{0,\text{gen}} \boldsymbol{F}_{ch}, \tag{2.21b}$$

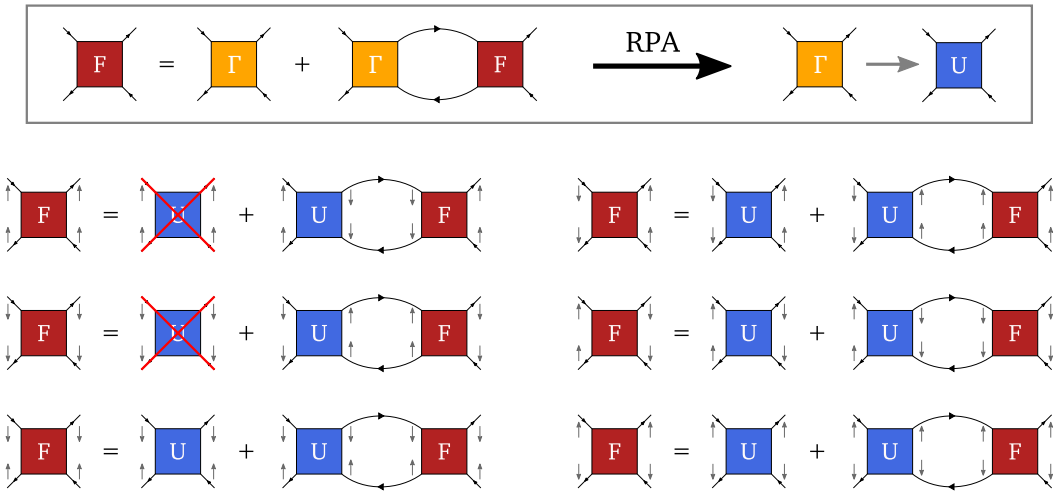

Fig. 2.3: (i) Diagrammatic view of the Bethe-Salpeter equations. (ii) In the case of the single-band Hubbard model and due to $SU(2)$ symmetry only 6 out of 16 equations remain to be solved, while they can be further *diagonalized*. The RPA corresponds to approximating the two-particle vertex Γ with the bare interaction kernel U.

where $\boldsymbol{F}$ is the fully connected vertex and $\boldsymbol{\Gamma}$ is the fully irreducible vertex, which in principle depend on three Matsubara frequencies and three momenta (note that in Eq. (2.21) we imply integrations over repeated internal indices and arguments). The subscript denotes the so-called channel of reducibility. Their explicit calculation corresponds to the evaluation of all diagrams up to infinite order, a task which is unfeasible from a computational perspective.

In that respect, RPA can be viewed as the zero order approximation of the $\boldsymbol{\Gamma}$ vertex, which is nothing but the bare interaction kernel, together with the restriction of remaining only on the particle-hole channel of the BSEs. Within these considerations, the BSEs – coupled with respect to the spin-orbital indices – reduce to our earlier result of Eq. (2.20).

2.2 Strong coupling approximation impurity solver

As we have already reviewed in Sec. 1.4.2, the development of both analytical or numerical approaches to solve the underlying quantum impurity model that lies at the core of DMFT is an active field of research by its own. Here, we will describe a (semi-) analytical impurity solver, which is based on a finite expansion with respect to the hybridization around the atomic-limit [30]. Besides its mathematical formulation, we will refer to the critical implementation details that need to be considered and we will discuss about the possible usage cases, as well as the accompanying limitations.

2.2.1 Mathematical formulation

Following Ref. [30], our starting point for the formulation of the impurity solver will be the multiorbital generalization of the AIM which reads as,

$$\hat{H}_{\mathrm{AIM}} = \hat{H}_{\mathrm{imp}} + \hat{H}_{\mathrm{bath}} + \hat{H}_{\mathrm{hyb}}, \tag{2.22}$$

where we have decoupled the corresponding degrees of freedom to explicitly denote the *atomic-like* part $\hat{H}_{\mathrm{imp}}$, the non-interacting fermionic bath, $\hat{H}_{\mathrm{bath}}$, and the hybridization between them, $\hat{H}_{\mathrm{hyb}}$.

In particular, each term is defined as,

$$\hat{H}_{\mathrm{imp}} = \sum_{\alpha\beta} h^{\mathrm{loc}}_{\alpha\beta} f^{\dagger}_{\alpha} f_{\beta} + \sum_{\alpha\beta\gamma\delta} U_{\alpha\beta\gamma\delta} f^{\dagger}_{\alpha} f^{\dagger}_{\beta} f_{\gamma} f_{\delta} \tag{2.23a}$$

$$\hat{H}_{\mathrm{bath}} = \sum_{\mathbf{k},a} \varepsilon_{\alpha}(\mathbf{k}) \hat{c}^{\dagger}_{\mathbf{k}\alpha} \hat{c}_{\mathbf{k}\alpha} \tag{2.23b}$$

$$\hat{H}_{\mathrm{hyb}} = \sum_{\mathbf{k}\alpha\beta} V_{\mathbf{k}\alpha\beta} f^{\dagger}_{\alpha} \hat{c}^{\dagger}_{\mathbf{k}\beta} + h.c. \tag{2.23c}$$

Here, greek letters denote composites of spin-orbital indices, $f^{\dagger}_{\alpha}$ (f_{α}) and $\hat{c}^{\dagger}_{\mathbf{k}\alpha}$ ($\hat{c}_{\mathbf{k}\alpha}$) create (destroy) electrons on the impurity site and on the bath, respectively; $V_{\mathbf{k}\alpha\beta}$ stands for the strength of the hybridization between the fermionic non-interacting bath and the impurity.

Assuming that the impurity Hamiltonian, $\hat{H}_{\text{imp}}$, can be fully diagonalized and yields,

$$\hat{H}_{\text{imp}} \xrightarrow{\text{diag}} \sum_l E_l |l\rangle\langle l| \,, \tag{2.24}$$

the atomic-limit Green's function can be simply computed through the Lehmann representation,

$$G^{\text{atom}}_{\alpha\beta}(i\omega_n) \equiv -\int_0^\beta d\tau\; e^{-i\omega_n\tau}\langle \mathscr{T}_\tau f_\alpha(\tau) f^\dagger_\beta(0)\rangle = \frac{1}{Z}\sum_{ll'} \frac{F^\alpha_{ll'} F^{\beta,\dagger}_{l'l}\left(e^{-\beta E_l} + e^{-\beta E_{l'}}\right)}{i\omega_n - E_{l'} + E_l}, \tag{2.25}$$

where Z is the atomic partition function and F^α ($F^{\alpha,\dagger}$) is the matrix representation of the fermionic operator f_α in the full eigenbasis, $|l\rangle$ of the atomic Hamiltonian. The atomic self-energy can be obtained via the Dyson equation,

$$\Sigma^{\text{atom}}(i\omega_n) = [G^{0,\text{atom}}(i\omega_n)]^{-1} - [G^{\text{atom}}(i\omega_n)]^{-1}, \tag{2.26}$$

where $G^{0,\text{atom}}(i\omega_n)$ is the non-interacting atomic Green's function. Considering the effect of the hybridization with the non-interacting bath – encoded in the hybridization function $\Delta(i\omega_n)$ – perturbatively, the interacting Green's function of the system reads,

$$G(i\omega_n) = G^{\text{atom}}(i\omega_n) + G[\Delta](i\omega_n) + G[\Delta^2](i\omega_n) + \ldots. \tag{2.27}$$

Up to second order expansion with respect to the hybridization elements, $V_{\mathbf{k}\alpha\beta}$, the self energy of the system becomes

$$\Sigma(i\omega_n) = \Sigma^{\text{atom}}(i\omega_n) + [G^{\text{atom}}(i\omega_n)]^{-1} G[\Delta](i\omega_n)[G^{\text{atom}}(i\omega_n)]^{-1} - \Delta(i\omega_n). \tag{2.28}$$

The correction to the atomic Green's function can be analytically obtained [96] and is given by,

$$G[\Delta] \equiv G^{(2)}_{\alpha\beta}(i\omega_n) = \beta G^{\text{atom}}_{\alpha\beta}(i\omega_n)\text{Tr}[G^{\text{atom}}\Delta] + G^{\text{amp}}_{\alpha\beta}(i\omega_n), \tag{2.29}$$

where $G^{\text{amp}}_{\alpha\beta}(i\omega_n)$ is the two-particle amputated Green's function. The latter is given by,

$$G^{\text{amp}}_{\alpha\beta}(i\omega_n) = \int_0^\beta \int_0^\beta \int_0^\beta d\tau_1 d\tau_2 d\tau_3 e^{-i\omega_n\tau_1} \sum_{\gamma\delta} \langle \mathscr{T}_\tau\; f_\alpha(\tau_1) f^\dagger_\beta(0) f^\dagger_\gamma(\tau_2) f_\delta(\tau_3)\rangle_{\text{A}} \Delta_{\gamma\delta}(\tau_2 - \tau_3), \tag{2.30}$$

with the thermal averaged $\langle \dots \rangle_{\mathrm{A}}$ to be computed with respect to the atomic system. Inserting the matrix-representation of the fermionic creation and annihilation impurity operators and after analytical integration one arrives at:

$$\begin{aligned} G^{\mathrm{amp}}_{\alpha\beta}(i\omega_n) = \sum_{IJKL}\sum_{\gamma\delta} & F^{\alpha}_{IJ}F^{\gamma,\dagger}_{JK}F^{\delta}_{KL}F^{\beta,\dagger}_{LI}\big(R^{JK}_{\gamma\delta}E^{-1}_{JL}\Omega_{JI} + R^{LK}_{\gamma\delta}E^{-1}_{LJ}\Omega_{LI} + Q^{IK}_{1,\gamma\delta}\Omega_{JI}\Omega_{LI}\big) \\ & + F^{\alpha}_{IJ}F^{\delta}_{JK}F^{\gamma,\dagger}_{KL}F^{\beta,\dagger}_{LI}\big(R^{KJ}_{\gamma\delta}E^{-1}_{JL}\Omega_{JI} + R^{KL}_{\gamma\delta}E^{-1}_{LJ}\Omega_{LI} - Q^{KI}_{2,\gamma\delta}\Omega_{JI}\Omega_{LI}\big) \\ & + F^{\gamma,\dagger}_{IJ}F^{\delta}_{JK}F^{\alpha}_{KL}F^{\beta,\dagger}_{LI}\big(R^{KJ}_{\gamma\delta}E^{-1}_{KI}\Omega_{LK} + R^{IJ}_{\gamma\delta}E^{-1}_{IK}\Omega_{LI} - Q^{LJ}_{2,\gamma\delta}\Omega_{LI}\Omega_{LK}\big) \\ & + F^{\delta}_{IJ}F^{\gamma,\dagger}_{JK}F^{\alpha}_{KL}F^{\beta,\dagger}_{LI}\big(R^{JK}_{\gamma\delta}E^{-1}_{KI}\Omega_{LK} + R^{JI}_{\gamma\delta}E^{-1}_{IK}\Omega_{LI} + Q^{JL}_{1,\gamma\delta}\Omega_{LI}\Omega_{LK}\big) \\ & + F^{\delta}_{IJ}F^{\alpha}_{JK}F^{\gamma,\dagger}_{KL}F^{\beta,\dagger}_{LI}\Omega_{KJ}\Omega_{LI}\big(R^{KL}_{\gamma\delta} - R^{JI}_{\gamma\delta} + Q^{JL}_{1,\gamma\delta} - Q^{KI}_{2,\gamma\delta}\big) \\ & + F^{\gamma,\dagger}_{IJ}F^{\alpha}_{JK}F^{\delta}_{KL}F^{\beta,\dagger}_{LI}\Omega_{KJ}\Omega_{LI}\big(R^{LK}_{\gamma\delta} - R^{IJ}_{\gamma\delta} + Q^{IK}_{1,\gamma\delta} - Q^{LJ}_{2,\gamma\delta}\big). \end{aligned} \tag{2.31}$$

Here, we have used capital Latin letters I, J, K, L to label the states that span the whole atomic Fock space, while F^{α} ($F^{\alpha,\dagger}$) shall be regarded as the matrix representation of the corresponding creation (annihilation) operators, respectively. Furthermore, we have used the shorthand notation $E_{ij} = E_I - E_J$ and $\Omega_{IJ} = (i\omega_n - E_{IJ})^{-1}$, while the R and Q functionals read:

$$R^{IJ}_{\gamma\delta} \equiv R_{\gamma\delta}(E_I, E_J) = \frac{1}{Z\beta}(e^{-\beta E_I} + e^{-\beta E_J})\sum_{\omega_n}\frac{\Delta_{\gamma\delta}(i\omega_n)}{i\omega_n - E_{IJ}}, \tag{2.32a}$$

$$Q^{IJ}_{\gamma\delta} \equiv Q_{\gamma\delta}(i\omega_n, E_I, E_J) = \frac{1}{Z\beta}(e^{-\beta E_I} - e^{-\beta E_J})\sum_{\omega'_n}\frac{\Delta_{\gamma\delta}(i\omega'_n)}{i\omega'_n - i\omega_n - E_{IJ}}, \tag{2.32b}$$

with $Q^{IJ}_{1,\gamma\delta} \equiv Q_{\gamma\delta}(i\omega_n, E_I, E_J)$ and $Q^{IJ}_{2,\gamma\delta} \equiv Q_{\gamma\delta}(-i\omega_n, E_I, E_J)$. Careful treatment of the possible singularities – that can arise from degenerate subspaces – must be considered. In such cases, the Q integral takes the form:

$$Q_{\gamma\delta}(i\omega_n, E_I, E_J) \xrightarrow{E_I = E_J} -\frac{\beta}{Z}e^{-\beta E_J}\Delta_{\gamma\delta}(i\omega_n). \tag{2.33}$$

Lastly, the corresponding singularities of the first 4 lines of Eq. (2.29) can be lifted by applying the de L' Hospital rule simultaneously on both R integrals. This leads to the

following expressions:

$$R^{JK}_{\gamma\delta}E^{-1}_{JL}\Omega_{JI} + R^{LK}_{\gamma\delta}E^{-1}_{LJ}\Omega_{LI} \xrightarrow{E_{JL}\to 0} \frac{\partial R^{JK}_{\gamma\delta}}{\partial E_J}\Omega_{JI} + R^{JK}_{\gamma\delta}\Omega^2_{JI} \tag{2.34a}$$

$$R^{KJ}_{\gamma\delta}E^{-1}_{JL}\Omega_{JI} + R^{KL}_{\gamma\delta}E^{-1}_{LJ}\Omega_{LI} \xrightarrow{E_{JL}\to 0} \frac{\partial R^{KJ}_{\gamma\delta}}{\partial E_J}\Omega_{JI} + R^{KJ}_{\gamma\delta}\Omega^2_{JI} \tag{2.34b}$$

$$R^{KJ}_{\gamma\delta}E^{-1}_{KI}\Omega_{LK} + R^{IJ}_{\gamma\delta}E^{-1}_{IK}\Omega_{LI} \xrightarrow{E_{IK}\to 0} \frac{\partial R^{KJ}_{\gamma\delta}}{\partial E_K}\Omega_{LK} - R^{KJ}_{\gamma\delta}\Omega^2_{LK} \tag{2.34c}$$

$$R^{JK}_{\gamma\delta}E^{-1}_{KI}\Omega_{LK} + R^{JI}_{\gamma\delta}E^{-1}_{IK}\Omega_{LI} \xrightarrow{E_{IK}\to 0} \frac{\partial R^{JK}_{\gamma\delta}}{\partial E_K}\Omega_{LK} - R^{JK}_{\gamma\delta}\Omega^2_{LK} \tag{2.34d}$$

These equations form a closed set and allow us to evaluate Eq.(2.31), given the atomic Hamiltonian and the hybridization function $\Delta(i\omega_n)$. Consequently we can exactly obtain the self-energy of the impurity model up to second order with respect to the hybridization by Eq. (2.28). This completes the mathematical formulation of the strong-coupling approximation impurity solver, which can be used as any other impurity solver within the DMFT self-consistency cycle – see Fig. 1.7.

2.2.2 Implementation details

In this section, we will discuss the crucial technical details that need to be considered when implementing the strong-coupling approximation impurity solver (SCA). The computational cost associated with the SCA stems from:

1. The full diagonalization of the atomic Hamiltonian.
2. The evaluation of the two-particle amputated Green's function, namely Eq. (2.31).

Here, we focus only on the second source of computational cost, since the diagonalization step does not nowadays pose a relevant restriction, at least for most systems of interest. Furthermore, based on physical grounds we will show that the full solution of the atomic problem is not even necessary.

Regarding the computational cost, **C**, associated with Eq. (2.31), a mere inspection results in a scaling relation $\mathbf{C} = N^4_{\text{orb}} \times N^4_F \times N^2_\omega$. Here, N_{orb} is the number of single-particle states,

$N_F^4 \times N_\omega^2$ is the dimension of the atomic Fock space and N_ω is the dimension of the Matsubara axis in which the Green's functions are defined. For instance, considering a full $d-shell$ to represent the atomic problem, a naive (brute-force) implementation would necessitate the evaluation of up to 10^{16} integrals; an impractical scenario even for a modern computer.

Since all terms of Eq. (2.31) have the same structure – element-and-index-resolved matrix-multiplications of two annihilation and two creation operators followed by numerical R and Q integrations – we consider, without loss of generality, only the first one. In a more compact notation, it reads:

$$\text{Eq.(2.31)} \xrightarrow{\text{1st term}} \sum_{IJKL} F_{IJ}^{\alpha} F_{JK}^{\gamma,\dagger} F_{KL}^{\delta} F_{LI}^{\beta,\dagger} P_{IJKL}(i\omega_n), \tag{2.35}$$

where $P_{IJKL}(i\omega_n)$ stands for all terms inside the parenthesis of the original expression. The functional form of the R and Q integrals provide an immediate simplification: the Bolzmann prefactors make the combinations that involve only high-in-energy states numerically irrelevant and thus effectively truncate the Fock-space of the problem [2].

Assuming that the relevant many-body states belong to a subset of the Fock space $\mathscr{S}$, we can furthermore seek for an efficient representation of the corresponding fermionic operators. Indeed, most elements of the matrices F are by definition zero, while conserved quantities – represented by good quantum numbers – usually prohibit a large set of contractions. The numerical search of those quantum numbers, that maximally partition the (remaining) Fock space, can be obtained by the so-called autopartition method without prior or additional knowledge, apart from the many-body Hamiltonian itself [116].

Summarizing the algorithm, during its first phase the local Fock space is partitioned into the finest direct sum of subspaces of smaller dimension. This corresponds to finding a permutation of the basis vectors so that the local Hamiltonian is block-diagonal. In the second step, the resulting partition is further modified so that all creation and annihilation operators are matrices with maximally one non-zero element in each row and column.

[2] In fact, at the intermediate temperature regime, the only relevant I, J, K, L combinations are those where at least one index points to the ground-state Hilbert space.

Within the discussion above, Eq. (2.35) can be rewritten as,

$$\text{Eq. (2.35)} \xrightarrow{autopartition} \sum_{s_1,s_2,s_3,s_4} \sum_{ijkl} F^{\alpha}_{ij} F^{\gamma,\dagger}_{jk} F^{\delta}_{kl} F^{\beta,\dagger}_{li} P_{ijkl}(i\omega_n), \tag{2.36}$$

where s_i are the obtained subspaces and i, j, k, l are indices running over them. Thus, instead of scanning over (large) square matrix representations, we traverse over all combinations of (small) rectangle ones defined for all possible s_i subspaces, which is orders of magnitute more efficient.

do not reduce the computational cost dramatically. The remaining computational cost is attributed to the evaluation of the R and Q integrals themselves [3]. The key observation here is that both types of integrals depend on the energy difference in their denominator. This allows for an efficient use of look-up tables to store the integrals in memory and access them when required, instead of re-evaluating them each time. Especially for large multi-orbital systems this insight exploits the fact that multiple degeneracies usually occur, thus leading to a large reduction of the required integrations to be performed. Furthermore, we have implemented a combination of numerical and analytical integration – based on second order moment-expansion model – which can be used to even further reduce the computational cost. This is crucial considering the fact that calculations at low temperatures usually necessitate the enlargement of the Matsubara axis – of the order of 10^3 frequencies.

2.2.3 Benchmarks: The single-band Hubbard model

Before closing this section, we will test the applicability and accuracy of the SCA impurity solver when employed within the DMFT framework. We will compare the results against the – numerically exact – continuous time Quantum Monte Carlo (CT-QMC) impurity solver in its hybridization expansion variant [116] and the exact-diagonalization (ED) one. To simplify our analysis and avoid systematic errors of CTQMC– such as the fermionic sign problem – while being able to provide accurate results even with finite (small) number of

[3] The symmetries of the $G^{\text{amp}}_{\alpha\beta}(i\omega_n)$ can also be used although they do not reduce the computational cost dramatically.

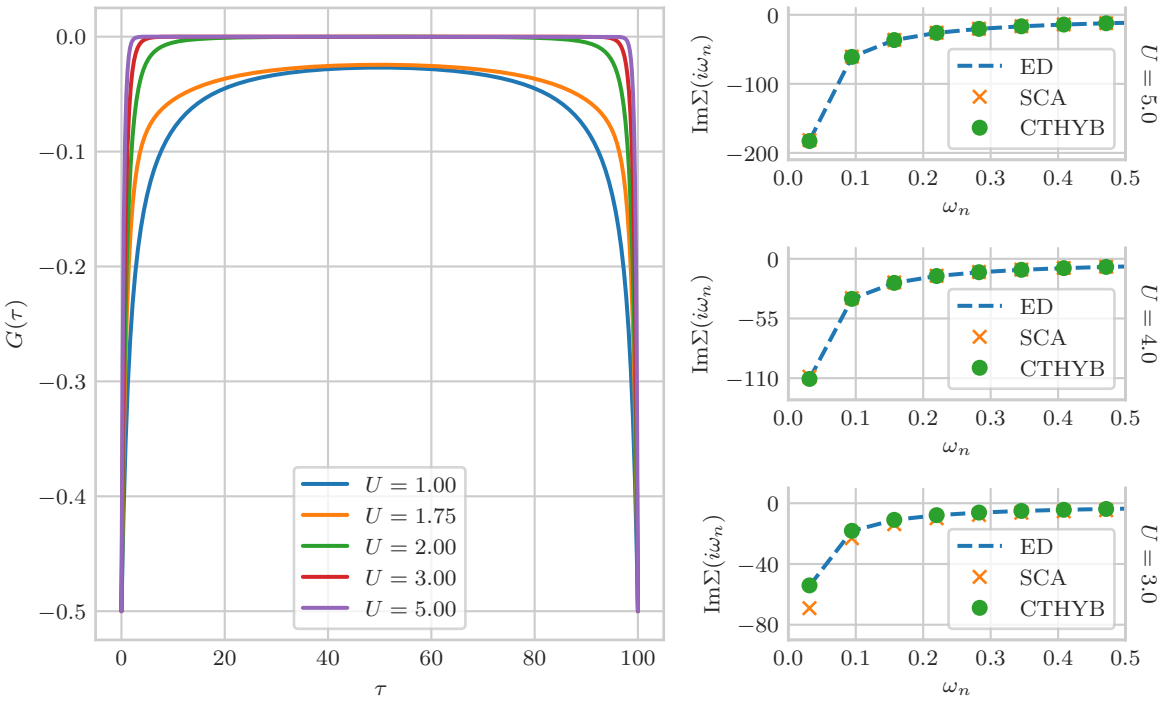

Fig. 2.4: (left) The interacting one-particle Green's function, $G(\tau)$, as obtained by CT-QMC within the DMFT framework for increasing on-site Hubbard interaction strength U. (right) Comparison between ED, CT-QMC and SCA impurity solvers for selected insulating cases on the level of the self-energies.

bath sites used in ED, we consider the single-band Hubbard model at half-filling with a dispersion relation that reads,

$$\varepsilon(\mathbf{k}) = 2t\ (\cos k_x + \cos k_y + \cos k_z). \tag{2.37}$$

Here, we set the hopping $t = \frac{1}{6}$ so that the half-bandwidth $D = 1$ is used to set our units. All simulations have been performed at fixed temperature $T = 0.01$ and are restricted to the paramagnetic phase, namely we impose the symmetry $\Sigma^{\uparrow\uparrow}(i\omega_n) = \Sigma^{\downarrow\downarrow}(i\omega_n)$.

For increasing strength of the on-site Coulomb interaction U, the system undergoes a metal-to-insulator transition at $U_c \approx 2.0$. This is shown on the left-hand side of Fig. 2.4, where we plot the converged $G(\tau)$ both in the metallic and in the insulating regime, obtained by simulations using the CT-QMC impurity solver. On the right-hand side of Fig. 2.4 we compare the different impurity solvers on the level of the self-energy $\Sigma(i\omega_n)$ for selected

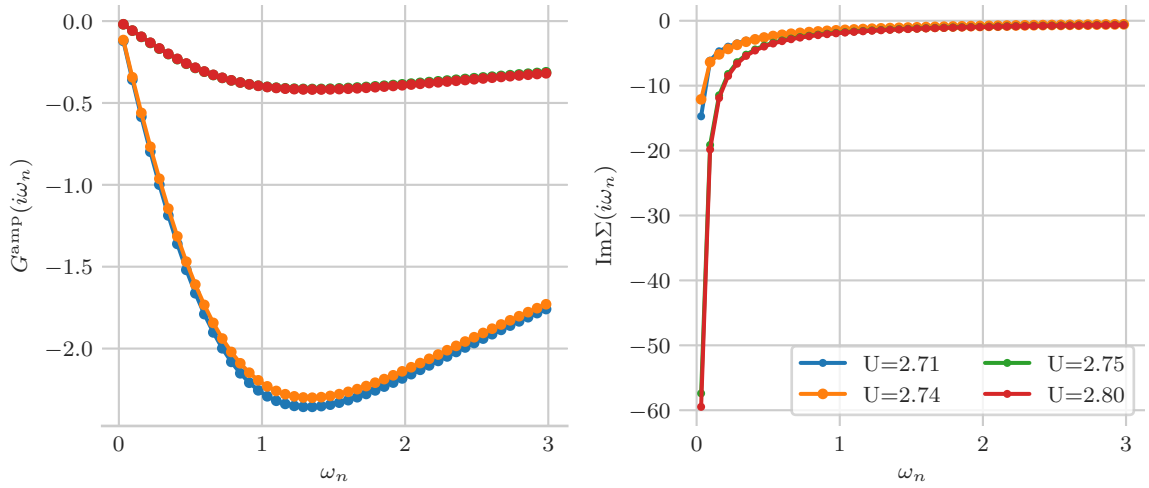

Fig. 2.5: The two-particle amputated Green's function (left) and the corresponding imaginary part of the self-energy (right) at selected interaction values around the *breakdown* in the last (obtained) iteration. For $U < 2.75$ the self-consistency cycle breaks down and non-causal features in the self-energy appear in the next DMFT iteration. For larger interaction values although the deviations from the numerically exact results are substantial, the DMFT self-consistent cycle can be completed. The abrupt changes between the (non-converging) $U = 2.74$ and (converging) $U = 2.75$ numerically pinpoint the SCA breakdown point.

insulating (only) cases [4]. For large U values, where the system is governed by the atomic-reference point, all solvers show excellent agreement. Naturally, substantial numerical deviations start to appear as we lower U and approach the insulator-to-metal transition. Hence. the further we move away from the SCA reference point (atomic-limit) the more crude the truncation of the perturbation series becomes. As a side remark, note that the differences are confined only to the low-frequency regime, as the high-frequency part $\omega_n > U$ is in any case an atomic-like feature.

The truncation scheme employed in the SCA eventually breaks down – already before the transition – and is signaled by artifacts that manifest themselves in non-causal (negative) spectral functions [5]. Non-causal spectral functions result from the violation of the Green's function's analytic properties and consequently of the self-energy. Directly from Eq. (2.28)

[4] The discrepancies in level of the $G(\tau)$ are not descriptive enough.

[5] This sets the hard limit of the applicability of the SCA impurity solver for any (multiorbital) system.

and since the atomic-limit self-energy fulfills by construction all analytic properties, we can deduce that the issue arises from the mismatch between the hybridization function and the two-particle amputated Green's function [77]. In Fig. 2.5, we explicitly target the parameter-space region where the breakdown of the approximation occurs. Note the abrupt changes on the functional form of the two-particle amputated Green's function upon lowering the on-site interaction. The still causal self-energies for $U < 2.75$ are misleading: in the next iteration non-causal features burst forth and the convergence procedure must be terminated.

Further restrictions can be enforced in order to postpone the non-causality issue and perform calculations for lower U values. However, the very perturbative nature of the SCA impurity solver comes in conceptual disagreement with the corresponding parameter regime. A more powerful and promising approach has been recently proposed within the so-called *superperturbation theory* [50] in which the expansion is not limited around the atomic-limit but instead around *any* solvable reference system.

2.2.4 Final remarks

The SCA impurity solver offers an efficient approach to solve a quantum impurity problem, which in turn is a key component in the DMFT framework. As is the case of any perturbative expansion, its applicability is confined to the phase-space around the corresponding reference system. In principle, there are only two conditions to satisfy in order to make use of the SCA: **(i)** integer total filling of the impurity system and **(ii)** proximity to the atomic-limit.

The small-to-moderate accompanying computational cost – resulting from an efficient implementation – allows to solve large and complicated multiorbital Hamiltonians, without further assumptions or simplifications on its quadratic or quartic part. Due to the latter, and considering also the numerical and computational limitations of more powerful impurity solvers, the SCA offers an alternative approach that can be used:

- In the framework of DFT+DMFT and especially within the full charge self-consistency scheme. Here the calculations are usually resource- and time- consuming and the SCA can be also employed to provide either the full solution or at least *a better starting point* for more powerful methods.

- In generic model studies to scan over multi-dimensional parameters' space and to analyze trends of the system. Importantly, access to uniform and static response functions – that typically require high-level of accuracy on the one-particle interacting propagators – is possible with a rather moderate additional computational cost that originates from further breaking of symmetries on the Hamiltonian level.

- For (cluster) calculations even directly on the real frequency axis, as the R and Q functional integrals in Eq. (2.31) can be analytically continued [63].

Chapter 3

Investigation of the $LaNiO_2/LaGaO_3$ heterostructure

Since after its discovery in cuprates [17], high-temperature superconductivity (HTS) has been one of the most fascinating macroscopically observed phenomena in condensed matter physics. Being a hallmark of strongly correlated systems, cuprates have been the subject of extensive theoretical and experimental studies [109, 66] driven both by the partial – or non-conclusive – undestanding of the underlying mechanism and (of course) the technological consenquences that a near-the-room-temperature superconductor might trigger [114]. This has lead to the discovery of other – similar but not quite to cuprates – families of HTS compounds, such as ruthenates [89, 86], cobaltates [130] and pnictides [118, 140], that form each by themselves a very active research field.

Inspired by their proximity – in terms of the periodic table classification – to cuprates, nickel-based oxides (nickelates) have been theoretically proposed [8, 107, 52, 51] as possible candidates for HTS cuprates' analogs, despite their differences [81]. However, theoretical expectations and predictions did not meet experimental realization; at least not until very recently, when superconductivity has been observed and reported by D. Li *et al.* in $Nd_{0.8}Sr_{0.2}NiO_3$ infinite layer [82]. Nickelates are actively back in the forefront of investigations, afresh.

Here, we report our realistic calculations on the layered $LaNiO_2/LaGaO_3$ superstructure, resolving the layer and orbital spectral weight structure at nominal filling and most importantly upon hole and electon doping. The chapter is organized as follows. In Section 3.1, we provide details on the model and the methodology that has been employed. In Section 3.2 and 3.3, we comment on the general features of the aggregated spectral functions and explicitly discuss the layer-dependence and structure of the relevant orbitals, respectively. In the last section, we summarize our findings.

3.1 Model and methodology

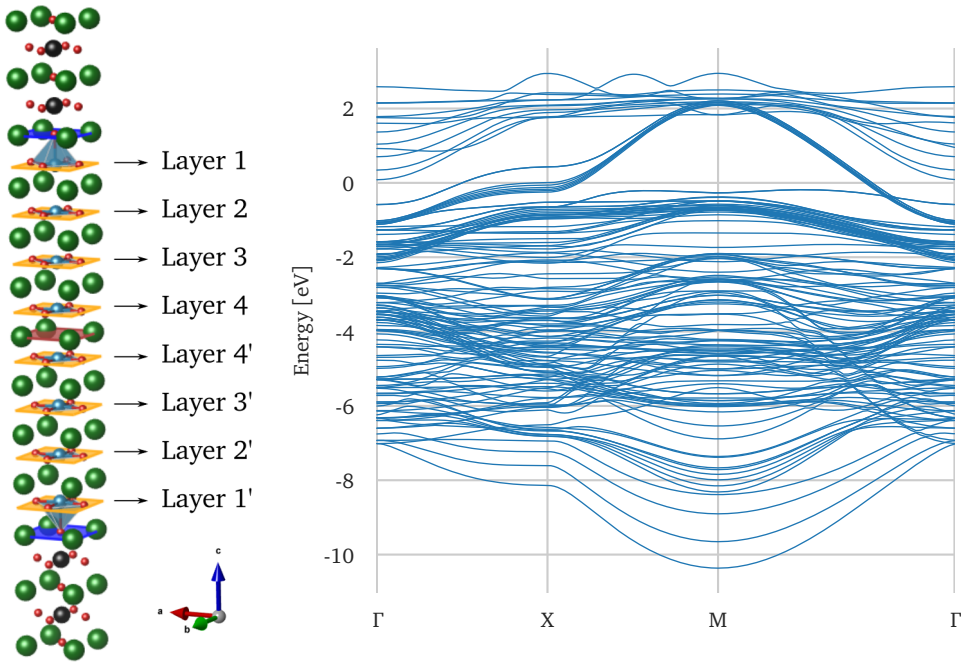

Fig. 3.1: (left) The unit cell of $LaNiO_2$. (right) The bandstructure along the high-symmetry points of the Brillouin zone. The Fermi energy is adjusted to $E_F = 0\ eV$.

Our calculations have been performed within the framework of density functional theory (DFT) and single-site dynamical mean-field theory (DMFT), without full charge self-consistency, as discussed in detail in Section 1.5. The DFT calculations have been carried

out using the VASP code [75], and we have obtained the *realistic* tight-binding representation of the system (wannierization) in the low energy regime $[-12\ eV, 3\ eV]$ using the Wannier90 code [99]. In Fig. 3.1, we show the structure of the heterostructure together with the resulting bandstructure along the high-symmetry points of the Brillouin zone. Note that the zero level has been adjusted to the chemical potential of the system at nominal filling ($N = 122$ electrons per spin-block).

The derived model consists of 139 orbitals (per spin-block) and includes the Nickel $3d$-, the Oxygen $2p$- and the Lanthanum $5d$- and $4f$-states. All Nickel atoms – full d-shell – are considered and treated as correlated, while oxygens and lanthunum states as uncorrelated. In all eight Nickel subspaces, we have introduced the Coulomb interaction, which is approximated by the rotationally invariant Kanamori operator [R] and parametrized with the on-site Hubbard $U = 8\ eV$ and Hund's coupling $J_H = 0.8\ eV$.

As mentioned above, correlation effects have been taken into account for each Nickel within DMFT. Exploiting the mirroring symmetry of the layers (or equivalently of the Nickel subspaces), on each iteration of the full self-consistent DMFT cycle, see Fig. 1.7, we solve simultaneously and independently only four impurity models: one for each correlated subspace in layers L^1, L^2, L^3, L^4. Regarding the very solution of the DMFT auxiliary impurity models, we have employed the state-of-the-art continuous-time quantum Monte-Carlo solver (CT-QMC) [135], in its hybridization expansion variant (CT-HYB) [116]. In all studied cases, and after the DMFT self-consistency condition has been satisfied, we have further obtained 50 independent measurements of high QMC statistics ($\sim 10^8 - 10^9$ QMC cycles) of the (four) resulting impurity models, in order to average out the unavoidable QMC noise and increase the quality of our results on the imaginary (Matsubara) axis. The latter is a key requirement to optimally perform the necessary step of the analytical continuation, for which we have used the maximum entropy method (MEM) [76, 74].

All calculations have been performed at fixed temperature $T = 116\ K$ enforcing the self-energy to be paramagnetic on each correlated subspace, namely $\Sigma_{\uparrow\uparrow} = \Sigma_{\downarrow\downarrow}$. Electron and hole doping has been considered by adjustment of the chemical-potential. Lastly, and since the derived Hamiltonian consists of both correlated and uncorrelated states, the double

counting (DC) correction terms – layer dependent – have been approximated by the *around-mean-field* [10].

3.2 Results: Aggregated local spectral functions

The starting point of our analysis is Fig. 3.2, where we show the aggregated local spectral functions , $A(\omega)$, resolved and grouped in terms of the atomic character of the states, over an extended energy window for all studied cases of total particle-filling: nominal filling and additional two and three holes/electrons. At nominal filling, we find most of the oxygen spectral weight to be located around $-4.85\ eV$ extended over a wide energy window. Lanthanum states, located around $1.8\ eV$, are less dispersive than the oxygen ones, although completely empty. For Nickel states, the largest portion of the spectral weight is distributed over a large energy window, while clearly a (small) quasiparticle peak structure is observed on the Fermi level.

Inducing holes into the system, results in significant modifications of the overall spectral weight structure. Lanthanum and oxygen states are push away and towards the Fermi level, respectively. In particular, the center of mass of the oxygen's spectral weight shifts by approximately $1\ eV$, and develops a peak in the proximity of the Fermi surface. Strong redistribution of the spectral weight is observed for the Nickel states, which concentrates at very low energies and develops distinct peaks that correspond to the t_{2g} and e_g subspaces. On the opposite doping direction (electron doping), we find very different behavior. The oxygen spectra remain rather unaffected in terms of their structure and only slightly shift to lower energies. On the contrary, lanthanum states gradually cross the Fermi level and start to contribute to the formation of the quasiparticle peak, albeit the latter is definitely dominated by the nickel $3d$-states.

In Fig. 3.3, we summarize quantitatively the effect of doping on the occupation of the Nickel, Oxygen and Lanthanum states, by showing the absolute (histograms) and relative (pie-charts) distribution of the charge carriers in the system. We note that the data have been extracted directly from the converged local Green's functions on the Matsubara axis.

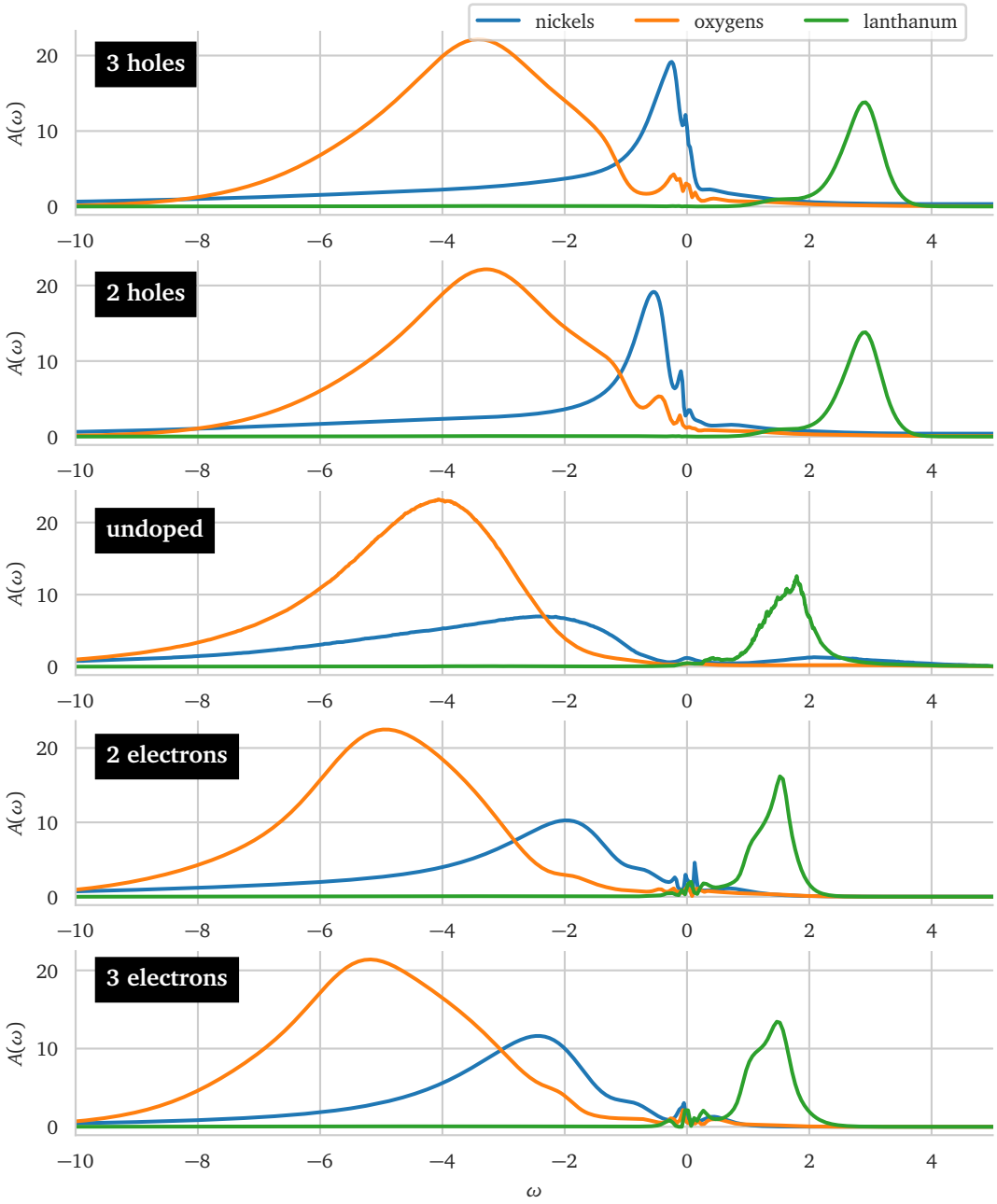

Fig. 3.2: Local spectral functions at nominal filling and for hole and electron doping, aggregated and resolved in terms of the atomic character.

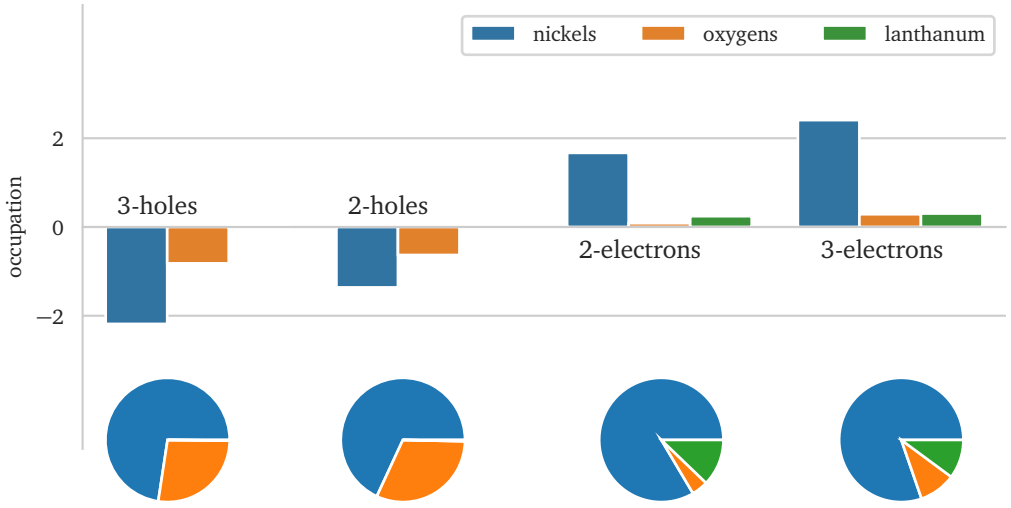

Fig. 3.3: The distribution of the induced charge carriers (holes or electrons) within the nickel, oxygen and lanthanum states. The pie-charts show the relative percentage of the particle distribution within the corresponding states normalized with respect to the overall doping.

Regardless the type of doping, we find the largest portion of the charge carriers to be distributed among the nickel subspaces. In the hole-doping cases, more than 25% of holes lie at the oxygen states. In the electron-doping cases, both lanthanum and oxygen doping is not negligible $\sim 10\%$, although it is expected that the oxygen states to be exhausted for stronger doping.

3.3 Results: Layer and orbital resolved spectra

Having discussed the overall behavior of the system at nominal filling and upon hole and electron doping, we turn our attention to the layer- and orbital-resolved spectral functions of each case, shown in Fig. 3.5-3.9. There, for each layer $L^1 - L^4$ – the rest are symmetric as discussed earlier – we explicitly visualize all five orbitals of the corresponding Nickel atom together with its nearest neighboring oxygen ligands (for L^1 the additional apical oxygen has been included), on the energy window $[-5\ eV, +5\ eV]$.

Already at nominal filling, the orbital distributions (location and structure) show very distinct layer dependent features. For all layers, the in-plane oxygens are located at approximately same energies, while the apical-oxygen states in layer L^1 are found at $-3eV$. As expected, the more relevant states are the Nickel ones. Although, in all layers we find the $d_{x^2-y^2}$ dominating the spectral weight at the Fermi level, the distribution of t_{2g} subspace – d_{xy}, d_{xz}, d_{yz} orbitals – as well as d_{z^2} orbital clearly depends on the corresponding layer: for the layer L^1 they are located in between the apical oxygen states and the Fermi level at -1 eV, while in the rest layers they are found in the proximity of the in-plane oxygen states and are rather decoupled from the $d_{x^2-y^2}$ orbital.

When we consider two holes in the system, the spectral weight shifts towards to Fermi level. The t_{2g} orbitals are greatly affected in all layers, reaching (L^1, L^2, L^3) or even crossing (L^2) the Fermi energy. The behavior of the d_{z^2} orbital is distinct when comparing the L^1 with the rest layers: in the former we find an almost half filled (insulating) state, while in the latter the d_{z^2} orbital is completely occupied. The d_{x2-y2} orbitals show similar features for all layers: close to half-filling and with clear quasiparticle peak at the Fermi energy. In the case of three holes in the system, we observe very similar features and trends for all orbitals, although the t_{2g} subspace and in particular the d_{xz} and d_{yz} orbitals are now clearly crossing the Fermi level in layers L^1 and L^2.

The situation in the electron doping regime is very different. The oxygen states, the t_{2g} subspace and the d_{z^2} orbital remain rather unaffected with respect to the nominal filling for all layers and for both studied dopings. The $d_{x^2-y^2}$ orbitals show layer dependent features mainly on their spectral weight formation for the two-electron doping, which may be due to their interplay with the lanthanum states (not shown here). For the three-electron doping case, the $d_{x^2-y^2}$ partial spectral function has similar structure in all layers.

Finally, in Fig. 3.4 we summarize quantitatively the effect of doping on the orbital occupations for each layer, as obtained by a direct comparison against the nominal filling results. Note that the data have been obtain directly from the local Green's function on the imaginary axis. Evidently, the inner most layers L^3 and L^4 show very similar behavior regardless the direction of the doping (hole or electron): in both cases we effectively induce the charge

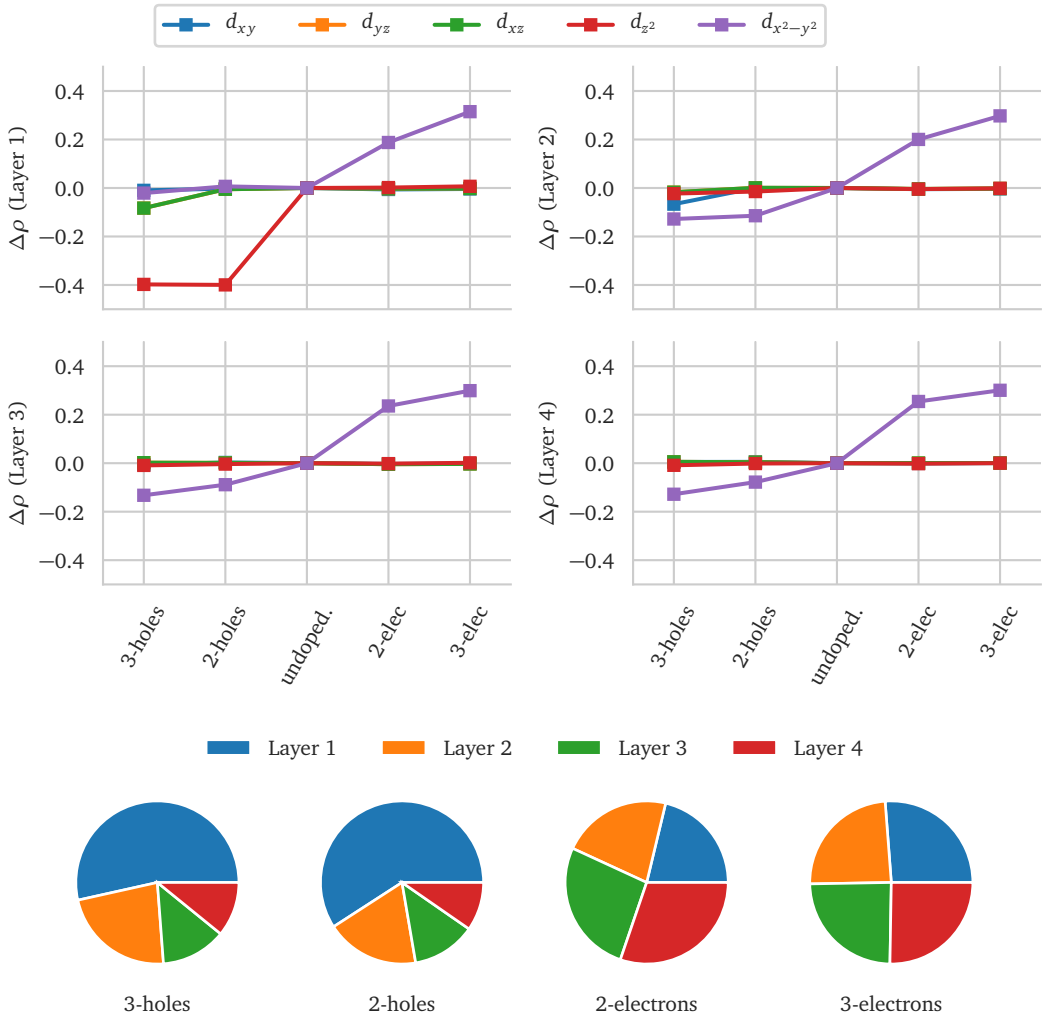

Fig. 3.4: Distribution of the charge carriers (holes or electrons) on the Nickel d-orbitals resolved in terms of the corresponding layer. (pie-charts) Concentration of the charge carriers (total sum) with respect to the corresponding layer of the heterostructure.

carriers solely to the $d_{z^2-y^2}$ orbitals. This trend gradually changes when moving to layer L^2. Here, although the doping affects dominantly the $d_{x^2-y^2}$ orbital, we find a non-negligible hole doping of the d_{yz} and d_{xz} orbitals. The most distinct effects, though, are observed in the outermost (interface) layer L^1 possibly due to the influence of the apical oxygen; here, we find a clear tendency towards the concentration of the holes (electrons) to the d_{z^2} ($d_{x^2-y^2}$) orbital. Lastly, based on the pie-charts, we observe that in the hole doping regime

the charge carriers are primarily confined within the layers L^1 and L^2, different than the electron doping regime where no significant layer-preference is found.

3.4 Summary

In summary, we have performed *ab initio* calculations for the $LaNiO_2/LaGaO_3$ heterostructure within the merger of DFT and DMFT, focusing on the one-particle local spectral functions of the system at nominal filling and for hole and electron doping. We have found substantial differences with respect to the doping direction and characteristic layer and orbital dependence.

A clear trend towards doping the Nickel orbitals is found in all cases, while oxygens (in the hole-regime) and lanthanum (in the electron-doping regime) states contribute to the overall spectral weight on the Fermi level. Our analysis over the layer- and orbital-resolved spectra suggests a single-band-like $d_{x^2-y^2}$ doping-scenario for the inner most layers of the heterostructure where both the t_{2g} and the axial d_{z^2} orbitals are completely occupied.

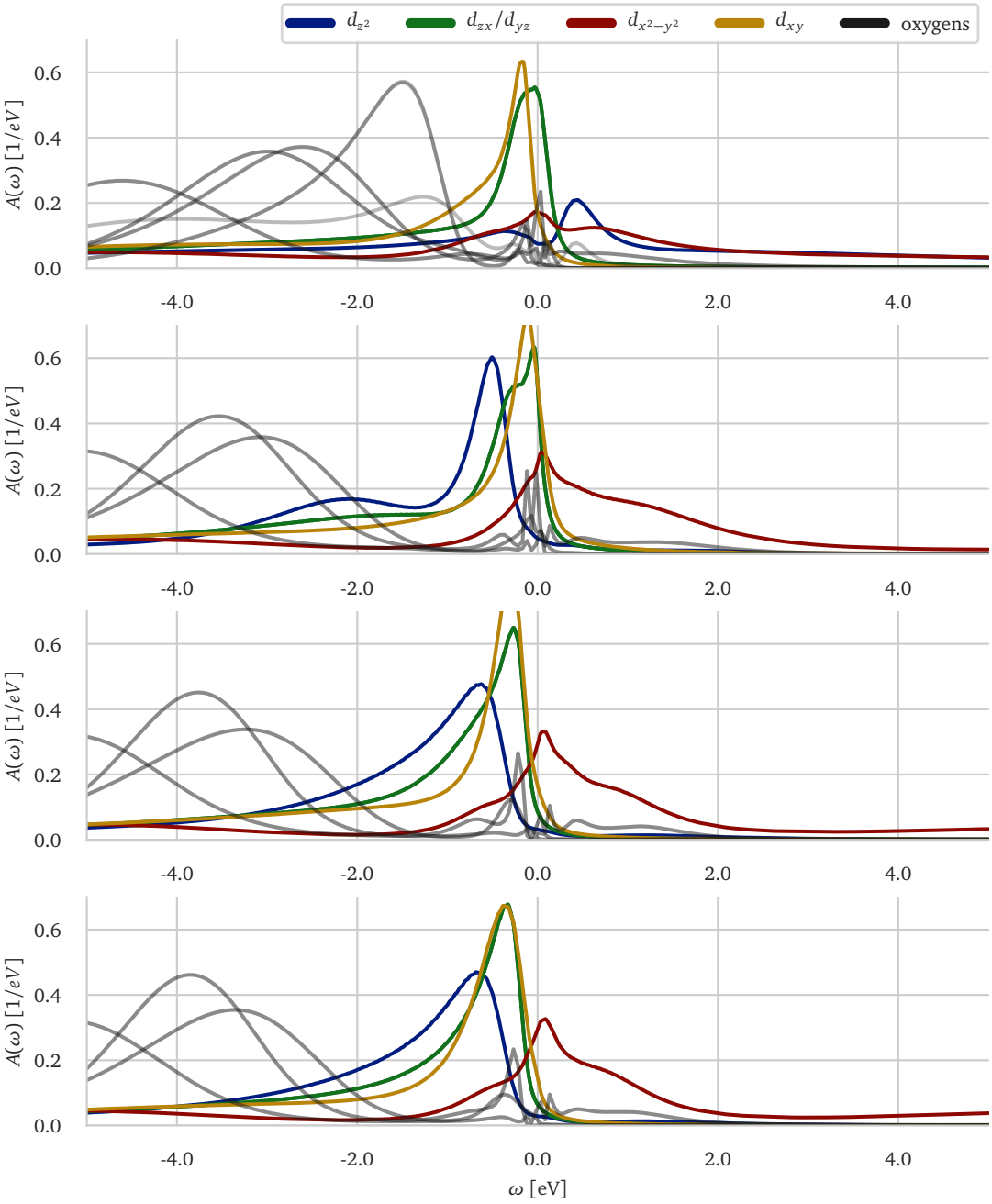

Fig. 3.5: Layer- and orbital-resolved local spectral functions for the three-holes doping case.

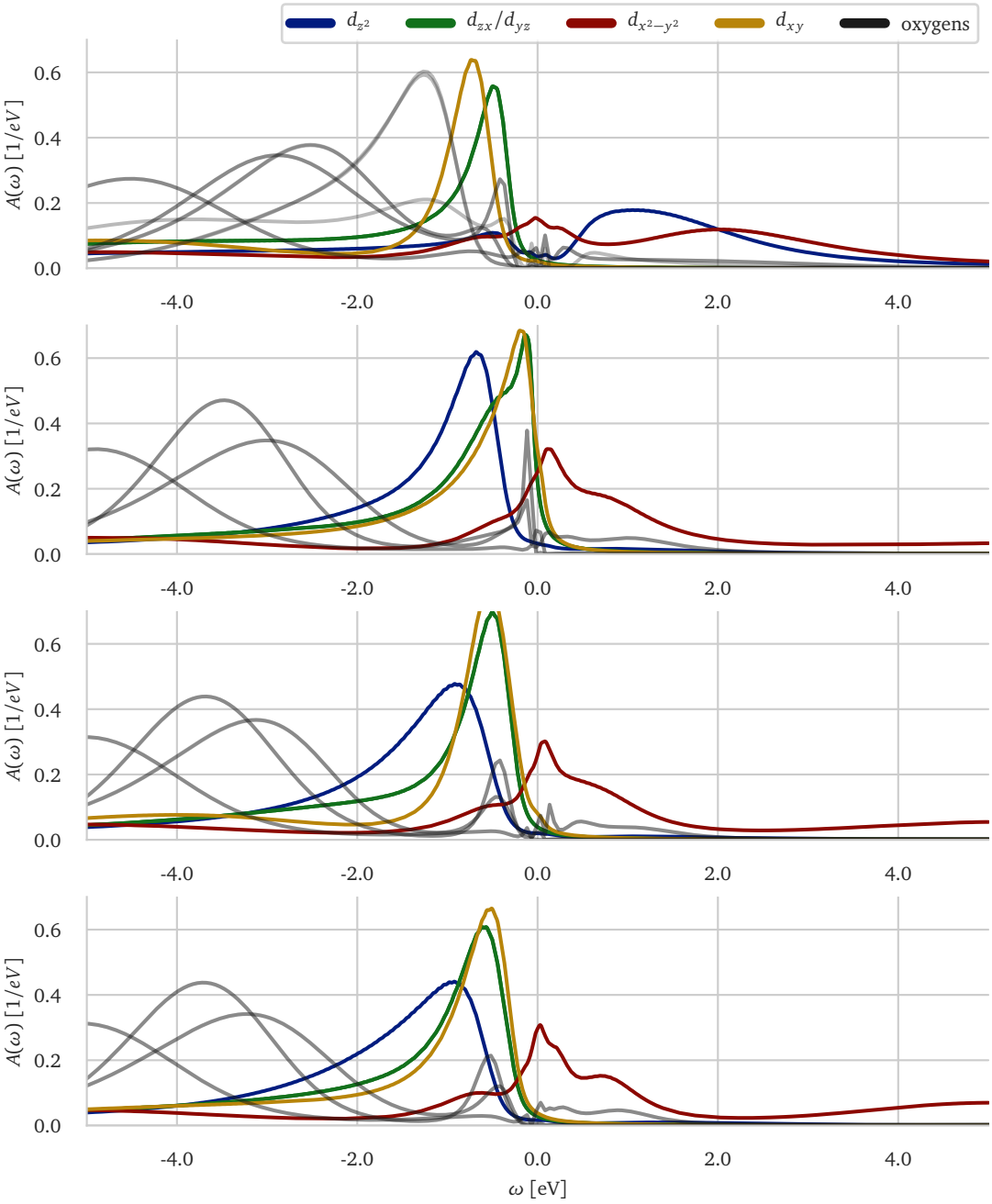

Fig. 3.6: Layer- and orbital-resolved local spectral functions for the two-holes doping case.

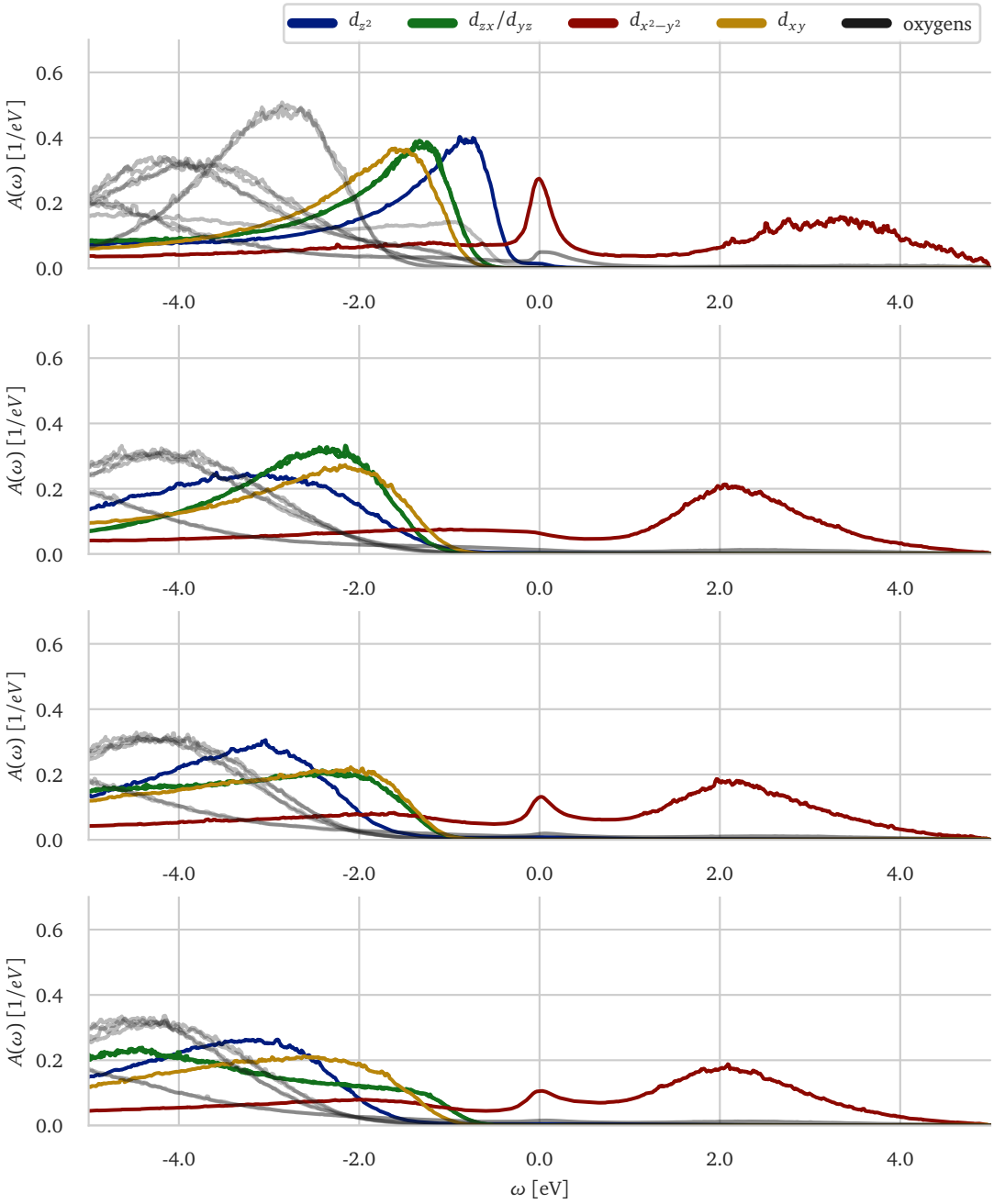

Fig. 3.7: Layer- and orbital-resolved local spectral functions for undoped case.

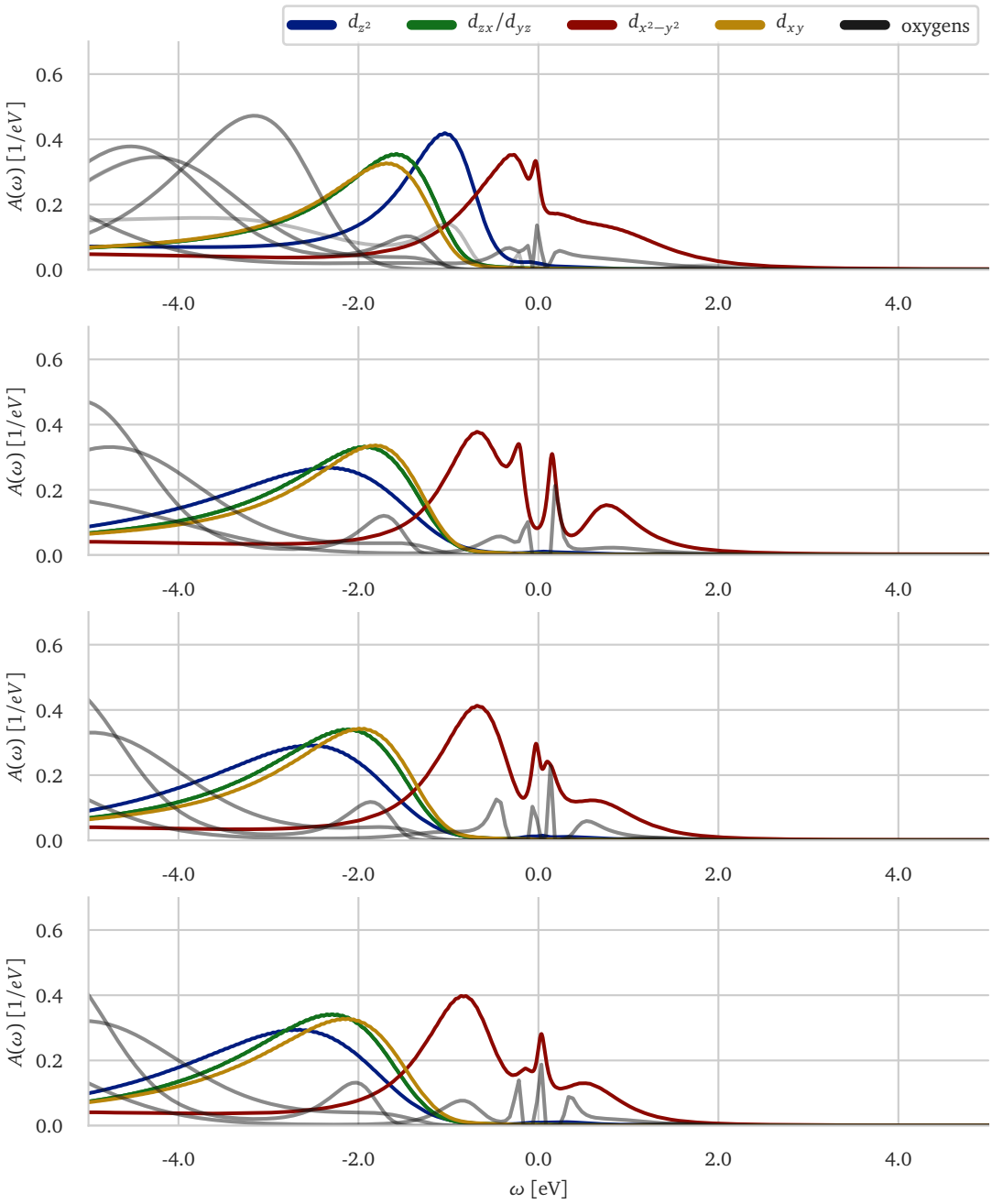

Fig. 3.8: Layer- and orbital-resolved local spectral functions for the two-electron doping case.

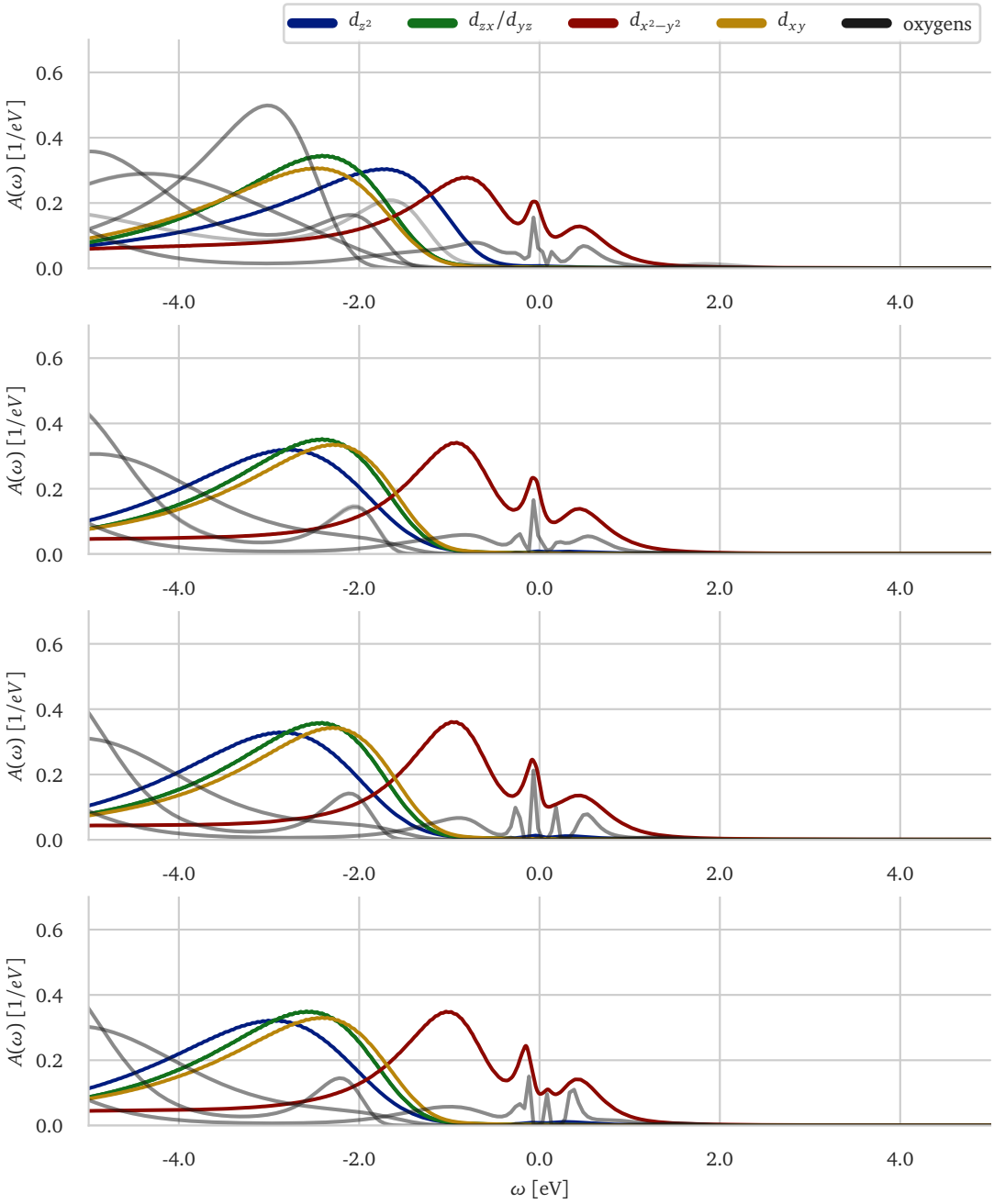

Fig. 3.9: Layer- and orbital-resolved local spectral functions for the three-electron doping case.

Chapter 4

On the interplay of crystal-field and spin-orbit coupling effects

Transition metal compounds of the $4d$ or $5d$ series, for instance Ruthenates or Iridates, are currently in the forefront of intense experimental and theoretical investigation [143, 18, 110]. From a theoretical point of view, their study through (derived) effective low-energy is challenged by significant difficulties that mainly originate from the interplay and competition of energy scales.

When present, a clear hierarchy of those energy scales is of great use; not only it directly connects with the existence of good quantum numbers – thus an optimal single particle basis to formally express the Hamiltonian itself – but also allows for further approximation schemes to be considered. For instance, transition metal compounds of the $3d$-series are usually characterized by dominant crystal-field potential and one usually labels the single particle states according to the irreducible representations of the underlying lattice symmetry. Complementary, in rare-earth ($4f$-series) compounds spin-orbit coupling dominates over the crystal-field energy-scales and thus renders the total angular momentum – the eigenbasis of spin-orbit coupling – to be the single-particle basis of choice.

In between, and especially for the $4d$-series compounds, such a clear hierarchy breaks down

and both crystal-field and spin-orbit coupling effects have to be considered explicitly: a task that only recently became feasible – yet significantly challenging – due to advancements of computational methodologies that allow to work within the absence of non-conserving and generic (even realistic) models.

Both parts of this chapter, focus on the interplay and effect of both crystal-field and spin-orbit coupling on the physical properties of strongly correlated systems. In the first part of this chapter, we present our results for Ca_2RuO_4 obtained by the merger of DFT+DMFT, where we focus on the single particle spectral functions when a DC-current is applied. To a large extend our discussion follows Ref. [19] and at its Supplementary Material, although we restrict ourselves mostly on the theoretical and methodological part of the work. In the second part, we present a generic study of a t_{2g} model in order to shed more light on the distinct effects of the crystal-field and/or spin-orbit coupling both on a single- and two-particle level.

4.1 Current driven insulator-to-metal transition in Ca_2RuO_4

*Parts of this section are published in "**A Unique Crystal Structure of Ca_2RuO_4 in the Current Stabilized Semi-Metallic State**" [19].*

Non-equilibrium phenomena in correlated fermionic systems currently form a major frontier of condensed matter research, since they provide an alternative way to realize phase transitions and study the interplay of competing energy scales [93, 138, 34]. Recent experiments on the antiferromagnetic Mott insulator Ca_2RuO_4 unveiled a rare example of a phase transition when a DC voltage is applied [101, 121]: upon applying an external voltage the insulating ground state was observed to transform into an electrically conducting phase with the latter being characterized by strong diamagnetic susceptibility.

Although it has been shown that in semi-metals such large diamagnetism can arise from light-mass Dirac electrons in the presence of strong spin-orbit coupling [39, 40], the electronic structure of ruthenates' metallic phases, such as Sr_2RuO_4, is incompatible with such

view [90, 26]. There, the Fermi surfaces consist of large multiple sheets and four electrons are distributed rather evenly within the t_{2g} subspace, while the metal-to-insulator transition can be tuned upon chemical substitution and involves a redistribution of the electrons accompanied with a first order structural transition; the latter involves the compression, tilt and rotation of the RuO_6 octahedra [103, 33].

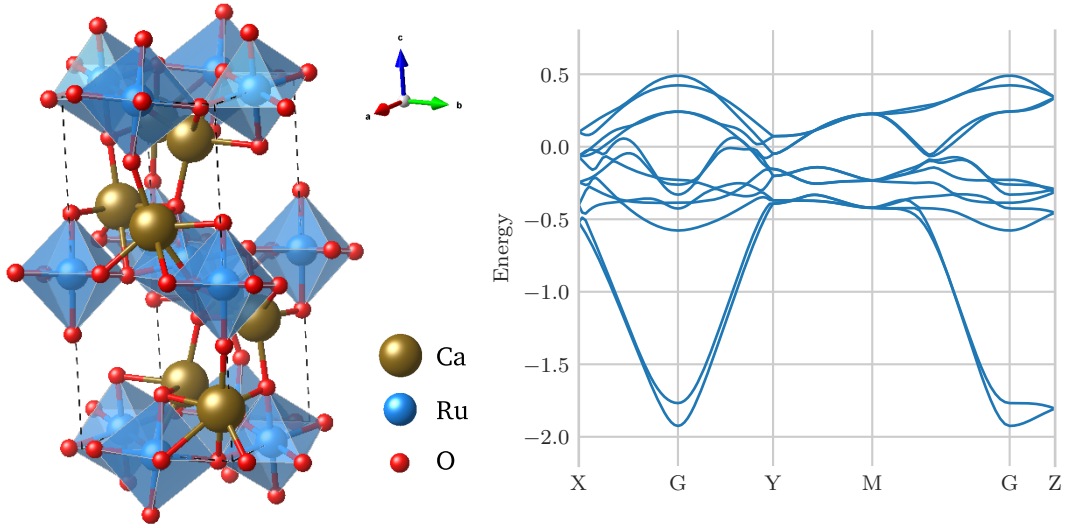

Fig. 4.1: (left) The conventional unit cell of Ca_2RuO_4. (right) The bandstructure along the high-symmetry points of the Brillouin-zone. The Fermi energy corresponds to $E = 0\ eV$.

Similarly, in Ca_2RuO_6 the transition has been identified upon applied pressure and strain [102, 137]. Thus, a microscopic description of the current-induced insulator-to-metal transition necessitates an accurate knowledge of the atomic positions in-equilibrium and out-of-equilibrium as well as the inclusion of correlation effects. Within neutron and X-ray diffraction experiments – for details we refer to Ref [19] – it has been found that the non-equilibrium phase assumes a unique crystal structure distinct from those of the equilibrium metallic phases leading to distinct electronic band-structure.

Based on the refined atomic positions, summarized in Table 4.1, we have performed *ab initio* electronic structure calculations in order to study the sensitivity of the electronic state to the crystallographic distortions in all phases: the equilibrium S-phase, the non-equilibrium semi-metallic S^* phase and the non-equilibrium metallic L^* phase. In the following sec-

tions, we will first present the methodological details involved before we discuss our results and finally draw conclusions.

Phase	S-phase	S*-phase	L*-phase
Temperature (K)	130	130	130
a (Å)	5.3842(8)	5.404(4)	5.341(5)
b (Å)	5.6158(9)	5.547(4)	5.436(6)
c (Å)	11.7461(11)	11.848(8)	12.153(9)
Volume (Å^3)	355.16(3)	355.2(2)	352.8(3)
Orthorhombicity (b—a)	0.23	0.14	0.10
Ru–O(1)a (Å)	2.0132(11)	2.001(4)	1.964(4)
Ru–O(1)b (Å)	2.0161(10)	2.005(3)	1.968(5)
Ru–O(2) (Å)	1.9683(11)	1.979(4)	2.021(4)
Ru–O avg (Å)	1.999	1.995	1.984
Ru–O ratio	1.023	1.012	0.972
Θ–O(1) (°)	12.79(1)	12.43(4)	10.69(4)
Θ–O(2) (°)	11.53(1)	10.65(4)	9.76(4)
Φ (°)	11.965(3)	11.874(10)	12.034(11)

Table 4.1: Neutron diffraction structural refinement in the orthorhombic $Pbca$ space group. Ru–O bonds and RuO_6 octahedral parameters at $T = 130\,\mathrm{K}$ of the S-phase and S*- and L*-phases at $J = 10\,\mathrm{A\,cm^{-2}}$. Θ–O(1) refers to the tilt angle between the basal plane and the ab-plane, Θ–O(2) is the angle between the RuâĂŞO(2) bond and the c-axis, and Φ is rotation of the RuO_6 around the c-axis. The Ru–O ratio compares the apical and averaged in-plane Ru-O bond lengths, and is a measure of the tetragonal distortion. Taken from Ref [19].

4.1.1 Models and technical details

For our calculations, we have employed the well-established merger of density functional theory (DFT) and single-site dynamical mean-field theory (DMFT), in its one-shot variant (no charge self-consistency), as discussed in detail in Chapter 1. The experimentally refined atomic positions have been used as input for the DFT calculations which have been carried

out using the WIEN2K code [88] with a full potential linearized augmented planewave method and with the Perdew/Burke/Ernzerhof parametrization of the generelized gradient approximation as the exchange-correlation functional [108]. The effective – material and phase dependent – models have been derived by projecting the converged DFT wavefunctions on a Wannier basis in the energy window $[-1, 2]\ eV$ around the Fermi level.

The low energy window is spanned by four t_{2g} subspaces, each one corresponding to one of the four Ru-sites in the unit cell. Note, however, that the label t_{2g} is strictly precise only in the case of a cubic environment and that the lower-in-symmetry distortions introduce off-diagonal matrix elements in the local crystal-field potential. Furthermore, we have introduced the local spin-orbit coupling operator on each Ru-site as the t_{2g} projection of the $H_{\mathrm{so}} = \zeta \sum_i^{N_e} \boldsymbol{l}_i \boldsymbol{s}_i$. Here, the spin-orbit coupling strength, ζ, is approximated by its Hartree-Fock value $\zeta = 0.16\ eV$ [1] and the summation runs over all N_e electrons.

Regarding the (screened) Coulomb interaction kernel, it has been approximated by the rotationally invariant Kanamori operator [64] and parametrized – as in previous studies [67, 100] – with $U = 1.9\ eV$ and $J_H = 0.4\ eV$ for all Ru-sites in all studied models. The total particle filling is adjusted to 16 electrons per unit-cell that corresponds to a t_{2g}^4 average configuration of each Ru subspace. Note that since our energy window contains only states that are treated as correlated, no double counting correction term is needed to be considered.

For the very solution of the DMFT auxiliary impurity models, we have employed the state-of-the-art continuous-time quantum Monte Carlo solver (CT-QMC), in its hybridization expansion variant (CT-HYB) [116]. After the DMFT convergence has been reached, the resulting impurity models have been further used to generate a statistical ensemble of 100 independent solutions of high QMC-statistics in order to minimize the unavoidable QMC noise and obtain high quality of results on the imaginary axis. The (average) interacting Green's function and self-energy have been analytically continued onto the real frequency axis; here we have employed the maximum entropy method (MEM) following Kraberger *et al.* [74].

An important remark should be made at this point. As is the case for most QMC calculations

	S	S^*	L^*	$T = 400\ K$
n_{xz}	1.11	1.16	1.28	1.34
n_{yz}	1.13	1.14	1.25	1.32
n_{xy}	1.76	1.70	1.47	1.34
n_{tot}	4.00	4.00	4.00	4.00

Table 4.2: Occupation numbers of the t_{2g} orbitals from DMFT calculations.

in similar systems, we have been confronted by the presence of severe QMC sign-problem and thus restricted our simulations in terms of the reachable temperature. This is due to the fact that common simplification schemes that involve, for instance truncation of small off-diagonal elements on the level of the Wannier Hamiltonians [67], cannot be employed for our study: most of the structural dependence of our models *is* in fact encoded on those elements. Hence, all our calculations are performed at $T = 390\ K$ where the average sign – in the most difficult S^*-phase – has been 0.38. Lastly, we emphasize that the calculation temperature should be distinguished from the *physical temperature* which, already, is strongly reflected by means of the corresponding lattice structures.

4.1.2 Results and discussion

We start our discussion from the *non-interacting* Wannier Hamiltonians. In all cases the cubic symmetry is broken and we find sizable tetragonal crystal-field splittings of $E_{xy} \neq E_{xz/yz}$. Further small orthorhombic distortions lead to an additional splitting – which is of two orders of magnitude smaller than the tegragonal one – of $E_{xz} \neq E_{yz}$. Here we observe a clear trend: the tetragonal crystal-field splitting , $\Delta_p = E_{xz/yz} - E_{xy}$, decreases as the current drives the system from the equilibrium S-phase, where $\Delta_p = 0.32\ eV$, to the non-equilibrium S^*- and L^*-phase, where $\Delta_p = 0.29\ eV$ and $\Delta_p = 0.19\ eV$ respectively. When considering interactions and include correlation effects through DMFT, this material's trend is still present and is reflected on the partial orbital occupations of the t_{2g} orbitals, that we summarize in Table 4.2. In particular, the largest orbital polarization is observed for the S-phase and the non-equilibrium S^*, despite the qualitative change in the metallicity of

the latter. In addition, the L^* and $T = 400\ K$ phases have similar orbital fillings as a result of their structural similarity. In Fig. 4.2, we show the DMFT self-energies and the

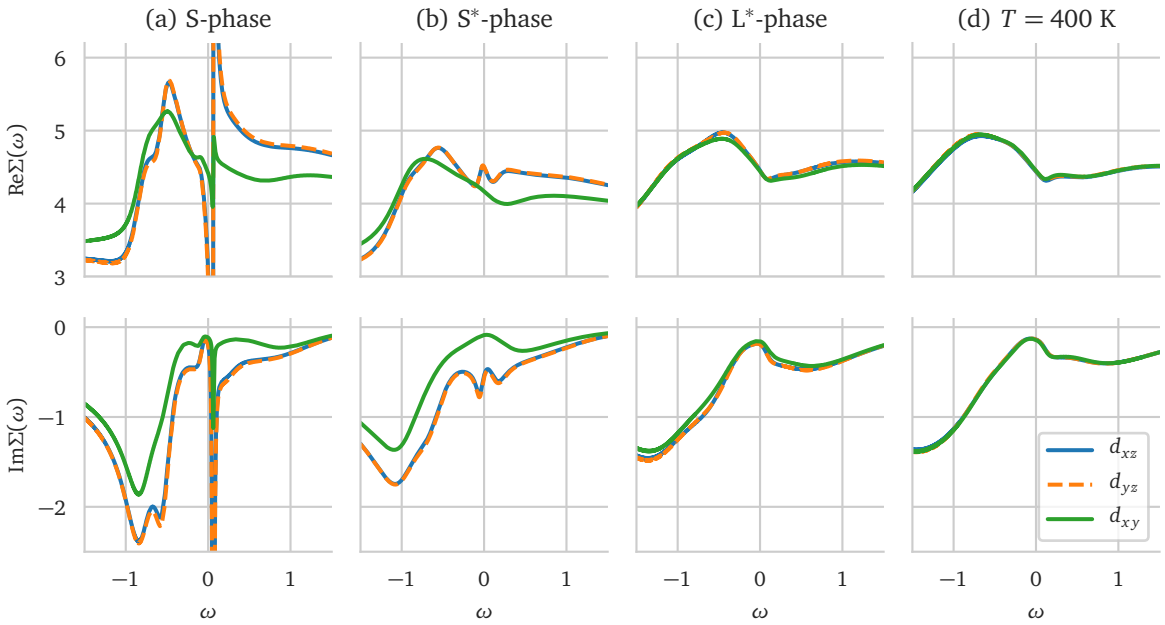

Fig. 4.2: Analytically continued self-energies $\Sigma(\omega)$ for all phases. (top) The real-part of the self-energy. (bottom) The imaginary-part of the self-energy. Here we show only the diagonal elements and restrict the visualization on the spin-up block of $\Sigma(\omega)$.

local spectral functions on the real frequency axis for all phases. Note the well-defined Fermi-liquid-like behavior – linear (real part) and quadratic (imaginary part) around the $\omega = 0\ eV$ – for the $T = 400\ K$, L^*- and S^*-phase, and the development of a pole when crossing the metal-to-insulator transition line and enter the S-phase [1].

In turn, the analytically continued self-energies allows us to obtain the corresponding k-resolved spectral functions, $A(\omega, \mathbf{k})$, in a numerically consistent manner [2] – as discussed in Section 1.6. In Fig. 4.4, we show the $A(\omega, \mathbf{k})$ for all studied phases in a small energy window

[1] At this point we note that the AC of the insulating self-energy poses a real challenge due to the presence of large off-diagonal elements.

[2] For the cross validation of the AC procedure of the self-energies we have compared the corresponding local spectral functions, $A(\omega)$, as obtained from a direct AC of the local Green's functions and the explicit summation of the $A(\omega, \mathbf{k})$ over the whole Brillouin zone.

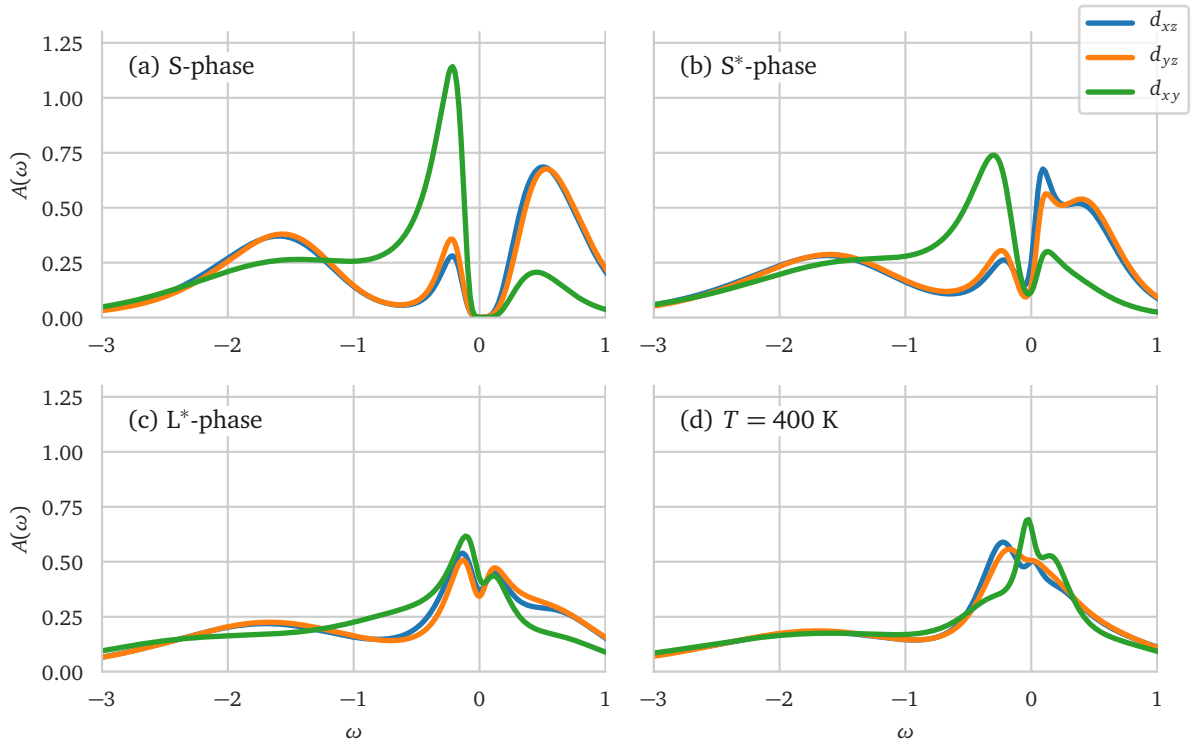

Fig. 4.3: Orbital-resolved local spectral functions $A(\omega)$ (in units of $1/eV$) for all studied structures, as obtained from the analytical continuation of the local Green's function, $G_{\text{loc}}(i\omega_n)$, on the low frequency regime. Here we show only the diagonal elements and restrict the visualization of the spin-up block.

near the Fermi level, while in Fig. 4.3, we extend the energy interval and plot the corresponding local spectra, $A(\omega)$. We find the equilibrium S-phase to be Mott-insulating with a charge gap of $\sim 0.2\ eV$. The gap is formed between a d_{xy} dominated lower-Hubbard band and a $d_{zx/yz}$ dominated upper-Hubbard band. The agreement of the DMFT results with experimental ARPES data [129, 111] is satisfactory: wide and dispersive d_{xy}-character band is located around $-2.0\ eV$ same as seen in experiment. Further d_{xy}-weight is located at $-0.3\ eV$ which is slightly closer than the experimental value of $-0.5\ eV$. On the other hand, the $d_{xz/yz}$ spectral weight is mostly distributed in a non-dispersive and incoherent broad band spanning from $-2.0\ eV$ to $-1.0\ eV$ while small contributions – that originate from the spin-orbit coupling mixture with the d_{xy} excitations at the same energy scale – are also found around $-0.3\ eV$, in excellent agreement with the experiment.

Driving the S-phase to the S^*-phase results in a redistribution of spectral weight from the Hubbard bands towards the Fermi level.The transfer of the spectral weight closes the insulating gap and create a *semi-metallic* phase. Qualitatively, the hole (electron) pockets are derived mostly from the d_{xy} ($d_{xz/yz}$) bands – although the spin-orbit coupling certainly mix the orbital character. Note, that the structure of the high-energy Hubbard bands remains very similar to the equilibrium S-phase one. Larger currents stabilize the L^*-phase, where tetragonal and orthorombic distortions are further reduced, and even larger transfer of spectral weight towards the Fermi level.

4.1.3 Conclusions

In conclusion, we have investigated the equilibrium and current-driven non-equilibrium phases of Ca_2RuO_4, on the single-particle level by means of DFT+DMFT, exploiting the knowledge of the exact atomic positions as have been obtained by neutron and X-ray diffraction experiments.

We have found that all t_{2g} orbitals contribute both in the formation of the Hubbard bands as well as in the character of quasiparticle bands around the Fermi level; no full orbital polarization has been found. Our results are in excellent agreement with experimental evidence and reveal the extreme sensitivity of the electronic band structure to even minor structural changes in the current induced state. Thus, they make it clear that the structural details must be explicitly considered in any model to describe the mechanism that drives the anomalous diamagnetism under direct current, such as the Dirac point formation proposed by Sow *et al.* [121].

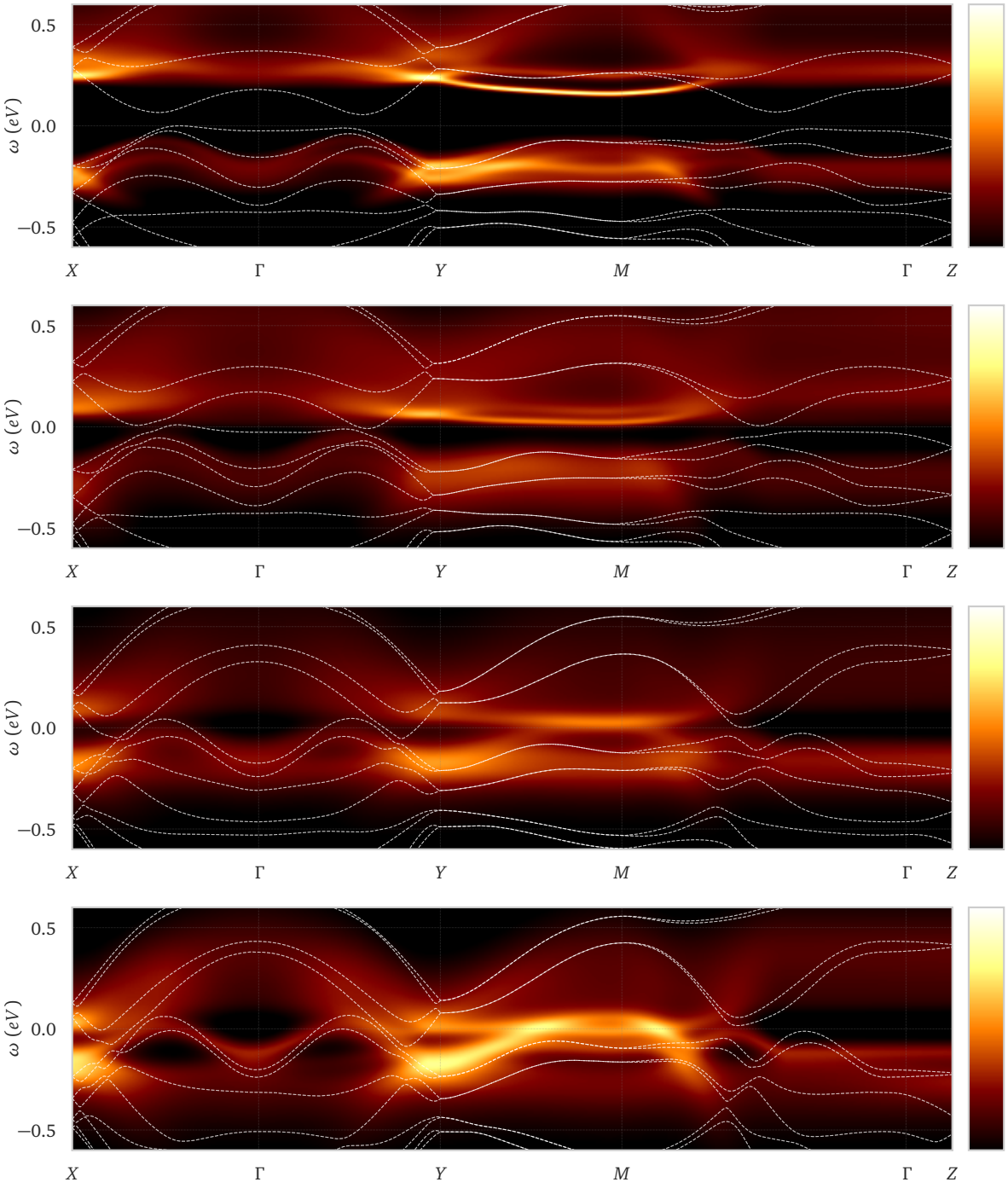

Fig. 4.4: DMFT-calculated intensity map for electrons spectral function $A(\omega, \mathbf{k})$ (in arbitrary units, dark (light) color implies low (high) intensity) as a function of the energy ω (counted from the chemical potential) and momentum $\mathbf{k}$ along the high-symmetry points in the orthorhombic Brillouin zone. From top to bottom: the equilibrium S-phase, the non-equilibrium S^*— and L^*— phases, and the $T = 400\ K$ structure from Ref [38]. The DFT+U mean-field bands are shown in white dashed lines.

4.2 Response of t_{2g}^4 systems in non-spherical potentials

During the last decades, advancements both in the theoretical and computational machinery have triggered even more the interest into the physics of the so-called strongly correlated fermionic. systems, through the study of effective model Hamiltonians that represent whole classes of real materials.

The very construction of those models is typically based on recognizing the relevant degrees of freedom and the associated energy scales that govern the system's properties. If present, a clear hierarchy of those energy scales is of great use; not only it directly connects with the existence of good quantum numbers – thus an optimal single particle basis to formally express the model itself – but also allows for further approximation schemes to be considered. For instance, transition metal compounds of the 3d series are usually characterized by dominant crystal-field potentials, hence one usually labels the single particle states according to the irreducible representations of the underlying lattice symmetry; that is the t_{2g} and e_g states in the case of cubic (octahedron) crystal field. On the other hand, in rare-earth (4f-series) compounds spin-orbit coupling dominates over the crystal-field energy-scales and thus renders the total angular momentum – the eigenbasis of spin-orbit coupling – to be the single-particle basis of choice. In between, the 4d and 5d compounds pose a real challenge in that respect. There, both crystal-field and spin-orbit coupling effects act on similar energy scales: no *good* single particle basis exist.

Here, we make use of a generic t_{2g} model Hamiltonian, which has been extensively employed for the study of early-in-series transition metal compounds under the initial assumption that the energy splitting between the irreducible representations is sufficiently large so that the low temperature dynamics involves only the lowest t_{2g} states. On top we consider the effect of both spin-orbit coupling and (additional) crystal-field splitting as induced from distortions of the perfect octahedron. Our study focus on the single- and most importantly on the two-particle observables, such as the magnetic susceptibility.

The following sections are organized as follows. In Section 4.2.1 we will describe in detail the model that has been used in this work together with the methodologies that have been

employed for its solution. In Section 4.2.2 and 4.2.3, we present and discuss our results. In Section 4.2.4, we summarize our conclusions and draw future plans.

4.2.1 Models and methods

We consider the t_{2g} multiorbital extension of the Hubbard Hamiltonian, which reads as,

$$\hat{H} = \sum_{ij}\sum_{\alpha\beta} T_{ij}^{\alpha\beta}\hat{c}_{i\alpha}^{\dagger}\hat{c}_{i\beta} + \sum_{i}\sum_{\alpha\beta\gamma\delta} U_{\alpha\beta\gamma\delta}^{(i)}\hat{c}_{i\alpha}^{\dagger}\hat{c}_{i\beta}^{\dagger}\hat{c}_{i\gamma}\hat{c}_{i\delta} - \mu\sum_{i\alpha}\hat{n}_{i\alpha}, \tag{4.1}$$

where Latin letters denote lattice sites and Greek letters stand for the collective spin-orbital indices $a \equiv \{d_{yz}^{\uparrow} d_{xz}^{\uparrow} d_{xz}^{\uparrow}, d_{yz}^{\downarrow} d_{xz}^{\downarrow} d_{xz}^{\downarrow}\}$; $\hat{c}_{i\alpha}^{\dagger}$ ($\hat{c}_{i\alpha}$) create (destroy) at electron at lattice site i with index a, $U_{\alpha\beta\gamma\delta}^{(i)}$ is the fully rotational invariant 4-index local interaction kernel and μ is the chemical potential that fixes the total particle density of the system. $T_{ij}^{\alpha\beta}$ stands as the matrix representation of all local and non-local single-particle operators acting on the system, namely:

$$T_{ij}^{\alpha\beta} \equiv t_{ij}^{\alpha\beta}(1-\delta_{ij}) + (\Delta_{\text{cf}}^{\alpha\beta} + \Delta_{\text{so}}^{\alpha\beta})\,\delta_{ij}, \tag{4.2}$$

where $h_{ij}^{\alpha\beta}$ stands for the hopping integrals of the model and $\Delta_{CF}^{\alpha\beta}$ ($\Delta_{\text{so}}^{\alpha\beta}$) corresponds to the matrix-representation of the crystal-field (spin-orbit coupling) operators in the corresponding single-particle basis. Regarding the hopping integrals, we have allowed for only nearest-neighbor hopping of an isotropic form, namely $t_{ij}^{\alpha\beta} = -t\,\delta_{\alpha\beta}\,\delta_{|i-j|=1}$. The spin-orbit coupling operator has been constructed by utilizing the $T-P$ equivalence: comparing the matrix-elements of the single-particle momentum operator of the full d- and p-shell identifies a mapping between the t_{2g} states and the latter using the relation $\boldsymbol{l}(t_{2g}) = -\boldsymbol{l}(p)$. Note, however, that the $T-P$ equivalence mapping holds under the assumption that the e_g states lie far above the t_{2g} ones [123]. Effectively, this corresponds to neglecting the off-diagonal elements between the irreducible representations' manifolds, and thus obtaining a partial quenching $l = 1$ of the angular momentum – the e_g states are non-magnetic. The interaction kernel is parametrized by two radial integrals F^0 and F^2 or equivalently to intra-orbital interaction U and the Hund's coupling J.

The general formulation of the above Hamiltonian allows us to study separate cases characterized by different hierarchy of energy scales, all in the same framework. In particular,

we define the following:

- The crystal-field only model (m-CF), where we set $\Delta_{\mathrm{so}}^{\alpha\beta} = 0$ and assumed a tetragonal elongating crystal-field that results in splitting upwards the d_{xy} orbital by an energy scale of t and yields an anisotropy between the xy-plane and the perpendicular z-axis.

- The spin-orbit coupling only model (m-SO), where we set $\Delta_{\mathrm{CF}}^{\alpha\beta} = 0$ in which the spin and orbital momenta are mixed but the total angular momentum is a conserved quantity. The spin-orbit coupling strength is set to be $\zeta = \frac{2t}{3}$.

- The aggregated model (m-CFSO) in which both spin-orbit coupling and tetragonal crystal-field effects are taken into account on equal footing.

Note that we have chosen the parametrization of the spin-orbit coupling to be such that the local energy-level structure of the m-CF and m-SO is equivalent – a four-fold and a two-fold degenerate subspace – while the *orbital character* of their local eigenstates critically differ. The average filling for all calculations and for all models is fixed to be $N = 4$. We have investigated the above mentioned models in three regimes: **(i)** the weak coupling regime, **(ii)** the atomic-limit regime and **(iii)** the intermediate regime.

Starting from the weak-coupling regime, we have employed the matrix formulation of the random-phase approximation, as it has been introduced, in detail, in Chapter 2. To recap, the random-phase approximation is a weak-coupling approach in which the summation of diagrams of bubble and ladder topology up to infinite order is considered, or equivalently it stands as the zero order approximation of the 4-index vertex function within the BSEs view. The objective, here, is the generalized response function, $\chi^{\mathrm{gen}}_{\alpha\beta\gamma\delta}(\boldsymbol{q}, i\nu_n)$, and the *building blocks* of the methods are the non-interacting generalized susceptibility, $\chi^{0,\mathrm{gen}}_{\alpha\beta\gamma\delta}(\boldsymbol{q}, i\nu_n)$ and the bare local interaction kernel $U_{\alpha\beta\gamma\delta}$. The former can be easily obtained by a convolution of the non-interacting lattice propagators as,

$$\chi^{0,\mathrm{gen}}_{\alpha\beta\gamma\delta}(\boldsymbol{q}, i\nu_n) = -\frac{1}{\beta}\sum_{\boldsymbol{k}}\sum_{\omega_n} G^0_{li}(\boldsymbol{k}+\boldsymbol{q}, i\omega_n + i\nu_n) G^0_{jk}(\boldsymbol{k}, i\omega_n), \tag{4.3}$$

while when written in a spin-block notation, $\chi^{0,\mathrm{gen}}_{\alpha\beta\gamma\delta}$ reads as,

$$\chi^{0,\mathrm{gen}}(\boldsymbol{q}, i\nu_n) = \begin{pmatrix} \chi^0_{\uparrow\uparrow\uparrow\uparrow} & \chi^0_{\uparrow\uparrow\uparrow\downarrow} & \chi^0_{\uparrow\uparrow\downarrow\uparrow} & \chi^0_{\uparrow\uparrow\downarrow\downarrow} \\ \chi^0_{\uparrow\downarrow\uparrow\uparrow} & \chi^0_{\uparrow\downarrow\uparrow\downarrow} & \chi^0_{\uparrow\downarrow\downarrow\uparrow} & \chi^0_{\uparrow\downarrow\downarrow\downarrow} \\ \chi^0_{\downarrow\uparrow\uparrow\uparrow} & \chi^0_{\downarrow\uparrow\uparrow\downarrow} & \chi^0_{\downarrow\uparrow\downarrow\uparrow} & \chi^0_{\downarrow\uparrow\downarrow\downarrow} \\ \chi^0_{\downarrow\downarrow\uparrow\uparrow} & \chi^0_{\downarrow\downarrow\uparrow\downarrow} & \chi^0_{\downarrow\downarrow\downarrow\uparrow} & \chi^0_{\downarrow\downarrow\downarrow\downarrow} \end{pmatrix} (\boldsymbol{q}, i\nu_n) \,. \tag{4.4}$$

Every element of the above matrix form shall be considered as 9×9 (orbital-indexed) matrix. In the same notation the 4-index interaction kernel reads:

$$U = \begin{pmatrix} U_{\uparrow\uparrow\uparrow\uparrow} & 0 & 0 & U_{\uparrow\uparrow\downarrow\downarrow} \\ 0 & U_{\uparrow\downarrow\uparrow\downarrow} & 0 & 0 \\ 0 & 0 & U_{\downarrow\uparrow\downarrow\uparrow} & 0 \\ U_{\downarrow\downarrow\uparrow\uparrow} & 0 & 0 & U_{\downarrow\downarrow\downarrow\downarrow} \end{pmatrix} . \tag{4.5}$$

The structural differences in the above matrices come as a result of the $SU(2)$ symmetry: the Coulomb repulsion is always spin-conserving, thus independently from the model at hand the above notation always holds. If the spin quantum number is conserved by the quadratic part of the Hamiltonian – and this is the case only for the m-CF –, the non-interacting generalized susceptibility simplifies to the interaction matrix-form. Regardless of symmetry conservations, the generalized susceptibility is obtained by Eq. 2.20, and does not pose any computational challenge for any set of parameters. In the extreme opposite regime, setting $t^{\alpha\beta}_{ij} = 0$, one arrives to the atomic limit, which serves in our case as a reference point. As in the weak-coupling regime, we can obtain the exact solution for any parametrization of the remaining terms. Diagonalizing the Hamiltonian, we access the eigenenergies and eigenstates of the system, thus we can obtain any physical quantity.[3] For instance, in Fig. 4.5, we show a cumulative energy-level diagram of the t^4_{2g} atomic-limit configuration, where we only tune the parametetrization of its quadratic part – crystal-field and spin-orbit coupling. The two boundaries of the figure correspond to the case where neither spin-orbit coupling or crystal-field splittings occur. The figure is (conceptually) divided into three regions and the color denotes the expectation value $\langle J^2 \rangle$. Starting from the very left of the figure towards the center, the strength of the spin-orbit coupling increases

[3] For all atomic-limit calculations we have used the **Quanty** codebase [54].

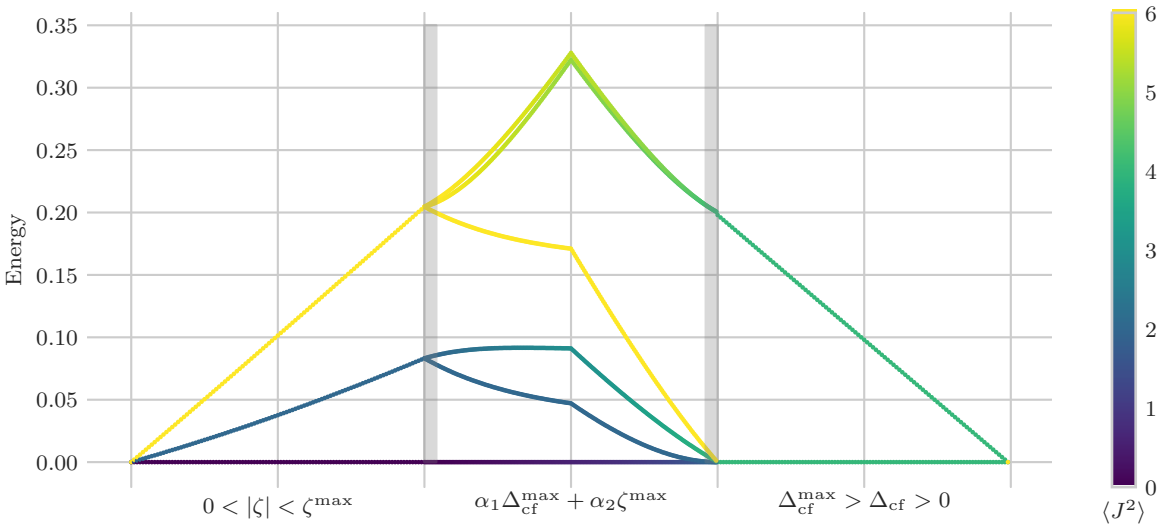

Fig. 4.5: The energy level diagram of the lowest lying states in the atomic limit. The color encodes the expectation value of the J^2 operator averaged of the corresponding degenerate states. We refer to the text for further explanations.

and the total-angular momentum subspaces $\boldsymbol{J} = 0, 1, 2$ continuously split. Similarly, from the very right towards the central panel again the states split and form a 6-fold and 3-fold degenerate subspace. The central panel corresponds to the case where both single-particle operators are considered. The grey-filled areas denote the regime where one or the other single-particle operators can be treated as perturbatively. Of particular interest for this study is the isothermal response, $\chi^{\rm at}_{AB}$, which for can be evaluated as,

$$\chi^{\rm at}_{AB} = \frac{1}{Z}\sum_{m,n}\langle\psi_n|\hat{A}|\psi_m\rangle\langle\psi_m|\hat{B}|\psi_n\rangle\left[\beta e^{-\beta E_n}\delta(E_n - E_m) - \frac{e^{-\beta E_n} - e^{-\beta E_m}}{E_n - E_m}\big(1 - \delta(E_n - E_m)\big)\right], \tag{4.6}$$

where ψ_n (E_n) is the m-th eigenstate (eigenenergy) of the atomic Hamiltonian; β is the inverse temperature and Z is the atomic partition function. The first term of of Eq. (4.6) corresponds to the Curie-Weiss part of the susceptibility and contributes in the presence of degenerate subspaces. The second term, in contrast, *connects* with non-degenerate subspaces, is almost temperature-independent and forms the so-called Van Vleck part.

In Fig. 4.6, we plot the isothermal magnetic response along the $z-$ and x-axis, as obtained from Eq. 4.6) for three different models: (left) spin-orbit coupling case, (center) crystal-

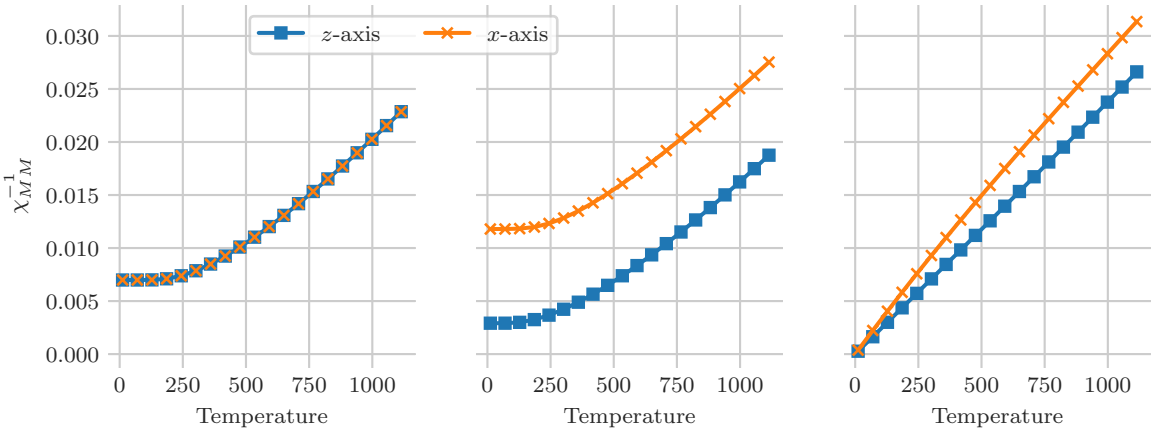

Fig. 4.6: The isothermal magnetic response along the z- and x-axis in the atomic limit: (left) spin-orbit coupling, (right) tetragonal crystal-field, and (middle) both spin-orbit coupling and crystal-field operators included.

field and spin-orbit coupling case and (right) crystal-field case. Note that although we have chosen the values of the SO and CF such that the splittings on the single particle level are equal, the two-particle response clearly distinguishes between the action of the corresponding operator. For instance, the magnetic response of the SO system is spherically symmetric while a clear in- and out-of-plane anisotropy is found – as expected – in the CF system. Additional information can be also extracted when considering again Fig. 4.5. For high temperatures all systems show a Curie-Weiss behavior as a result of the thermal activation of degenerate subspaces. As the temperature decreases, the Bolzmann factors act as a cut-off of relevant states. Eventually, in the SO system the last-standing subspace, $J = 0$, is non-degenerate and thus only the Van Vleck part contributes. In the CF system, the 9-fold degeneracy of the ground-state allows for the dominant Curie-Weiss part to contribute the most. In between, both contributions become relevant and their effect together with the anisotropy should be visible – at least at some extend – even when the lattice degrees of freedom are introduced.

To study the intermediate coupling regime, we have employed the dynamical mean-field theory (DMFT), in which the original lattice problem is mapped onto an effective impurity model embedded self-consistently into a bath of non-interacting; the underlying approx-

imation is that the self-energy is momentum-independent yet fully dynamic. Regarding the very solution of the corresponding impurity problem, we have used the continuous-time Quantum Monte Carlo in hybridization expansion variant (CT-HYB) [116], which in principle allows to consider full-rotational invariant interactions and (real or complex) off-diagonal elements in the hybridization function.

We will focus on two objectives throughout the study of the different models: single-particle spectral functions and uniform and static response functions. Given that a full self-consistency is reached, and by performing the necessary analytical continuation [4] step to obtain the local Green's function into the real frequency axis, the local spectral function is calculated as,

$$A(\omega) = -\frac{1}{\pi}\sum_{a} \mathrm{Im} G^{\mathrm{loc}}_{\alpha\alpha}(\omega). \tag{4.7}$$

In general, the calculation of two-particle response functions necessitate access to the two-particle vertex [5]. Here, we restrict ourselves to the linear response regime in order to exploit the fact that the uniform and static susceptibilities, χ_{AB}, can be calculated as,

$$\chi_{AB}(\boldsymbol{q},\omega)\Big|_{\substack{\omega=0\\ \boldsymbol{q}=0}} = b_s^{-1}\mathrm{Tr}\,[\tilde{\rho}_B \tilde{A}], \tag{4.8}$$

where b_s is the strength of the field that couples to an operator $\hat{B}$ and is acting as a perturbation to the original Hamiltonian of system, $H_{\mathrm{per}} = \hat{H} - b_s\hat{B}$; $\tilde{\rho}_B$ is the one-particle density matrix of the perturbed system at hand.

At this point we should note that the absence of good quantum numbers leads to (severe) QMC fermionic sign-problem, which in turn hinders the solution – and ultimately the convergence – of the corresponding impurity models. Thus the calculations were limited to rather high-temperatures within adjusted natural single-particle basis. Regarding the convergence of the single-particle density matrices in the presence of small perturbations, it has been necessary to obtain an extended sample of measurements. Small perturbation result in small elements in the hybridization function, which, in turn, are comparable with

[4] For completeness, the analytical continuation of the single-particle Green's functions has been obtained using the stochastic optimization method (SOM) [76]

[5] And additionally, DMFT is not self-consistent on the two-particle level.

the unavoidable numerical QMC noise. Therefore, in all cases shown below, we have obtained 30 independent measurements with high QMC statistics ($\sim 10^8 - 10^9$ cycles) and performed a statistical analysis.

4.2.2 Results: Comparison in the one-particle level

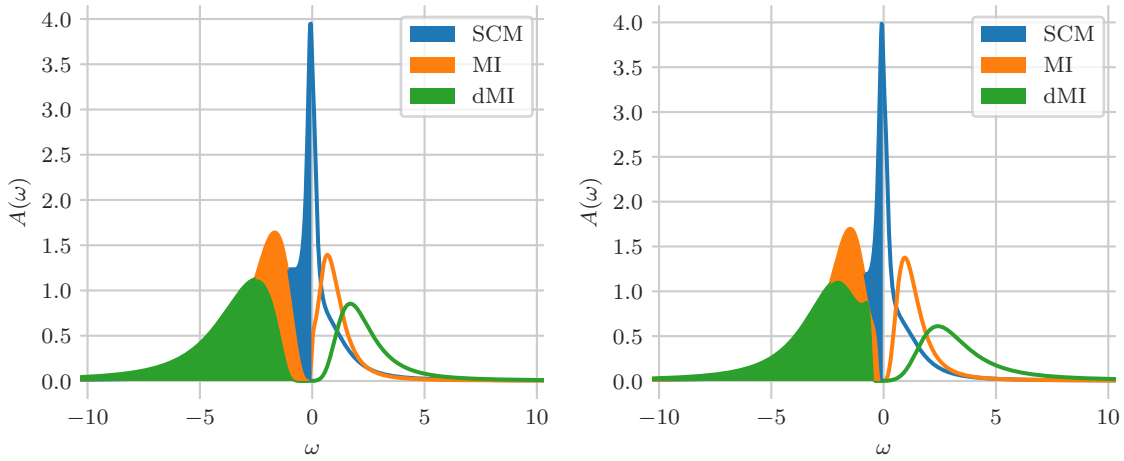

Fig. 4.7: Comparison of the single-particle spectral functions at fixed inverse temperature $\beta = 20\ eV^{-1}$ for selected values of the on-site Hubbard interaction – (blue) $U = 2.5\ eV$, (orange) $U = 3.5\ eV$ and (green) $U = 6.0\ eV$ – that correspond to different points in the complete phase-diagram. (right) Spectral functions for the m-CF case. (left) Spectral functions for the m-SO case.

We start our discussion with the comparison of the extreme-cases on the single-particle level. Namely, we consider effects either of the tetragonal crystal-field (m-CF) or a spin-orbit coupling (m-SO). In Fig. 4.7, we show for both models the local spectral functions for three selected values of the interaction at fixed inverse temperature $\beta = 20\ eV^{-1}$. Each one corresponds to a characteristic point in the complete phase-space:

- A strongly correlated metallic (SCM) solution, which is characterized by a sharp (thus coherent) quasiparticle peak on the Fermi-surface ($\omega = 0$), and corresponds to an intra-orbital interaction strength $U = 2.5\ eV$.

- An Mott-insulating solution (MI), right after the metal-to-insulator transition, obtained at $U = 3.5\ eV$. Here, the upper and lower Hubbard bands are fully formed and a charge gap is (just) opened.
- A solution (dMI) far away from the metal-to-insulator transition line, deep within the Mott phase, at $U = 6.0\ eV$.

In both cases, m-CF and m-SO, we have determined the metal-to-insulator transition to occur at $U_c = 3.0\ eV$. Note that the ratio of the intra-orbital interaction and Hund's coupling strength is kept fixed as $J = 0.1\ U$. Moreover, we find that the differences of the local spectra with respect to their structural features are almost negligible. It is only the rather small *bumb* on the edge of the lower Hubbard band for the MI solution, which originates from the multiplet structure in presence of the SOC operator, that can be used as a hint to distinguish the two – fundamentally different – physical systems.

Other than this faint detail the models are indistinguishable: the orbital character and the symmetries of each model are to a large extend and misleadingly smeared when looking at single-particle observables.

4.2.3 Results: Uniform and static response functions

As has been shown in the previous section, the symmetry and orbital character of the m-CF and m-SO are not clearly visible within the single-particle local spectral functions. On the two-particle level, however, due to the (greater) sensitivity upon the symmetries of the Hamiltonian the distinct effects of crystal-field and spin-orbit coupling can be captured.

In Fig 4.8, we show the inverse uniform and static magnetic susceptibility as a function of temperature down to room-temperature for the same interaction regime discussed above [6]. For completeness, on each subplot we have included both the (exact) atomic-limit reference system and the results in the weak-coupling regime treated within the multiorbital generalization of RPA.

[6] For clarity we have omitted the error-bars for all our DMFT response functions' calculations.

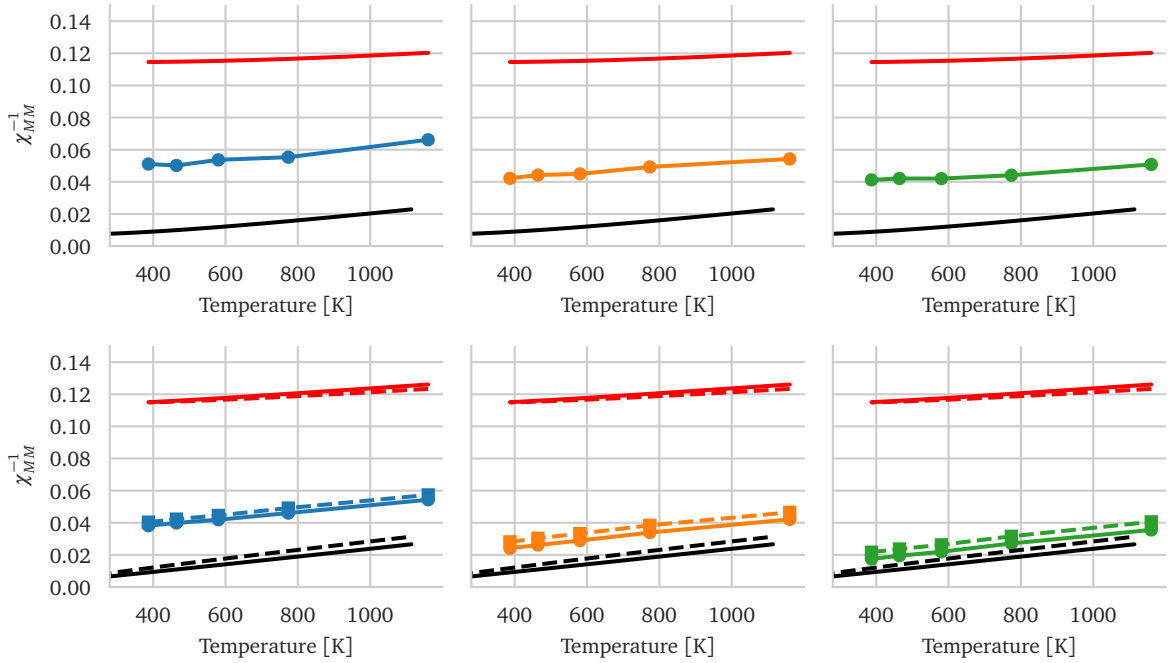

Fig. 4.8: The inverse uniform and static magnetic response corresponding to the $m-SO$ (upper panels) and to the $m-CF$ (lower panels) case, respectively. From left to right we move from the SCM regime into the dMI regime. With black (red) color we plot the exact atomic-limit (RPA) susceptibilities. For the DMFT results we use the same color-encoding as in the case of the local spectral functions. Solid lines correspond to an applied field along the z-axis, while dashed in the x/y-axis.

For both m-CF and m-SO systems, we find profound atomic features in the dMI-regime, which start to get mediated by the lattice degrees of freedom as we move towards the MI-regime. Interestingly, even when cross the line and enter the CM-regime, the localized magnetic moments only moderately washed out by the itinerant energy scale and still show *atomic-like* behavior. In the m-CF case, the anisotropy that originates from the tetragonal crystal-field potential clearly comes into view [7]. On the other hand, in the m-SO case, due to the spherical symmetry – that the local spin-orbit coupling conserves – the magnetic response is isotropic in all directions.

[7] The numerical effort needed together with the severe QMC sign problems we have experienced due to the specific variant of QMC that we have employed do not allow in which point the very interesting inversion of the easy-axis occurs.

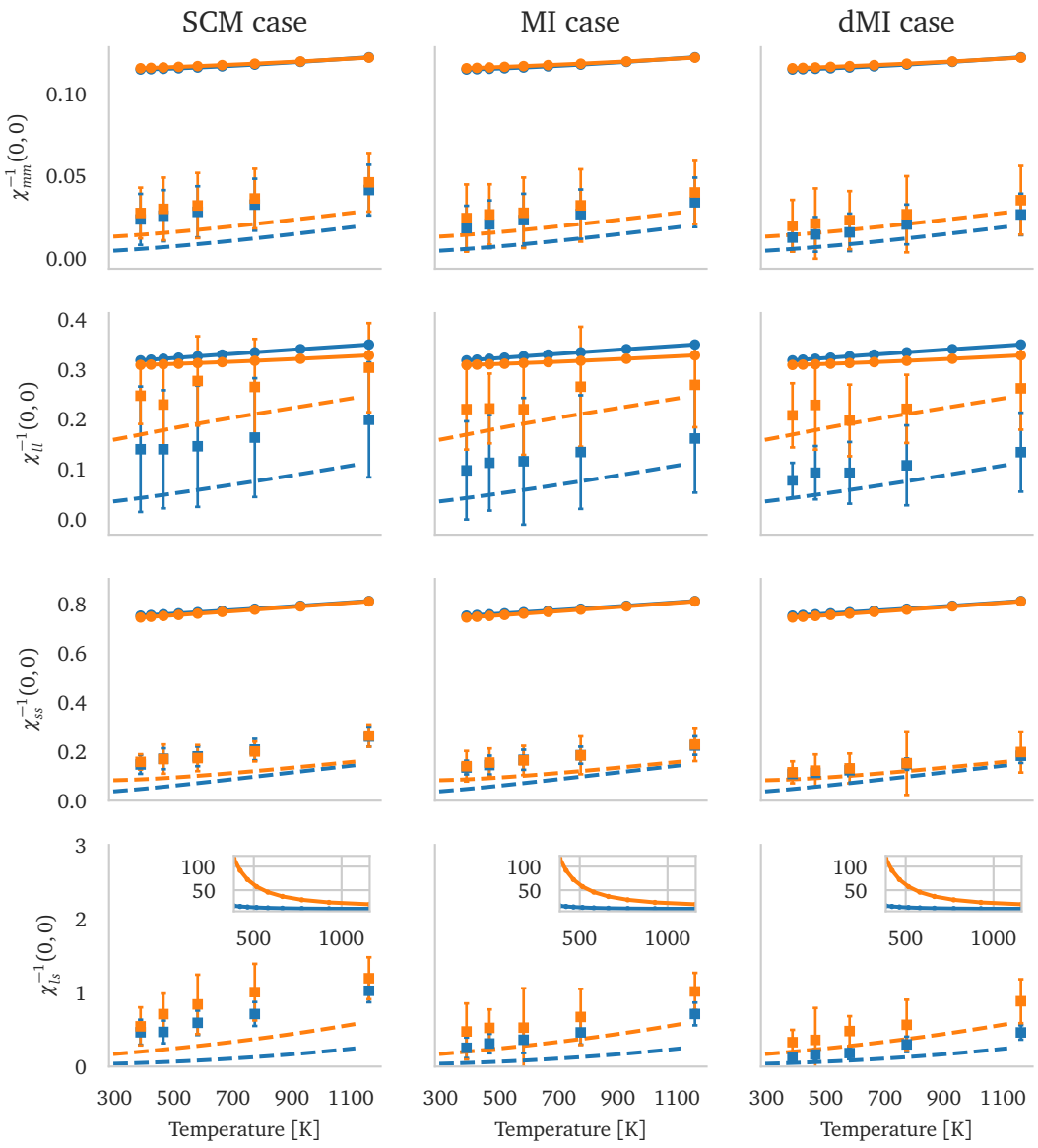

Fig. 4.9: The inverse uniform and static susceptibilities for the m-CFSO case. From top to bottom (row-wise): the magnetic, orbital, spin and orbital-spin susceptibilities. From left to right (column-wise): strongly correlated metallic, insulating and deep insulating phase. With blue (orange) we depict the data for the z-axis (x/y-axis). Dashed lines are used for the exact atomic-limit values while solid lines correspond to the data on perturbative regime as obtained by RPA.

The full problem: Crystal field and spin-orbit coupling effects

Having compared the two limiting cases, we now consider the m-CFSO case in order to capture the effect of the interplay and of both single-particle operators. Following the same procedure as before, we have obtained the response of the system in three characteristic points of the complete phase-diagram: one SCM, one MI and one dMI. Furthermore, we have disentangled the various channels that contribute to the final magnetic response, namely the spin-spin, orbital-orbital and spin-orbital susceptibility.

In Fig. 4.9, we present our DMFT results together with the corresponding atomic-limit and RPA ones that serve as a reference points.[8] Again, we find a linear temperature dependence for all strengths of the on-site interaction in all channels. Note, however, the effects of the tetragonal crystal-field and spin-orbit coupling: interference terms appear, namely $\langle L_z S_z \rangle \neq 0$ and $\langle L_x S_x \rangle \neq 0$, together with a clear anisotropy between the x/y-axis and z-axis, namely $\langle \hat{A}_x \hat{B}_x \rangle \neq \langle \hat{A}_z \hat{B}_z \rangle$ for $\hat{A}, \hat{B} \in [\hat{M}, \hat{L}, \hat{S}]$. The profound atomic-like features get mediated by the lattice degrees of freedom as we move towards the metallic regime. Most importantly, the orbital part of the response remains rather large in magnitude and thus contributes significantly to the total magnetic response.

4.2.4 Summary and conclusions

To summarize, we have investigated the t_{2g} Hamiltonian in the presence of tetragonal crystal-field (m-CF) or spin-orbit coupling (m-SO) on the one- and two-particle level. Regarding the local spectral functions we have found only subtle differences. In contrast, the conserved-symmetries and the (unique) orbital-character of those systems can be easily resolved when considering their response upon small fields, and we have observed profound atomic features even in the case where we enter the strongly correlated regime. Considering both operators on equal footing (m-CFSO), the characteristics of both operators come into view: easy and hard axis magnetic anisotropy together with interference $\hat{L}\hat{S}$ terms are

[8] In the RPA limit, χ_{ls} (shown in insets), is only marginally present (shown in insets): only one point at the Fermi surface contributes to the ring-diagram evaluation.

present. Interestingly, we find that the orbital-orbital channel contributes significantly in all cases: the orbital moment is not fully quenched.

Chapter 5

Dynamics of the PAM's magnetic response

Heavy-fermion systems – (intermetallic) compounds of rare earth metals – comprise an extended class of strongly correlated compounds which have been in the forefront of intense experimental and theoretical research for over 50 years [125, 117, 141]. The physics of those materials originates from the interplay of the Kondo effect [71] that when activated leads to a abrupt resistivity reduction, and the indirect – mediated by the polarization of the dispersive conduction electrons – coupling of the localized states, the so-called RKKY interaction [113], that favors the formation of magnetic ground states [106]. However, a realistic description of such compounds within an *ab initio* framework is a very challenging (numerical) task. Multiple energy scales, i.e. crystal-field splittings and spin-orbit coupling, coexist and have to be considered explicitly while taking into account correlation effects; a task that is oftentimes feasible only within crude approximation schemes, even when equipped with the concurrent advanced computational methodologies.

In the following, we report our DMFT study on the multi-orbital generalization of the periodic Anderson model, as inspired by conditions that are realized in Cerium-based heavy-fermion compounds. The remainder of this chapter is organized as follows. In Section 5.1, we explicitly present the parametrization of the models that have been used together with

the methodology that we have followed. In Section 5.2 we discuss the evolution of the single-particle spectral functions of our systems. Finally, in Section 5.3, we present our results regarding the static- and the dynamic magnetic susceptibilities, both in real-frequency and time.

5.1 Models and methodology

In this study, we consider the multi-orbital generalization of the periodic Anderson model (PAM). Our model consists of four localized states that hybridize with four conduction bands, on a three-dimensional cubic lattice. The PAM Hamiltonian, written in a mixed Wannier and Block representation, formally reads as,

$$\begin{aligned}\hat{H}_{\mathrm{PAM}} = &\sum_{\mathbf{k}b} \epsilon_b(\mathbf{k}) c^\dagger_{\mathbf{k}b} c_{\mathbf{k}b} + \sum_{i\alpha\beta} h_{\alpha\beta} f^\dagger_{i\alpha} f_{i\beta} \\ &+ \sum_{ib\alpha} V_{b\alpha}\left(c^\dagger_{ib} f_{i\alpha} + f^\dagger_{i\alpha} c_{ib} \right) \\ &+ \sum_{i} \sum_{\alpha\beta\gamma\delta} U_{\alpha\beta\gamma\delta} f^\dagger_{i\alpha} f^\dagger_{i\beta} f_{i\gamma} f_{i\delta} \\ &+ \mu(\hat{N}_c + \hat{N}_f).\end{aligned} \tag{5.1}$$

Here, $c^\dagger_{ib}$ (c_{ib}) create (destroy) an electron in the b conduction band whereas $f_{i\alpha}$ ($f_{i\alpha}$) denote the creation (annihilation) of an electron with quantum number α at site i. The matrix elements $h_{\alpha\beta}$ stand for the single-particle local structure and $U_{\alpha\beta\gamma\delta}$ is the 4-index interaction kernel acting only on the localized states; $V_{b\alpha}$ correspond to the hybridization strength between the local f-states and the conduction bands. Finally, the chemical potential, μ, controls the total particle occupation of the system.

The dispersion relation, $\varepsilon_b(\boldsymbol{k})$, is assumed fully isotropic and equivalent for all conduction bands, namely $\varepsilon_b(\mathbf{k}) = 2t(\cos k_x + \cos k_y + \cos k_z)$. The localized f-states are expressed in the basis of total angular momentum $|J; J_z\rangle$, and more specifically the $|J = \frac{5}{2}; J_z = \pm\frac{5}{2}\rangle$ and $|J = \frac{5}{2}; J_z = \pm\frac{3}{2}\rangle$ states. We assume the single-particle local structure to be diagonal albeit we control the splitting between the j-states with a unique adjustable parameter

$\Delta_j = E_{5/2} - E_{3/2}$. The hybridization is set to be constant, $V_{b\alpha} = V$, and for all cases shown above we fix the total particle filling to be $N = N_c + N_f = 3$ with the additional restriction $N_f = 1$.

We obtain the solution of the PAMs by means of dynamical mean-field theory (DMFT) in which the original lattice model is mapped onto an impurity embedded in a non-interacting fermionic bath self-consistently[1]. Within the DMFT context, we are assured that we take into account all local correlation effects explicitly. To solve the generated auxiliary impurity problems, lying in the core of the DMFT framework, we employ the – numerically exact – continuous-time Quantum Monte Carlo (CT-QMC) [46], in its hybridization expansion variant (CT-HYB) [116].

In all cases, the converged impurity models have been subsequently sampled 50 times with high QMC statistics to achieve quality results for both the corresponding local self-energy, $\Sigma(i\omega_n)$, and the dynamic (impurity) magnetic response along the z-axis, $\chi^{imp}_{zz}(\tau)$. The calculation of $\chi^{imp}_{zz}(\tau) = \langle M_z(\tau) M_z(\tau = 0)\rangle$ has been performed within the time-insertion method on the basis of Legendre polynomials for higher accuracy [21]. The obtained fermionic single-particle Green's functions and bosonic dynamic responses have been analytically continued onto the real-frequency axis using the stochastic optimization method (SOM) [76].

5.2 Results: Single particle spectral functions

We start our discussion from the single-particle local spectral functions, $A(\omega)$, shown in Fig 5.1 for three different inverse temperatures. Row-wise the splitting of the j-states remains fixed and only free parameter is the strength their hybridization with the non-interacting bath, which increasing when moving from the left to the right. The upper (lower) panels correspond to the $\Delta_j = -0.05\ eV$ ($\Delta_j = +0.05\ eV$)), namely to the case where the lowest lying states are the $|J = \frac{5}{2}; J_z = \pm\frac{5}{2}\rangle$ ($|J = \frac{5}{2}; J_z = \pm\frac{3}{2}\rangle$). The central panel

[1] See also Chapter 1

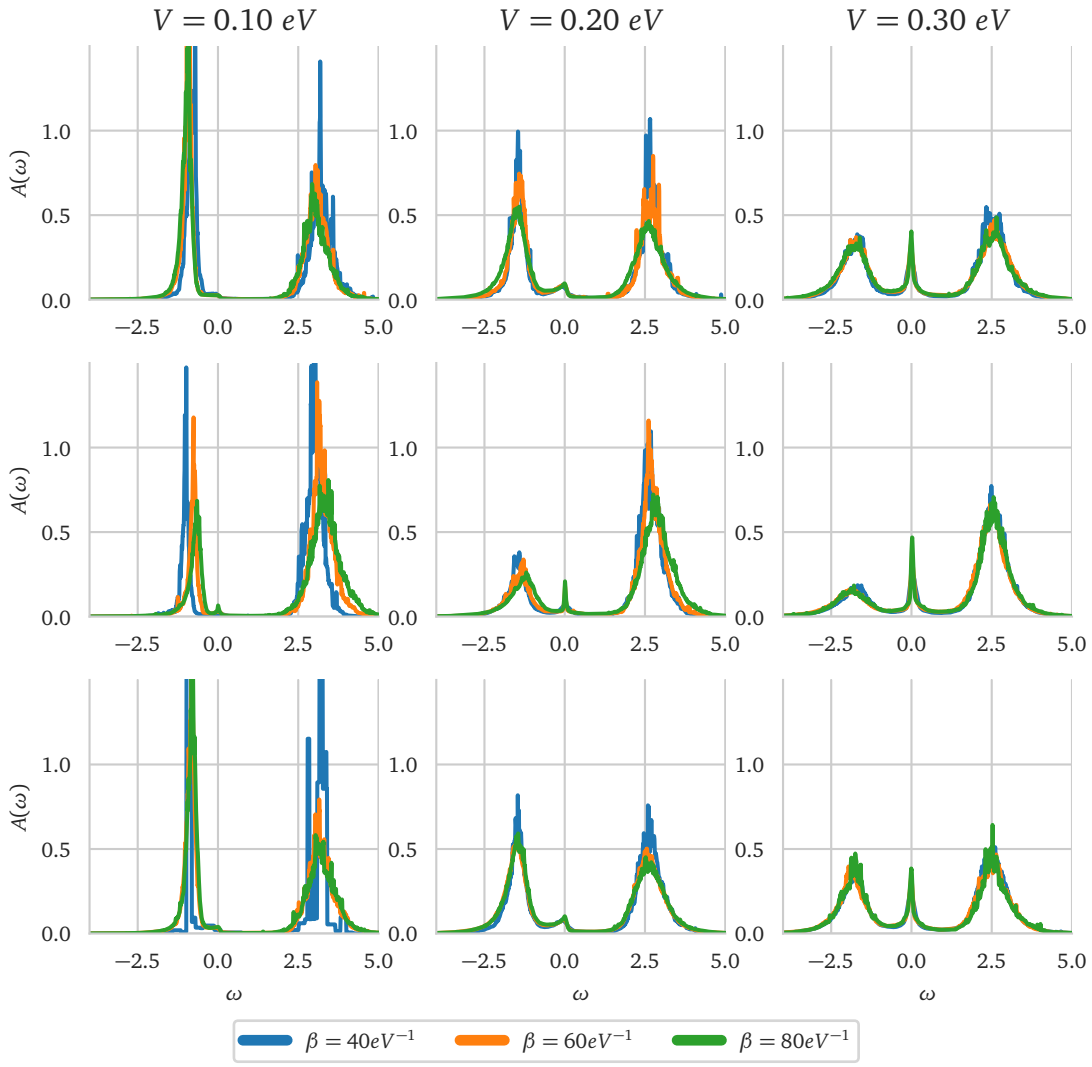

Fig. 5.1: The single-particle local spectral-functions, as a function of temperature, for all studied models. Row-wise the splitting is adjusted to $\Delta_J = -0.05\ eV$ (upper), $\Delta_J = 0.0\ eV$ (middle) and $\Delta_J = +0.05\ eV$ (lower).

correspond to full fourfold degeneracy, $\Delta_j = 0.00\ eV$.

As expected, and regardless of the assumed splitting of the j-states, the hybridization controls the transition from an insulating (purely localized) solution to a metallic-like one. For small hybridization, the local subspace is effectively decoupled from the band, while spectral weight moves towards the Fermi level and becomes coherent with increasing hy-

bridization. In turn, the quasiparticle peak is dominated by the corresponding lowest-in-energy states, although this information cannot be directly resolved from inspection of the full spectral functions. The character of the (composite) orbital character is encoded solely in the two-particle interaction kernel. Since we restrict the filling of the corresponding localized states to $N_f = 1$, the two-particle configuration subspace inserts only marginally for all single-particle observables, as is the local spectral function. However, the evolution of the quasiparticle-peak into a Kondo resonance, already signalizes the importance of electronic correlations in the dynamics of the system, which is the subject of the next section.

5.3 Results: Magnetic response functions

5.3.1 Static magnetic response

In Fig 5.2, we present the big summary of the (impurity) static-limit of the magnetic response along the z-axis, $\chi_{mm}(i\omega = 0)$, obtained by DMFT as a function of the temperature from $T = 400\ K$ down to $T = 100\ K$. In all cases, the inverse magnetic response shows an apparent linear Curie-Weiss like behavior: localized j-moments are formed. Even more interesting, however, is the information that we communicate in the color-encoding of our data (red = large, blue = small) – see also Fig. 5.3 – which provides a *measure*, M_d, of the dynamics of the corresponding magnetic response and has been calculated as,

$$M_d = \chi^{\mathrm{imp}}_{mm}(\tau = 0) - \chi^{\mathrm{imp}}_{mm}(\tau = \frac{\beta}{2}). \tag{5.2}$$

At high temperatures and small-to-intermediate hybridizations, the response of the system is rather non-dynamic. As temperature decreases fluctuations start to show up and especially for the intermediate values of the hybridization become significant. In contrast, for large hybridizations the strong dynamic behavior is always present. This behavior holds for all studied systems, although the numerical values suggest that there is a dependency with respect to the assumed splitting: the fourfold degenerate model shows the most dynamic features, since fluctuations within the local-subspace are not penalized.

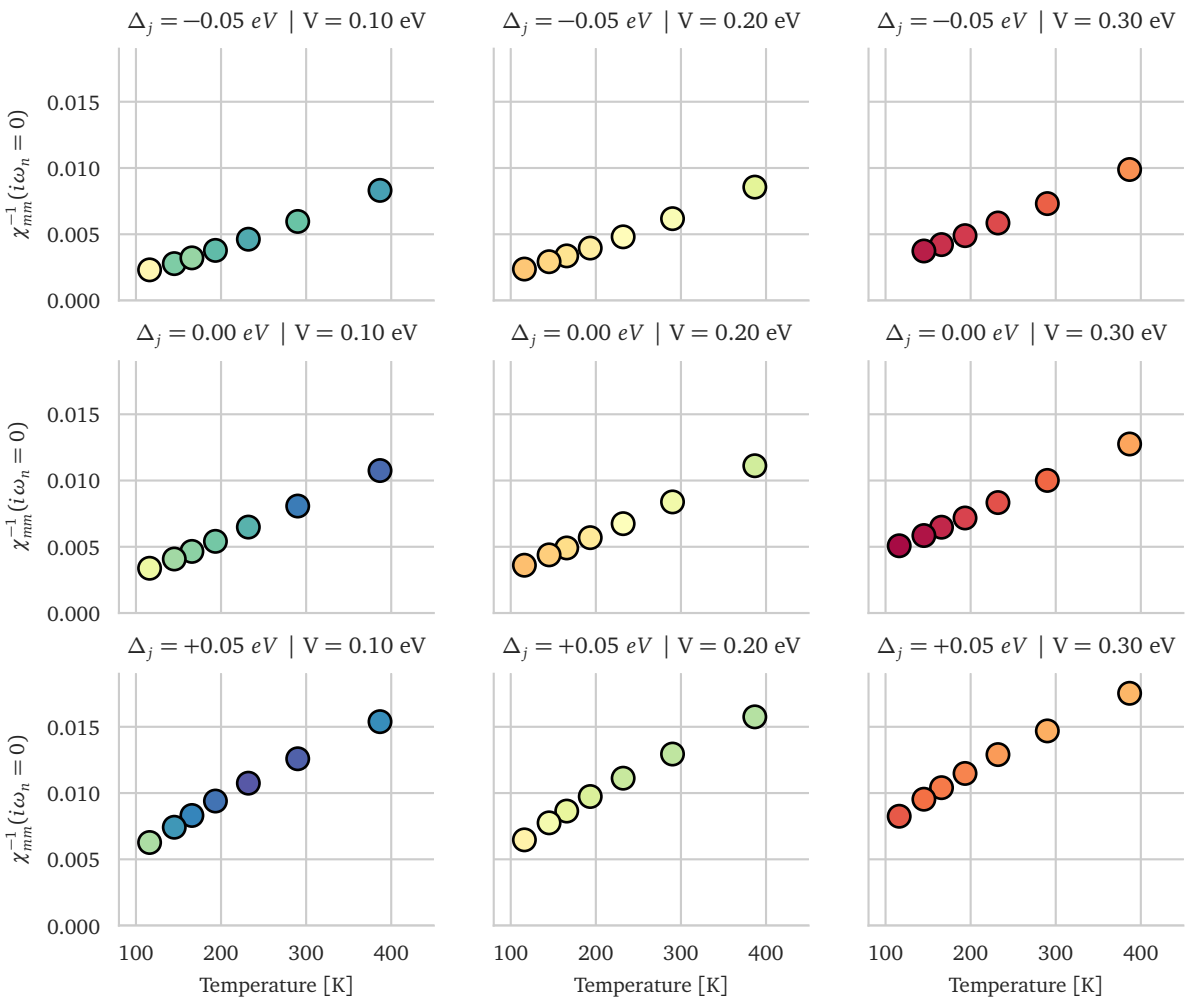

Fig. 5.2: The static magnetic response as a function of temperature, for all studied models. Row-wise the splitting is adjusted to $\Delta_J = -0.05\ eV$ (upper), $\Delta_J = 0.0\ eV$ (middle) and $\Delta_J = +0.05\ eV$ (lower). From left to right the hybridization strength increases as $V = 0.1\ eV$ (left), $V = 0.2\ eV$ (center) and $V = 0.3\ eV$ (right). Red (blue) color encodes a large (small) magnetitude of the measure M_d.

Importantly, our results suggest that employing purely local-models to fit magnetic responses that show even Curie-Weiss behavior, shall be considered with great care in most cases: albeit there can be found a parametrization that perfectly fits the data, the assumed moment is definitely not static.

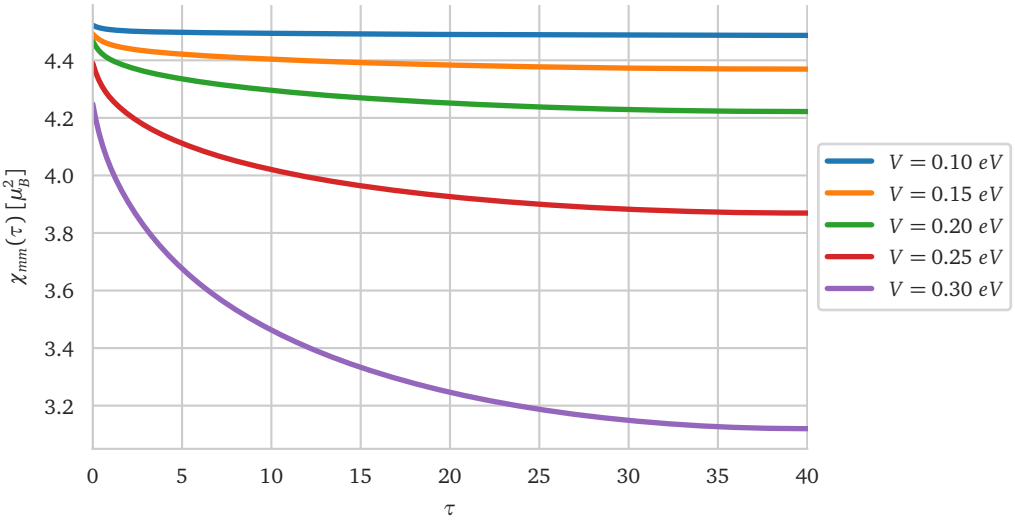

Fig. 5.3: An example case of the magnetic (impurity) response function on the imaginary time axis, at fixed inverse temperature $\beta = 80\ eV^{-1}$ and local splitting $\Delta_J = -0.05\ eV$, and varying hybridization strength V.

5.3.2 Dynamic magnetic response: Frequency- and time-domain

In continuation of the previous analysis, in Fig. 5.4 and Fig. 5.5, we show the spectral functions of magnetic response in real-frequencies, $\chi_{mm}(\omega)$, and real-time, $\chi_{mm}(t)$, respectively, for all studied models as obtained by the analytical continuation of the corresponding measured $\chi_{mm}(i\omega_n)$. Despite the fact that our data on the Matsubara axis are of great quality (see Fig. 5.3 for example), in order to Fourier transform into the time-domain, $\chi_{mm}(t) \equiv \mathrm{FT}[\chi_{\mathrm{mm}}(\omega)]$, the real-frequency magnetic spectral functions have been fitted within an adjustable Lorentzian distribution of the form,

$$\frac{1}{\pi}\mathrm{Im}\chi_{mm}(\omega) \rightarrow L(\omega) = \frac{2\alpha\gamma\omega}{(\omega^2 - \omega_p^2)^2 + 4\gamma^2\omega^2}, \tag{5.3}$$

where ω_p stands for the peak-position and γ is the damping parameter (width of the Lorentzian). In all cases, the numerical optimization has been performed by minimizing the quadratic difference between the actual and the fitted spectral functions, with an optimization confidence on the fifth digit.

For small hybridization strength, most of the bosonic spectral weight is located very close to

the zero-level and shows a characteristic peak structure, which corresponds to very shallow and extensive time-period fluctuations that decay very slowly: here the moments can be considered static and thus a purely-local model can provide reasonable estimates. As we increase the hybridization strength, the spectral weight moves towards higher frequencies and becomes dispersive; there, the time-fluctuations are very strong and sharp, and the responses decay in short time-scales: neglecting the hybridization with the conduction electrons can lead to false estimates.

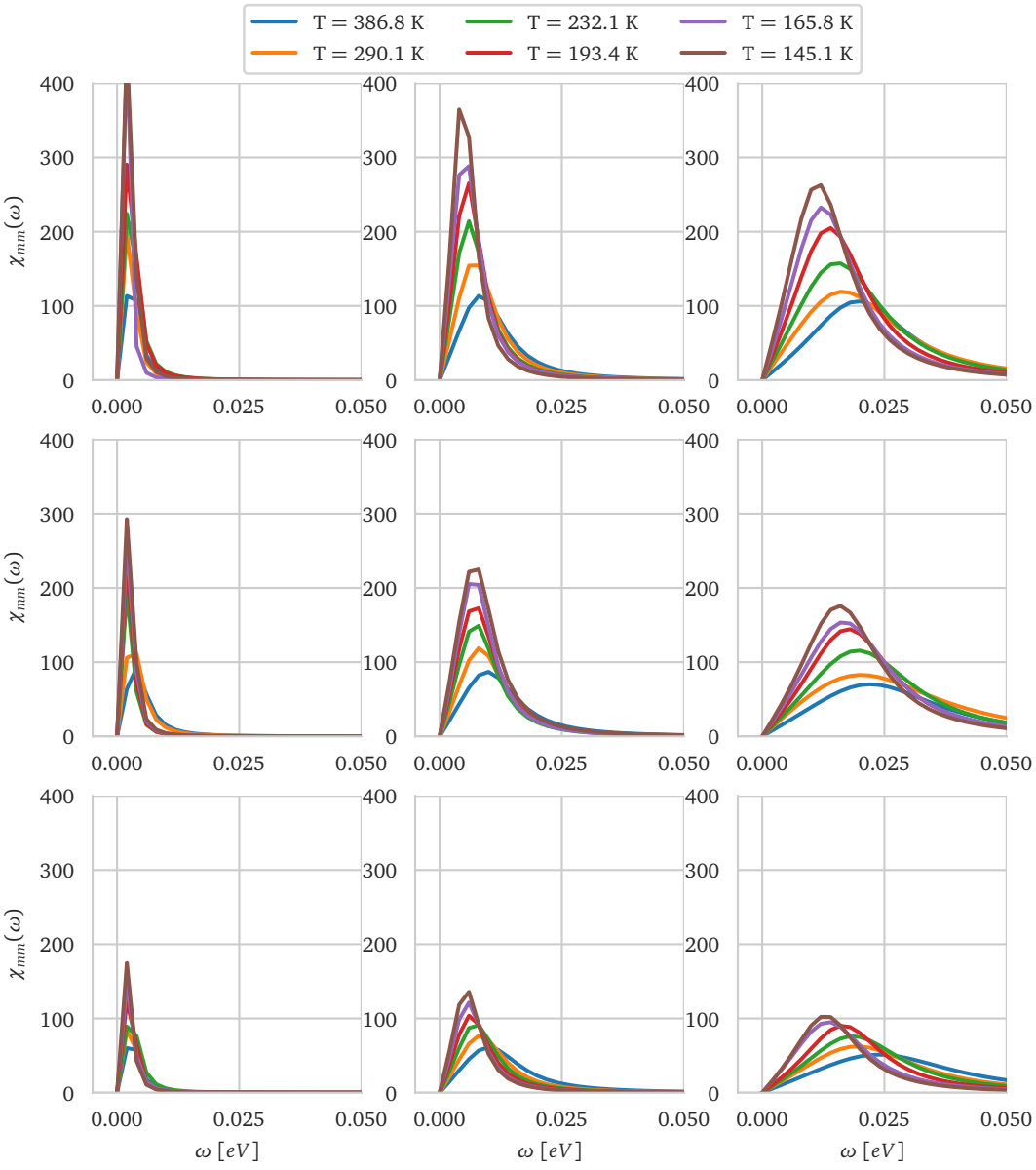

Fig. 5.4: The magnetic response in the real frequency domain as a function of temperature, for all studied models. Row-wise the splitting is adjusted to $\Delta_J = -0.05\ eV$ (upper), $\Delta_J = 0.0\ eV$ (middle) and $\Delta_J = +0.05\ eV$ (lower). From left to right the hybridization strength increases as $V = 0.1\ eV$ (left), $V = 0.2\ eV$ (center) and $V = 0.3\ eV$ (right).

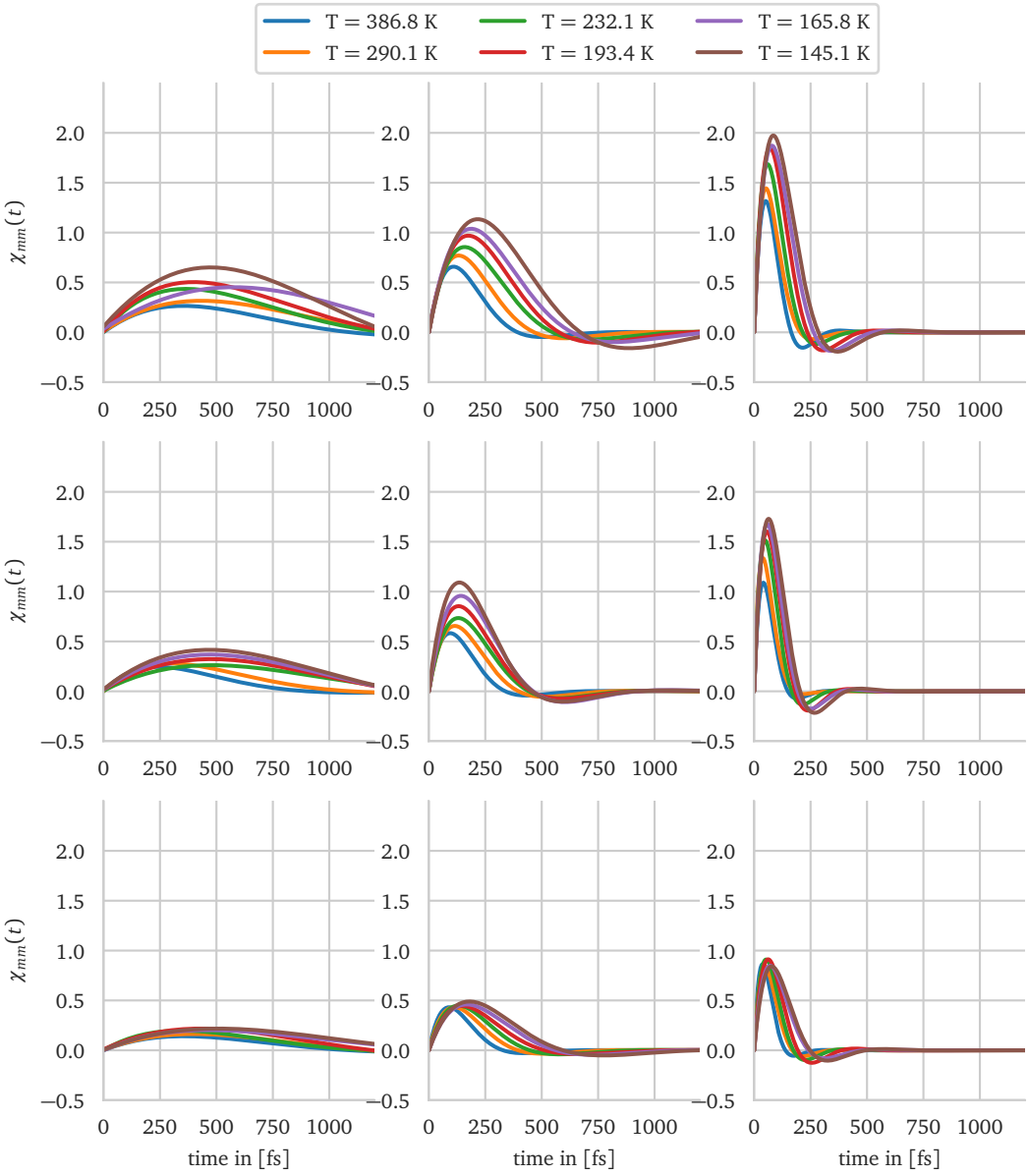

Fig. 5.5: The magnetic response in the real time domain as a function of temperature, for all studied models. Row-wise the splitting is adjusted to $\Delta_J = -0.05\ eV$ (upper), $\Delta_J = 0.0\ eV$ (middle) and $\Delta_J = +0.05\ eV$ (lower). From left to right the hybridization strength increases as $V = 0.1\ eV$ (left), $V = 0.2\ eV$ (center) and $V = 0.3\ eV$ (right).

Chapter 6

Summary

The topic of this thesis has been the study of material-based many-body effective Hamiltonians describing different classes of compounds, within the context of dynamical mean-field theory (DMFT) and the *ab initio* framework of density functional theory (DFT). Exact in the limit of infinite dimensions and formulated around the single-particle self-energy, DMFT not only allows for accessing dynamic one-particle or two-particle correlator but acts like a compass for the development of concurrent methodologies that target self-consistency to higher-in-order properties. The latter, provides the necessary material specification to tailor the parametrization of the corresponding effective models.

Starting with the nickelate-based heterostructure $LaNiO_2/LaGaO_3$ (Chapter 3), we have investigated the structure of the orbital-resolved single-particle spectral functions at nominal filling and upon electron and hole doping. The analysis of the layer dependence to the concentration of the induced charge carriers and the accompanied redistribution of the spectral weight of Nickel, Oxygen and Lanthanum states around the Fermi surface, serves as a prediction for the corresponding compound, yet to be verified by experiments. Within the same, DFT+DMFT, framework, we have tackled Ca_2RuO_4 ruthenates' compound, which has recently attracted attention due to an unusual interplay of correlation effects and spin-orbit coupling (Chapter 4). Our simulations have explained a new – experimentally generated – type of insulator-to-metal transition caused by subtle variations in the lattice structure as

induced by the application of an external electrical potential.

In continuation to the material-based studies, we have turned our attention to prototypical model Hamiltonians. First, we have studied the a generic three-band t_{2g} model in the presence of both tetragonal crystal-field and spin-orbit coupling – a reminiscent of the Ca_2RuO_4 compound. Here, the simulations have targeted not only single-particle spectral functions but more importantly the channel resolved – orbital-orbital, spin-spin and spin-orbital – static and uniform magnetic susceptibilities for different parametrizations of the Coulomb interaction across the phase-diagram, using for reference the extreme cases: atomic-limit and the spin-resolved random-phase approximation in the weak coupling regime. Our results sketch the significance of the two-particle susceptibilities to explicitly recover the presence of each corresponding symmetry of the applied local operator. Following the last remark and inspired by previous studies on the family of Ce-based heavy-fermion systems, we have explored in depth the dynamic character of the magnetic susceptibility of the 4-state Periodic Anderson model (PAM) in a wide range of parameters' space (Chapter 5). We have determined the boundaries of the validity of a common scheme, where one can map the underlying PAM onto a static isolated local subspace. However, for a wide range of the phase-space, we find highly fluctuating moments suggesting that the neglection of the hybridization can indeed lead to physically wrong estimates.

Bibliography

[1] Anatole 1914-2011 (viaf)79042222 Abragam and Brebis 1915-2006 (viaf)19738318 Bleaney. *Electron paramagnetic resonance of transition ions*. Oxford : Clarendon press, 1970. ISBN: 0198512503. URL: http://lib.ugent.be/catalog/rug01:000477992.

[2] Alexander Altland and Ben D Simons. *Condensed matter field theory*. Cambridge university press, 2010.

[3] Michaela Altmeyer et al. "Role of vertex corrections in the matrix formulation of the random phase approximation for the multiorbital Hubbard model". In: *Physical Review B* 94.21 (2016), p. 214515.

[4] OK Andersen and T Saha-Dasgupta. "Muffin-tin orbitals of arbitrary order". In: *Physical Review B* 62.24 (2000), R16219.

[5] Philip Warren Anderson. "Localized magnetic states in metals". In: *Physical Review* 124.1 (1961), p. 41.

[6] PW Anderson and Elihu Abrahams. "Superconductivity theories narrow down". In: *Nature* 327.6121 (1987), p. 363.

[7] Stefan Andersson and Myrta Grüning. "Performance of Density Functionals for Calculating Barrier Heights of Chemical Reactions Relevant to Astrophysics". In: *The Journal of Physical Chemistry A* 108.37 (2004), pp. 7621–7636. DOI: 10.1021/jp040448c. eprint: https://doi.org/10.1021/jp040448c. URL: https://doi.org/10.1021/jp040448c.

[8] V. I. Anisimov, D. Bukhvalov, and T. M. Rice. "Electronic structure of possible nickelate analogs to the cuprates". In: *Phys. Rev. B* 59 (12 Mar. 1999), pp. 7901–7906. DOI: 10.1103/PhysRevB.59.7901. URL: https://link.aps.org/doi/10.1103/PhysRevB.59.7901.

[9] Vladimir I. Anisimov, Jan Zaanen, and Ole K. Andersen. "Band theory and Mott insulators: Hubbard U instead of Stoner I". In: *Phys. Rev. B* 44 (3 July 1991), pp. 943–954. DOI: 10.1103/PhysRevB.44.943. URL: https://link.aps.org/doi/10.1103/PhysRevB.44.943.

[10] Vladimir I Anisimov, Jan Zaanen, and Ole K Andersen. "Band theory and Mott insulators: Hubbard U instead of Stoner I". In: *Physical Review B* 44.3 (1991), p. 943.

[11] F Aryasetiawan et al. "Calculations of Hubbard U from first-principles". In: *Physical Review B* 74.12 (2006), p. 125106.

[12] Thomas Ayral, Silke Biermann, and Philipp Werner. "Screening and nonlocal correlations in the extended Hubbard model from self-consistent combined G W and dynamical mean field theory". In: *Physical Review B* 87.12 (2013), p. 125149.

[13] Thomas Ayral and Olivier Parcollet. "Mott physics and spin fluctuations: A unified framework". In: *Physical Review B* 92.11 (2015), p. 115109.

[14] CJ Ballhausen. "Crystal and ligand field theory". In: *International Journal of Quantum Chemistry* 5.S5 (1971), pp. 373–377.

[15] Ulf von Barth and Lars Hedin. "A local exchange-correlation potential for the spin polarized case. i". In: *Journal of Physics C: Solid State Physics* 5.13 (1972), p. 1629.

[16] Daniel Bauernfeind, Markus Aichhorn, and Hans Gerd Evertz. "Comparison of MPS based real time evolution algorithms for Anderson Impurity Models". In: *arXiv preprint arXiv:1906.09077* (2019).

[17] J. G. Bednorz and K. A. Müller. "Possible high Tc superconductivity in the Ba-La-Cu-O system". In: *Zeitschrift für Physik B Condensed Matter* 64.2 (June 1986), pp. 189–193. ISSN: 1431 - 584X. DOI: 10.1007/BF01303701. URL: https://doi.org/10.1007/BF01303701.

[18] Joel Bertinshaw et al. “Square Lattice Iridates”. In: *Annual Review of Condensed Matter Physics* 10.1 (2019), pp. 315–336. DOI: 10.1146/annurev-conmatphys-031218-013113.

[19] J. Bertinshaw et al. “Unique Crystal Structure of Ca_2RuO_4 in the Current Stabilized Semimetallic State”. In: *Phys. Rev. Lett.* 123 (13 Sept. 2019), p. 137204. DOI: 10.1103/PhysRevLett.123.137204. URL: https://link.aps.org/doi/10.1103/PhysRevLett.123.137204.

[20] Hans Bethe. “Zur theorie der metalle”. In: *Zeitschrift für Physik* 71.3-4 (1931), pp. 205–226.

[21] Lewin Boehnke et al. “Orthogonal polynomial representation of imaginary-time Green’s functions”. In: *Phys. Rev. B* 84 (7 Aug. 2011), p. 075145. DOI: 10.1103/PhysRevB.84.075145. URL: https://link.aps.org/doi/10.1103/PhysRevB.84.075145.

[22] David Bohm and David Pines. “A Collective Description of Electron Interactions. I. Magnetic Interactions”. In: *Phys. Rev.* 82 (5 June 1951), pp. 625–634. DOI: 10.1103/PhysRev.82.625. URL: https://link.aps.org/doi/10.1103/PhysRev.82.625.

[23] Galen Bollinger. *Book Review: Regression Diagnostics: Identifying Influential Data and Sources of Collinearity*. 1981.

[24] Max Born and Robert Oppenheimer. “Zur quantentheorie der molekeln”. In: *Annalen der physik* 389.20 (1927), pp. 457–484.

[25] Heinz-Peter Breuer, Francesco Petruccione, et al. *The theory of open quantum systems*. Oxford University Press on Demand, 2002.

[26] J. P. Carlo et al. “New magnetic phase diagram of (Sr,Ca)2RuO4”. In: *Nature Materials* 11.4 (2012), pp. 323–328. ISSN: 1476-4660. DOI: 10.1038/nmat3236. URL: https://doi.org/10.1038/nmat3236.

[27] M Casula et al. “Low-energy models for correlated materials: bandwidth renormalization from coulombic screening”. In: *Physical review letters* 109.12 (2012), p. 126408.

[28] Dana Cialla-May, Michael Schmitt, and Jürgen Popp. “Theoretical principles of Raman spectroscopy”. In: *Physical Sciences Reviews* 4.6 ().

[29] M. T. Czyzyk and G. A. Sawatzky. “Local-density functional and on-site correlations: The electronic structure of La_2CuO_4 and $LaCuO_3$”. In: *Phys. Rev. B* 49 (20 May 1994), pp. 14211–14228. DOI: 10.1103/PhysRevB.49.14211. URL: https://link.aps.org/doi/10.1103/PhysRevB.49.14211.

[30] Xi Dai, Kristjan Haule, and Gabriel Kotliar. “Strong-coupling solver for the quantum impurity model”. In: *Phys. Rev. B* 72 (4 July 2005), p. 045111. DOI: 10.1103/PhysRevB.72.045111. URL: https://link.aps.org/doi/10.1103/PhysRevB.72.045111.

[31] Andrea Damascelli. “Probing the electronic structure of complex systems by ARPES”. In: *Physica Scripta* 2004.T109 (2004), p. 61.

[32] Nagamalleswararao Dasari et al. “A multi-orbital iterated perturbation theory for model Hamiltonians and real material-specific calculations of correlated systems”. In: *The European Physical Journal B* 89.9 (2016), p. 202.

[33] Z. Fang and K. Terakura. “Magnetic phase diagram of $Ca_{2-x}Sr_xRuO_4$ governed by structural distortions”. In: *Phys. Rev. B* 64 (2 June 2001), p. 020509. DOI: 10.1103/PhysRevB.64.020509. URL: https://link.aps.org/doi/10.1103/PhysRevB.64.020509.

[34] D. Fausti et al. “Light-Induced Superconductivity in a Stripe-Ordered Cuprate”. In: *Science* 331.6014 (2011), pp. 189–191. ISSN: 0036-8075. DOI: 10.1126/science.1197294. eprint: https://science.sciencemag.org/content/331/6014/189.full.pdf. URL: https://science.sciencemag.org/content/331/6014/189.

[35] Alexander L Fetter and John Dirk Walecka. *Quantum theory of many-particle systems*. Courier Corporation, 2012.

[36] WMC Foulkes et al. “Quantum Monte Carlo simulations of solids”. In: *Reviews of Modern Physics* 73.1 (2001), p. 33.

[37] JK Freericks, VM Turkowski, and Veljko Zlatic. “Nonequilibrium dynamical mean-field theory”. In: *Physical review letters* 97.26 (2006), p. 266408.

[38] O. Friedt et al. “Structural and magnetic aspects of the metal-insulator transition in $Ca_{2-x}Sr_xRuO_4$”. In: *Phys. Rev. B* 63 (17 Apr. 2001), p. 174432. DOI: 10.1103/PhysRevB.63.174432. URL: https://link.aps.org/doi/10.1103/PhysRevB.63.174432.

[39] Hidetoshi Fukuyama and Ryogo Kubo. “Interband Effects on Magnetic Susceptibility. II. Diamagnetism of Bismuth”. In: *Journal of the Physical Society of Japan* 28.3 (1970), pp. 570–581. DOI: 10.1143/JPSJ.28.570. eprint: https://doi.org/10.1143/JPSJ.28.570. URL: https://doi.org/10.1143/JPSJ.28.570.

[40] Yuki Fuseya, Masao Ogata, and Hidetoshi Fukuyama. “Transport Properties and Diamagnetism of Dirac Electrons in Bismuth”. In: *Journal of the Physical Society of Japan* 84.1 (2015), p. 012001. DOI: 10.7566/JPSJ.84.012001. eprint: https://doi.org/10.7566/JPSJ.84.012001. URL: https://doi.org/10.7566/JPSJ.84.012001.

[41] Antoine Georges and Gabriel Kotliar. “Hubbard model in infinite dimensions”. In: *Physical Review B* 45.12 (1992), p. 6479.

[42] Antoine Georges et al. “Dynamical mean-field theory of strongly correlated fermion systems and the limit of infinite dimensions”. In: *Rev. Mod. Phys.* 68 (1 Jan. 1996), pp. 13–125. DOI: 10.1103/RevModPhys.68.13. URL: https://link.aps.org/doi/10.1103/RevModPhys.68.13.

[43] Psaltakis C. Gregory. *Quantum Many-Particle Systems*. Crete University Press, Heraklion, 2008.

[44] Claudius Gros and Roser Valenti. “Cluster expansion for the self-energy: A simple many-body method for interpreting the photoemission spectra of correlated Fermi systems”. In: *Physical Review B* 48.1 (1993), p. 418.

[45] Emanuel Gull et al. “Continuous-time Monte Carlo methods for quantum impurity models”. In: *Reviews of Modern Physics* 83.2 (2011), p. 349.

[46] Emanuel Gull et al. “Continuous-time quantum Monte Carlo impurity solvers”. In: *Computer Physics Communications* 182.4 (2011), pp. 1078–1082.

[47] O Gunnarsson, MW Haverkort, and G Sangiovanni. “Analytical continuation of imaginary axis data for optical conductivity”. In: *Physical Review B* 82.16 (2010), p. 165125.

[48] O Gunnarsson et al. “Density-functional calculation of the parameters in the Anderson model: Application to Mn in CdTe”. In: *Physical Review B* 39.3 (1989), p. 1708.

[49] Martin C Gutzwiller. “Effect of correlation on the ferromagnetism of transition metals”. In: *Physical Review Letters* 10.5 (1963), p. 159.

[50] Hartmut Hafermann et al. “Superperturbation solver for quantum impurity models”. In: *EPL (Europhysics Letters)* 85.2 (2009), p. 27007.

[51] M. J. Han et al. “Dynamical Mean-Field Theory of Nickelate Superlattices”. In: *Phys. Rev. Lett.* 107 (20 Nov. 2011), p. 206804. DOI: 10.1103/PhysRevLett.107.206804. URL: https://link.aps.org/doi/10.1103/PhysRevLett.107.206804.

[52] P. Hansmann et al. “Turning a Nickelate Fermi Surface into a Cupratelike One through Heterostructuring”. In: *Phys. Rev. Lett.* 103 (1 June 2009), p. 016401. DOI: 10.1103/PhysRevLett.103.016401. URL: https://link.aps.org/doi/10.1103/PhysRevLett.103.016401.

[53] Walter A Harrison. *Electronic structure and the properties of solids: the physics of the chemical bond*. Courier Corporation, 2012.

[54] M. W. Haverkort, M. Zwierzycki, and O. K. Andersen. “Multiplet ligand-field theory using Wannier orbitals”. In: *Phys. Rev. B* 85 (16 Apr. 2012), p. 165113. DOI: 10.1103/PhysRevB.85.165113. URL: https://link.aps.org/doi/10.1103/PhysRevB.85.165113.

[55] K Held. “Electronic structure calculations using dynamical mean field theory”. In: *Advances in physics* 56.6 (2007), pp. 829–926.

[56] MH Hettler et al. “Dynamical cluster approximation: Nonlocal dynamics of correlated electron systems”. In: *Physical Review B* 61.19 (2000), p. 12739.

[57] Alexander Cyril Hewson. *The Kondo problem to heavy fermions*. Vol. 2. Cambridge university press, 1997.

[58] Vandana S. Hiteshi T. Tanmoy C. "A Brief Review on Importance of DFT In Drug Design". In: *Res. Med. Eng. Sci.* 7 (2019). DOI: 10.31031/RMES.2019.07.0006.

[59] P. Hohenberg and W. Kohn. "Inhomogeneous Electron Gas". In: *Phys. Rev.* 136 (3B Nov. 1964), B864–B871. DOI: 10.1103/PhysRev.136.B864. URL: https://link.aps.org/doi/10.1103/PhysRev.136.B864.

[60] John Hubbard. "Electron correlations in narrow energy bands". In: *Proceedings of the Royal Society of London. Series A. Mathematical and Physical Sciences* 276.1365 (1963), pp. 238–257.

[61] Mark Jarrell and James E Gubernatis. "Bayesian inference and the analytic continuation of imaginary-time quantum Monte Carlo data". In: *Physics Reports* 269.3 (1996), pp. 133–195.

[62] R. O. Jones. "Density functional theory: Its origins, rise to prominence, and future". In: *Rev. Mod. Phys.* 87 (3 Aug. 2015), pp. 897–923. DOI: 10.1103/RevModPhys.87.897. URL: https://link.aps.org/doi/10.1103/RevModPhys.87.897.

[63] Christoph Jung et al. "Superperturbation theory on the real axis". In: *Annalen der Physik* 523.8-9 (2011), pp. 706–714.

[64] Junjiro Kanamori. "Electron Correlation and Ferromagnetism of Transition Metals". In: *Progress of Theoretical Physics* 30.3 (Sept. 1963), pp. 275–289. ISSN: 0033-068X. DOI: 10.1143/PTP.30.275. eprint: http://oup.prod.sis.lan/ptp/article-pdf/30/3/275/5278869/30-3-275.pdf. URL: https://doi.org/10.1143/PTP.30.275.

[65] Junjiro Kanamori. "Electron correlation and ferromagnetism of transition metals". In: *Progress of Theoretical Physics* 30.3 (1963), pp. 275–289.

[66] B. Keimer et al. "From quantum matter to high-temperature superconductivity in copper oxides". In: *Nature* 518.7538 (2015), pp. 179–186. ISSN: 1476-4687. DOI: 10.1038/nature14165. URL: https://doi.org/10.1038/nature14165.

[67] Minjae Kim et al. “Spin-Orbit Coupling and Electronic Correlations in Sr_2RuO_4”. In: *Phys. Rev. Lett.* 120 (12 Mar. 2018), p. 126401. DOI: 10.1103/PhysRevLett.120.126401. URL: https://link.aps.org/doi/10.1103/PhysRevLett.120.126401.

[68] Donald H Kobe. “Linked Cluster Theorem and the Green’s Function Equations of Motion for a Many-Fermion System”. In: *Journal of Mathematical Physics* 7.10 (1966), pp. 1806–1820.

[69] W. Kohn. “Nobel Lecture: Electronic structure of matter—wave functions and density functionals”. In: *Rev. Mod. Phys.* 71 (5 Oct. 1999), pp. 1253–1266. DOI: 10.1103/RevModPhys.71.1253. URL: https://link.aps.org/doi/10.1103/RevModPhys.71.1253.

[70] W. Kohn and L. J. Sham. “Self-Consistent Equations Including Exchange and Correlation Effects”. In: *Phys. Rev.* 140 (4A Nov. 1965), A1133–A1138. DOI: 10.1103/PhysRev.140.A1133. URL: https://link.aps.org/doi/10.1103/PhysRev.140.A1133.

[71] Jun Kondo. “Resistance Minimum in Dilute Magnetic Alloys”. In: *Progress of Theoretical Physics* 32.1 (July 1964), pp. 37–49. ISSN: 0033-068X. DOI: 10.1143/PTP.32.37. eprint: http://oup.prod.sis.lan/ptp/article-pdf/32/1/37/5193092/32-1-37.pdf. URL: https://doi.org/10.1143/PTP.32.37.

[72] Gabriel Kotliar et al. “Cellular dynamical mean field approach to strongly correlated systems”. In: *Physical review letters* 87.18 (2001), p. 186401.

[73] Gabriel Kotliar et al. “Electronic structure calculations with dynamical mean-field theory”. In: *Reviews of Modern Physics* 78.3 (2006), p. 865.

[74] Gernot J. Kraberger et al. “Maximum entropy formalism for the analytic continuation of matrix-valued Green’s functions”. In: *Phys. Rev. B* 96 (15 Oct. 2017), p. 155128. DOI: 10.1103/PhysRevB.96.155128. URL: https://link.aps.org/doi/10.1103/PhysRevB.96.155128.

[75] G. Kresse and J. Hafner. “Ab initio molecular dynamics for liquid metals”. In: *Phys. Rev. B* 47 (1 Jan. 1993), pp. 558–561. DOI: 10.1103/PhysRevB.47.558. URL: https://link.aps.org/doi/10.1103/PhysRevB.47.558.

[76] Igor Krivenko and Malte Harland. “SOM: Implementation of the Stochastic Optimization Method for Analytic Continuation”. In: *arXiv preprint arXiv:1808.00603* (2018).

[77] IS Krivenko et al. “Analytical approximation for single-impurity Anderson model”. In: *JETP letters* 91.6 (2010), pp. 319–325.

[78] Rep Kubo. “The fluctuation-dissipation theorem”. In: *Reports on progress in physics* 29.1 (1966), p. 255.

[79] Lev Davidovich Landau. “On the theory of a Fermi Liquid”. In: *JETP* 3 (1959), pp. 920–925.

[80] Frank Lechermann et al. “Rotationally invariant slave-boson formalism and momentum dependence of the quasiparticle weight”. In: *Physical Review B* 76.15 (2007), p. 155102.

[81] K.-W. Lee and W. E. Pickett. “Infinite-layer $LaNiO_2$: Ni^{1+} is not Cu^{2+}”. In: *Phys. Rev. B* 70 (16 Oct. 2004), p. 165109. DOI: 10.1103/PhysRevB.70.165109. URL: https://link.aps.org/doi/10.1103/PhysRevB.70.165109.

[82] Danfeng Li et al. “Superconductivity in an infinite-layer nickelate”. In: *Nature* 572.7771 (2019), pp. 624–627. ISSN: 1476-4687. DOI: 10.1038/s41586-019-1496-5. URL: https://doi.org/10.1038/s41586-019-1496-5.

[83] AI Lichtenstein and MI Katsnelson. “Ab initio calculations of quasiparticle band structure in correlated systems: LDA++ approach”. In: *Physical Review B* 57.12 (1998), p. 6884.

[84] AI Lichtenstein and MI Katsnelson. “Antiferromagnetism and d-wave superconductivity in cuprates: A cluster dynamical mean-field theory”. In: *Physical Review B* 62.14 (2000), R9283.

[85] A. I. Liechtenstein, V. I. Anisimov, and J. Zaanen. “Density-functional theory and strong interactions: Orbital ordering in Mott-Hubbard insulators”. In: *Phys. Rev. B* 52 (8 Aug. 1995), R5467–R5470. DOI: 10.1103/PhysRevB.52.R5467. URL: https://link.aps.org/doi/10.1103/PhysRevB.52.R5467.

[86] Ying Liu and Zhi-Qiang Mao. “Unconventional superconductivity in Sr2RuO4”. In: *Physica C: Superconductivity and its Applications* 514 (2015), pp. 339–353. ISSN: 0921-4534. DOI: https://doi.org/10.1016/j.physc.2015.02.039. URL: http://www.sciencedirect.com/science/article/pii/S0921453415000660.

[87] Yi Lu and Maurits W Haverkort. “Exact diagonalization as an impurity solver in dynamical mean field theory”. In: *The European Physical Journal Special Topics* 226.11 (2017), pp. 2549–2564.

[88] J. Luitz. “WIEN2k, An Augmented Plane Wave + Local Orbitals Program for Calculating Crystal Properties”. In: (2001).

[89] Yoshiteru Maeno, T Maurice Rice, and Manfied Sigrist. “The intriguing superconductivity of strontium ruthenate”. In: (2001).

[90] Y. Maeno et al. “Superconductivity in a layered perovskite without copper”. In: *Nature* 372.6506 (1994), pp. 532–534. ISSN: 1476-4687. DOI: 10.1038/372532a0. URL: https://doi.org/10.1038/372532a0.

[91] Thomas Maier et al. “Quantum cluster theories”. In: *Reviews of Modern Physics* 77.3 (2005), p. 1027.

[92] Ferdinando Mancini, Evgeny Plekhanov, and Gerardo Sica. “Exact solution of the 1D Hubbard model with NN and NNN interactions in the narrow-band limit”. In: *The European Physical Journal B* 86.10 (2013), p. 408.

[93] Ramesh G. Mani et al. “Zero-resistance states induced by electromagnetic-wave excitation in GaAs/AlGaAs heterostructures”. In: *Nature* 420.6916 (2002), pp. 646–650. ISSN: 1476-4687. DOI: 10.1038/nature01277. URL: https://doi.org/10.1038/nature01277.

[94] Richard M. Martin, Lucia Reining, and David M. Ceperley. *Interacting Electrons: Theory and Computational Approaches*. Cambridge University Press, 2016, pp. 345–388.

[95] Nicola Marzari et al. “Maximally localized Wannier functions: Theory and applications”. In: *Rev. Mod. Phys.* 84 (4 Oct. 2012), pp. 1419–1475. DOI: 10.1103/RevModPhys.84.1419. URL: https://link.aps.org/doi/10.1103/RevModPhys.84.1419.

[96] Walter Metzner. “Linked-cluster expansion around the atomic limit of the Hubbard model”. In: *Phys. Rev. B* 43 (10 Apr. 1991), pp. 8549–8563. DOI: 10.1103/PhysRevB.43.8549. URL: https://link.aps.org/doi/10.1103/PhysRevB.43.8549.

[97] Walter Metzner and Dieter Vollhardt. “Correlated lattice fermions in $d \rightarrow \infty$ dimensions”. In: *Physical review letters* 62.3 (1989), p. 324.

[98] Bogdan Mihaila. “Lindhard function of a d-dimensional Fermi gas”. In: (2011). arXiv: 1111.5337 [cond-mat.quant-gas].

[99] Arash A. Mostofi et al. “An updated version of wannier90: A tool for obtaining maximally-localised Wannier functions”. In: *Computer Physics Communications* 185.8 (2014), pp. 2309–2310. ISSN: 0010-4655. DOI: https://doi.org/10.1016/j.cpc.2014.05.003. URL: http://www.sciencedirect.com/science/article/pii/S001046551400157X.

[100] Jernej Mravlje et al. “Coherence-Incoherence Crossover and the Mass-Renormalization Puzzles in Sr_2RuO_4”. In: *Phys. Rev. Lett.* 106 (9 Mar. 2011), p. 096401. DOI: 10.1103/PhysRevLett.106.096401. URL: https://link.aps.org/doi/10.1103/PhysRevLett.106.096401.

[101] Fumihiko Nakamura et al. “Electric-field-induced metal maintained by current of the Mott insulator Ca2RuO4”. In: *Scientific Reports* 3.1 (2013), p. 2536. ISSN: 2045-2322. DOI: 10.1038/srep02536. URL: https://doi.org/10.1038/srep02536.

[102] Fumihiko Nakamura et al. “From Mott insulator to ferromagnetic metal: A pressure study of Ca_2RuO_4”. In: *Phys. Rev. B* 65 (22 May 2002), p. 220402. DOI: 10.1103/PhysRevB.65.220402. URL: https://link.aps.org/doi/10.1103/PhysRevB.65.220402.

[103] S. Nakatsuji and Y. Maeno. "Quasi-Two-Dimensional Mott Transition System $Ca_{2-x}Sr_xRuO_4$". In: *Phys. Rev. Lett.* 84 (12 Mar. 2000), pp. 2666–2669. DOI: 10.1103/PhysRevLett.84.2666. URL: https://link.aps.org/doi/10.1103/PhysRevLett.84.2666.

[104] Canio Noce. "The periodic Anderson model: Symmetry-based results and some exact solutions". In: *Physics reports* 431.4 (2006), pp. 173–230.

[105] Arpita Paul and Turan Birol. "Applications of dft+ dmft in materials science". In: *Annual Review of Materials Research* 49 (2019).

[106] Eva Pavarini, Piers Coleman, and Erik Koch. *Many-Body Physics: From Kondo to Hubbard*. 2015.

[107] E. Pavarini et al. "Band-Structure Trend in Hole-Doped Cuprates and Correlation with T_{cmax}". In: *Phys. Rev. Lett.* 87 (4 July 2001), p. 047003. DOI: 10.1103/PhysRevLett.87.047003. URL: https://link.aps.org/doi/10.1103/PhysRevLett.87.047003.

[108] Perdew, Burke, and Ernzerhof. "Generalized Gradient Approximation Made Simple." In: *Physical review letters* 77 18 (1996), pp. 3865–3868.

[109] Cyril Proust and Louis Taillefer. "The Remarkable Underlying Ground States of Cuprate Superconductors". In: *Annual Review of Condensed Matter Physics* 10.1 (2019), pp. 409–429. DOI: 10.1146/annurev-conmatphys-031218-013210. eprint: https://doi.org/10.1146/annurev-conmatphys-031218-013210. URL: https://doi.org/10.1146/annurev-conmatphys-031218-013210.

[110] Jeffrey G. Rau, Eric Kin-Ho Lee, and Hae-Young Kee. "Spin-Orbit Physics Giving Rise to Novel Phases in Correlated Systems: Iridates and Related Materials". In: *Annual Review of Condensed Matter Physics* 7.1 (2016), pp. 195–221. DOI: 10.1146/annurev-conmatphys-031115-011319.

[111] S. Riccò et al. "In?situ strain tuning of the metal-insulator-transition of Ca2RuO4 in angle-resolved photoemission experiments". In: *Nature Communications* 9.1 (2018), p. 4535. ISSN: 2041-1723. DOI: 10.1038/s41467-018-06945-0. URL: https://doi.org/10.1038/s41467-018-06945-0.

[112] G Rohringer et al. “Diagrammatic routes to nonlocal correlations beyond dynamical mean field theory”. In: *Reviews of Modern Physics* 90.2 (2018), p. 025003.

[113] M. A. Ruderman and C. Kittel. “Indirect Exchange Coupling of Nuclear Magnetic Moments by Conduction Electrons”. In: *Phys. Rev.* 96 (1 Oct. 1954), pp. 99–102. DOI: 10.1103/PhysRev.96.99. URL: https://link.aps.org/doi/10.1103/PhysRev.96.99.

[114] Abida Saleem and S. Hussain. “Review the High Temperature Superconductor (HTSC) Cuprates-Properties and Applications”. In: *Journal of Surfaces and Interfaces of Materials* 1 (Dec. 2013). DOI: 10.1166/jsim.2013.1025.

[115] Ulrich Schollwöck. “The density-matrix renormalization group in the age of matrix product states”. In: *Annals of Physics* 326.1 (2011), pp. 96–192.

[116] Priyanka Seth et al. “TRIQS/CTHYB: A continuous-time quantum Monte Carlo hybridisation expansion solver for quantum impurity problems”. In: *Computer Physics Communications* 200 (2016), pp. 274–284.

[117] Qimiao Si and Frank Steglich. “Heavy Fermions and Quantum Phase Transitions”. In: *Science* 329.5996 (2010), pp. 1161–1166. ISSN: 0036-8075. DOI: 10.1126/science.1191195. eprint: https://science.sciencemag.org/content/329/5996/1161.full.pdf. URL: https://science.sciencemag.org/content/329/5996/1161.

[118] Qimiao Si, Rong Yu, and Elihu Abrahams. “High-temperature superconductivity in iron pnictides and chalcogenides”. In: *Nature Reviews Materials* 1.4 (2016), p. 16017. ISSN: 2058-8437. DOI: 10.1038/natrevmats.2016.17. URL: https://doi.org/10.1038/natrevmats.2016.17.

[119] Richard N Silver, Devinderjit S Sivia, and James E Gubernatis. “Maximum-entropy method for analytic continuation of quantum Monte Carlo data”. In: *Physical Review B* 41.4 (1990), p. 2380.

[120] Jae-Hoon Sim and Myung Joon Han. “Maximum quantum entropy method”. In: *Physical Review B* 98.20 (2018), p. 205102.

[121] Chanchal Sow et al. “Current-induced strong diamagnetism in the Mott insulator Ca2RuO4”. In: *Science* 358.6366 (2017), pp. 1084–1087. ISSN: 0036-8075. DOI: 10.1126/science.aah4297. eprint: https://science.sciencemag.org/content/358/6366/1084.full.pdf. URL: https://science.sciencemag.org/content/358/6366/1084.

[122] Peter Staar, Thomas Maier, and Thomas C Schulthess. “Dynamical cluster approximation with continuous lattice self-energy”. In: *Physical Review B* 88.11 (2013), p. 115101.

[123] Georgios L. Stamokostas and Gregory A. Fiete. “Mixing of $t_{2g} - e_g$ orbitals in 4d and 5d transition metal oxides”. In: *Phys. Rev. B* 97 (8 Feb. 2018), p. 085150. DOI: 10.1103/PhysRevB.97.085150. URL: https://link.aps.org/doi/10.1103/PhysRevB.97.085150.

[124] Uwe Stephan and David A Drabold. “Order-N projection method for first-principles computations of electronic quantities and Wannier functions”. In: *Physical Review B* 57.11 (1998), p. 6391.

[125] G. R. Stewart. “Heavy-fermion systems”. In: *Rev. Mod. Phys.* 56 (4 Oct. 1984), pp. 755–787. DOI: 10.1103/RevModPhys.56.755. URL: https://link.aps.org/doi/10.1103/RevModPhys.56.755.

[126] Edwin M Stoudenmire and Steven R White. “Studying two-dimensional systems with the density matrix renormalization group”. In: *Annu. Rev. Condens. Matter Phys.* 3.1 (2012), pp. 111–128.

[127] Satoru Sugano. *Multiplets of transition-metal ions in crystals*. Elsevier, 2012.

[128] Ping Sun and Gabriel Kotliar. “Many-body approximation scheme beyond GW”. In: *Physical review letters* 92.19 (2004), p. 196402.

[129] D. Sutter et al. “Hallmarks of Hunds coupling in the Mott insulator Ca2RuO4”. In: *Nature Communications* 8.1 (2017), p. 15176. ISSN: 2041-1723. DOI: 10.1038/ncomms15176. URL: https://doi.org/10.1038/ncomms15176.

[130] Kazunori Takada et al. “Superconductivity in two-dimensional CoO2 layers”. In: *Nature* 422.6927 (2003), pp. 53–55. ISSN: 1476-4687. DOI: 10.1038/nature01450. URL: https://doi.org/10.1038/nature01450.

[131] Katsuhik-o Takegahara, Yoshio Aoki, and Akira Yanase. “Slater-Koster tables for f electrons”. In: *Journal of Physics C: Solid State Physics* 13.4 (1980), p. 583.

[132] C Taranto et al. “From infinite to two dimensions through the functional renormalization group”. In: *Physical review letters* 112.19 (2014), p. 196402.

[133] Alessandro Toschi, AA Katanin, and Karsten Held. “Dynamical vertex approximation: A step beyond dynamical mean-field theory”. In: *Physical Review B* 75.4 (2007), p. 045118.

[134] Fabien Tran et al. “Hybrid exchange-correlation energy functionals for strongly correlated electrons: Applications to transition-metal monoxides”. In: *Phys. Rev. B* 74 (15 Oct. 2006), p. 155108. DOI: 10.1103/PhysRevB.74.155108. URL: https://link.aps.org/doi/10.1103/PhysRevB.74.155108.

[135] Matthias Troyer and Uwe-Jens Wiese. “Computational complexity and fundamental limitations to fermionic quantum Monte Carlo simulations”. In: *Physical review letters* 94.17 (2005), p. 170201.

[136] Loig Vaugier, Hong Jiang, and Silke Biermann. “Hubbard U and Hund exchange J in transition metal oxides: Screening versus localization trends from constrained random phase approximation”. In: *Physical Review B* 86.16 (2012), p. 165105.

[137] X. Wang et al. “Epitaxial thin film growth of $Ca2RuO_{4+\delta}$ by pulsed laser deposition”. In: *Applied Physics Letters* 85.25 (2004), pp. 6146–6148. DOI: 10.1063/1.1841451. eprint: https://doi.org/10.1063/1.1841451. URL: https://doi.org/10.1063/1.1841451.

[138] Y. H. Wang et al. “Observation of Floquet-Bloch States on the Surface of a Topological Insulator”. In: *Science* 342.6157 (2013), pp. 453–457. ISSN: 0036-8075. DOI: 10.1126/science.1239834. eprint: https://science.sciencemag.org/content/342/6157/453.full.pdf. URL: https://science.sciencemag.org/content/342/6157/453.

[139] Gregory H. Wannier. “The Structure of Electronic Excitation Levels in Insulating Crystals”. In: *Phys. Rev.* 52 (3 Aug. 1937), pp. 191–197. DOI: 10.1103/PhysRev.52.191. URL: https://link.aps.org/doi/10.1103/PhysRev.52.191.

[140] Hai-Hu Wen and Shiliang Li. “Materials and Novel Superconductivity in Iron Pnictide Superconductors”. In: *Annual Review of Condensed Matter Physics* 2.1 (2011), pp. 121–140. DOI: 10.1146/annurev-conmatphys-062910-140518. eprint: https://doi.org/10.1146/annurev-conmatphys-062910-140518. URL: https://doi.org/10.1146/annurev-conmatphys-062910-140518.

[141] Steffen Wirth and Frank Steglich. “Exploring heavy fermions from macroscopic to microscopic length scales”. In: *Nature Reviews Materials* 1.10 (2016), p. 16051. ISSN: 2058-8437. DOI: 10.1038/natrevmats.2016.51. URL: https://doi.org/10.1038/natrevmats.2016.51.

[142] FC Zhang and TM Rice. “Effective Hamiltonian for the superconducting Cu oxides”. In: *Physical Review B* 37.7 (1988), p. 3759.

[143] Guoren Zhang and Eva Pavarini. “Spin-Orbit and Coulomb Effects in Single-Layered Ruthenates”. In: *physica status solidi (RRL) - Rapid Research Letters* 12.11 (2018), p. 1800211. DOI: 10.1002/pssr.201800211. eprint: https://onlinelibrary.wiley.com/doi/pdf/10.1002/pssr.201800211. URL: https://onlinelibrary.wiley.com/doi/abs/10.1002/pssr.201800211.

List of Figures

1.1 The Hubbard model of a two-dimensional square lattice with first and second nearest neighbors hopping, t and t', and a local Coulomb interaction, U. 9

1.2 A picturial view of the periodic Anderson model (PAM). 11

1.3 Examples of parametrization of the hopping between d-orbitals. The π (σ) bond corresponds to the case where the density distribution lobes point towards (parallel to) each other. 12

1.4 (top-left) The unit cell of a cubic perovskite ABO_3. (top-right) The d orbitals in the basis of tesseral harmonics. (bottom) Energy level splittings of the d-shell due to the experience of an (I) octahedral, O_h, and (II) tetragonal , D_{4h}, crystal-field generated from the surrounding ligands. The far-left case corresponds to a compression of the z-axis while the far-right case corresponds to an elongation of the z-axis. 14

1.5 Energy splittings of the d-shell. **(i)** Splittings based on a cubic crystal-field, which is diagonal in basis of the tesseral harmonics, T_l^m. **(ii)** Splittings generated from the spin-orbit coupling, which is diagonal in the basis of total-angular momentum, $|J;J_z\rangle$. **(iii)** Splittings generated when both cubic crystal-field and spin-orbit coupling operator act on the d-state manifold. Note that no good single particle basis exists [123]. 15

1.6 Examples of Feynman diagrams for the self-energy. **(a)** second-order diagram of the self-energy, **(b)** non-skeleton self-energy diagram, **(c)** Second-order diagram of the self-energy expressed in terms of the interacting (dressed) single-particle propagator. 18

1.7 The DMFT self-consistent scheme. Given the original lattice model we **(I)** fix the particle density – calculating the chemical potential μ – and we obtain the local Green's function of the system. Provided the interacting part of the Hamiltonian, we define and **(II)** solve the AIM. At stage **(III)** we check if the convergence criteria are met and return to stage **(I)** or exit the self-consistent loop, respectively. 21

1.8 A schematic view of the DFT+DMFT self-consistent scheme in its *one-shot* variant. 27

2.1 Example case: the two-dimensional single band Hubbard model described by the dispersion relation $\varepsilon_{\mathbf{k}} = -2t\ (\cos k_x + \cos k_y)$, with $t = 1$ setting the energy units. (upper panel) Bandstructure along the high-symmetry points of the Brillouin-zone. Dashed line corresponds to the assumed chemical potential. (lower left) The Fermi surface of the above model. Full lines correspond to the perfect nesting condition. Dashed lines denote the boundaries of the Brillouin zone. (lower right) The static non-interacting generalized susceptibility as obtained by a direct evaluation of the Lindhard formula. Due to $SU(2)$ symmetry all non-zero elements of the tensor are equal. . . . 36

2.2 Interacting physical susceptibilities obtained with the RPA for the model defined in Fig. 2.1. (left) The static spin-spin response function, $\chi_{ss}(\boldsymbol{q}, 0)$, along the high symmetry points of the Brillouin zone. (right) The static density-density response function, $\chi_{nn}(\boldsymbol{q}, 0)$, along the high symmetry points of the Brillouin zone. 39

2.3 (i) Diagrammatic view of the Bethe-Salpeter equations. (ii) In the case of the single-band Hubbard model and due to $SU(2)$ symmetry only 6 out of 16 equations remain to be solved, while they can be further *diagonalized*. The RPA corresponds to approximating the two-particle vertex Γ with the bare interaction kernel U. 40

2.4 (left) The interacting one-particle Green's function, $G(\tau)$, as obtained by CT-QMC within the DMFT framework for increasing on-site Hubbard interaction strength U. (right) Comparison between ED, CT-QMC and SCA impurity solvers for selected insulating cases on the level of the self-energies. 47

2.5 The two-particle amputated Green's function (left) and the corresponding imaginary part of the self-energy (right) at selected interaction values around the *breakdown* in the last (obtained) iteration. For $U < 2.75$ the self-consistency cycle breaks down and non-causal features in the self-energy appear in the next DMFT iteration. For larger interaction values although the deviations from the numerically exact results are substantial, the DMFT self-consistent cycle can be completed. The abrupt changes between the (non-converging) $U = 2.74$ and (converging) $U = 2.75$ numerically pinpoint the SCA breakdown point. 48

3.1 (left) The unit cell of $LaNiO_2$. (right) The bandstructure along the high-symmetry points of the Brillouin zone. The Fermi energy is adjusted to $E_F = 0\ eV$. 52

3.2 Local spectral functions at nominal filling and for hole and electron doping, aggregated and resolved in terms of the atomic character. 55

3.3 The distribution of the induced charge carriers (holes or electrons) within the nickel, oxygen and lanthanum states. The pie-charts show the relative percentage of the particle distribution within the corresponding states normalized with respect to the overall doping. 56

3.4 Distribution of the charge carriers (holes or electrons) on the Nickel d-orbitals resolved in terms of the corresponding layer. (pie-charts) Concentration of the charge carriers (total sum) with respect to the corresponding layer of the heterostructure. 58

3.5 Layer- and orbital-resolved local spectral functions for the three-holes doping case. 60

3.6 Layer- and orbital-resolved local spectral functions for the two-holes doping case. 61

3.7 Layer- and orbital-resolved local spectral functions for undoped case. 62

3.8 Layer- and orbital-resolved local spectral functions for the two-electron doping case. 63

3.9 Layer- and orbital-resolved local spectral functions for the three-electron doping case. 64

4.1 (left) The conventional unit cell of Ca_2RuO_4. (right) The bandstructure along the high-symmetry points of the Brillouin-zone. The Fermi energy corresponds to $E = 0\ eV$. 67

4.2 Analytically continued self-energies $\Sigma(\omega)$ for all phases. (top) The real-part of the self-energy. (bottom) The imaginary-part of the self-energy. Here we show only the diagonal elements and restrict the visualization on the spin-up block of $\Sigma(\omega)$. 71

4.3 Orbital-resolved local spectral functions $A(\omega)$ (in units of $1/eV$) for all studied structures, as obtained from the analytical continuation of the local Green's function, $G_{\text{loc}}(i\omega_n)$, on the low frequency regime. Here we show only the diagonal elements and restrict the visualization of the spin-up block. 72

4.4 DMFT-calculated intensity map for electrons spectral function $A(\omega, \mathbf{k})$ (in arbitrary units, dark (light) color implies low (high) intensity) as a function of the energy ω (counted from the chemical potential) and momentum $\mathbf{k}$ along the high-symmetry points in the orthorhombic Brillouin zone. From top to bottom: the equilibrium S-phase, the non-equilibrium S^*- and L^*- phases, and the $T = 400\ K$ structure from Ref [38]. The DFT+U mean-field bands are shown in white dashed lines. 74

4.5 The energy level diagram of the lowest lying states in the atomic limit. The color encodes the expectation value of the J^2 operator averaged of the corresponding degenerate states. We refer to the text for further explanations. 79

4.6 The isothermal magnetic response along the z- and x-axis in the atomic limit: (left) spin-orbit coupling, (right) tetragonal crystal-field, and (middle) both spin-orbit coupling and crystal-field operators included. 80

4.7 Comparison of the single-particle spectral functions at fixed inverse temperature $\beta = 20\ eV^{-1}$ for selected values of the on-site Hubbard interaction – (blue) $U = 2.5\ eV$, (orange) $U = 3.5\ eV$ and (green) $U = 6.0\ eV$ – that correspond to different points in the complete phase-diagram. (right) Spectral functions for the m-CF case. (left) Spectral functions for the m-SO case. . 82

4.8 The inverse uniform and static magnetic response corresponding to the $m-SO$ (upper panels) and to the $m-CF$ (lower panels) case, respectively. From left to right we move from the SCM regime into the dMI regime. With black (red) color we plot the exact atomic-limit (RPA) susceptibilities. For the DMFT results we use the same color-encoding as in the case of the local spectral functions. Solid lines correspond to an applied field along the z-axis, while dashed in the x/y-axis. 84

4.9 The inverse uniform and static susceptibilities for the m-CFSO case. From top to bottom (row-wise): the magnetic, orbital, spin and orbital-spin susceptibilities. From left to right (column-wise): strongly correlated metallic, insulating and deep insulating phase. With blue (orange) we depict the data for the z-axis (x/y-axis). Dashed lines are used for the exact atomic-limit values while solid lines correspond to the data on perturbative regime as obtained by RPA. 85

5.1 The single-particle local spectral-functions, as a function of temperature, for all studied models. Row-wise the splitting is adjusted to $\Delta_J = -0.05\ eV$ (upper), $\Delta_J = 0.0\ eV$ (middle) and $\Delta_J = +0.05\ eV$ (lower). 92

5.2 The static magnetic response as a function of temperature, for all studied models. Row-wise the splitting is adjusted to $\Delta_J = -0.05\ eV$ (upper), $\Delta_J = 0.0\ eV$ (middle) and $\Delta_J = +0.05\ eV$ (lower). From left to right the hybridization strength increases as $V = 0.1\ eV$ (left), $V = 0.2\ eV$ (center) and $V = 0.3\ eV$ (right). Red (blue) color encodes a large (small) magnetitude of the measure M_d. 94

5.3 An example case of the magnetic (impurity) response function on the imaginary time axis, at fixed inverse temperature $\beta = 80\ eV^{-1}$ and local splitting $\Delta_J = -0.05\ eV$, and varying hybridization strength V. 95

5.4 The magnetic response in the real frequency domain as a function of temperature, for all studied models. Row-wise the splitting is adjusted to $\Delta_J = -0.05\ eV$ (upper), $\Delta_J = 0.0\ eV$ (middle) and $\Delta_J = +0.05\ eV$ (lower). From left to right the hybridization strength increases as $V = 0.1\ eV$ (left), $V = 0.2\ eV$ (center) and $V = 0.3\ eV$ (right). 97

5.5 The magnetic response in the real time domain as a function of temperature, for all studied models. Row-wise the splitting is adjusted to $\Delta_J = -0.05\ eV$ (upper), $\Delta_J = 0.0\ eV$ (middle) and $\Delta_J = +0.05\ eV$ (lower). From left to right the hybridization strength increases as $V = 0.1\ eV$ (left), $V = 0.2\ eV$ (center) and $V = 0.3\ eV$ (right). 98

List of Tables

4.1 Neutron diffraction structural refinement in the orthorhombic $Pbca$ space group. Ru–O bonds and RuO_6 octahedral parameters at $T = 130\,K$ of the S-phase and S*- and L*-phases at $J = 10\,A\,cm^{-2}$. Θ–O(1) refers to the tilt angle between the basal plane and the ab-plane, Θ–O(2) is the angle between the RuâĂŞ-O(2) bond and the c-axis, and Φ is rotation of the RuO_6 around the c-axis. The Ru–O ratio compares the apical and averaged in-plane Ru-O bond lengths, and is a measure of the tetragonal distortion. Taken from Ref [19]. 68

4.2 Occupation numbers of the t_{2g} orbitals from DMFT calculations. 70

Acknowledgments

Coming to the finish-line, I feel obliged to acknowledge all those people that in one way or other stood by my side, creating the best environment to conduct my research.

First and foremost, I want to thank my supervisor, Dr. Philipp Hansmann, for giving me the opportunity to join his group and being for me a source of endless scientific and psychological support. Our discussions have been intense and inspiring, acting as stimulus for all my project-choices and for the skill set that I developed during this time period. Simply put, I could not ask for anything more. I will always have a debt of gratitude to my office mate, Dr. Xiaodong Cao. Our relationship has always been... explosive and unconditional. And my only hope that I managed to offer as much as support as he offered to me. Many thanks also to my group colleagues, Michael Schmid and Stefan Käser, not only for our scientific collaborations, but also for *forcing* happiness to the toughest periods. I am sure that they will both succeed in their next steps, and they will continue to keep up their smile. Apart from my group, I owe gratitude to Dr. Werner Dobrautz and Dr. Demetrio Vilardi for the fruitful – and endless – scientific (and not only) discussions and for the proof-reading of this dissertation. I am sure that this was just the beginning of a long friendship!

Από καρδιάς ευχαριστίες στην οικογένεια μου και ιδιαίτερα στους γονείς μου, Βασίλη και Μαρία, που ήταν πάντα στο πλευρό μου οποτεδήποτε το χρειάστηκα. Για το τέλος, το πιο μεγάλο ευχαριστώ (τόσο λίγο ακούγεται!) το οφείλω μονάχα σε εσένα Αλεξάνδρα, διότι με κράτησες όρθιο καθ'όλη την προσπάθεια μου και στάθηκες στο πλάι μου στα εύκολα, στα δύσκολα και κυρίως στα άσχημα. Όλη μου η δουλειά είναι αφιερωμένη σε εσένα.